VOLUME 29 JANUARY 1951 NUMBER 1

Canadian Journal of Physics

Editor: G. M. VOLKOFF

NOTE:—This Journal prior to January, 1951, was Section A (Physical Sciences) of the Canadian Journal of Research.

Published by THE NATIONAL RESEARCH COUNCIL
OTTAWA CANADA

CANADIAN JOURNAL OF PHYSICS

This was formerly *Section A, Canadian Journal of Research.* The change to the new name took place January 1, 1951. The CANADIAN JOURNAL OF PHYSICS is published six times annually.

The CANADIAN JOURNAL OF PHYSICS is published by the National Research Council of Canada under the authority of the Chairman of the Committee of the Privy Council on Scientific and Industrial Research. Matters of general policy are the responsibility of a joint Editorial Board consisting of members of the National Research Council of Canada and the Royal Society of Canada.

The National Research Council of Canada publishes also the following Journals: *Canadian Journal of Botany, Canadian Journal of Chemistry, Canadian Journal of Medical Sciences, Canadian Journal of Technology, Canadian Journal of Zoology.*

EDITORIAL BOARD

Representing
NATIONAL RESEARCH COUNCIL

DR. H. P. ARMES (*Chairman*),
Emeritus Dean of Arts and Science,
University of Manitoba,
Winnipeg, Man.

DR. OTTO MAASS,
Macdonald Professor of Physical Chemistry,
McGill University,
Montreal, P.Q.

DR. J. H. L. JOHNSTONE,
Professor of Physics,
Dalhousie University,
Halifax, N.S.

DR. A. BERTRAND,
Professor of Bacteriology,
Faculty of Medicine,
University of Montreal,
Montreal, P.Q.

Representing
ROYAL SOCIETY OF CANADA

DR. G. M. VOLKOFF,
Professor of Physics,
University of British Columbia,
Vancouver, B.C.

DR. J. W. T. SPINKS,
Dean, College of Graduate Studies,
University of Saskatchewan,
Saskatoon, Sask.

Section III

DR. H. S. JACKSON,
Head, Department of Botany,
University of Toronto,
Toronto, Ont.

DR. E. HORNE CRAIGIE,
Department of Zoology,
University of Toronto,
Toronto, Ont.

Section V

Ex officio

DR. LÉO MARION, *Editorial Adviser*,
Division of Chemistry,
National Research Laboratories,
Ottawa.

DR. H. H. SAUNDERSON,
Director, Division of Information Services,
National Research Council,
Ottawa.

Representing
THE CHEMICAL INSTITUTE OF CANADA

DR. H. G. THODE,
Department of Chemistry,
McMaster University,
Hamilton, Ont.

Subscription rate: $2.00 a year. Special rates can be obtained for subscriptions to more than one of the Journals published by the National Research Council. All enquiries concerning subscriptions should be addressed to the CANADIAN JOURNAL OF PHYSICS, National Research Council, Ottawa, Canada.

"Reprinted in entirety by photo-offset from the original issue"

VOLUME 29 1951

Canadian Journal of Physics

NOTE:—This Journal prior to January, 1951, was Section A (Physical Sciences) of the Canadian Journal of Research.

Published by THE NATIONAL RESEARCH COUNCIL
OTTAWA CANADA

Canadian Journal of Physics

Issued by THE NATIONAL RESEARCH COUNCIL OF CANADA

VOL. 29 JANUARY, 1951 NUMBER 1

γ-RAYS PRODUCED BY SLOW NEUTRON CAPTURE IN BERYLLIUM, CARBON, AND NITROGEN[1]

BY B. B. KINSEY, G. A. BARTHOLOMEW, AND W. H. WALKER*

Abstract

The γ-rays produced by slow neutron capture in beryllium, carbon, and nitrogen have been investigated with a pair spectrometer. Only one γ-ray was observed to follow capture in beryllium and in carbon; nine were observed from nitrogen. The neutron binding energies computed from the energies of these radiations are: Be^{10}, 6.797 ± 0.008 Mev.; C^{13}, 4.948 ± 0.008 Mev.; N^{15}, 10.823 ± 0.012 Mev. The nitrogen γ-rays can be fitted into a term scheme containing the previously known excited states of N^{15}, obtained from the study of (d, p) reactions, together with one excited state at 9.16 Mev., hitherto unreported. A comparison of the intensities of the nitrogen and beryllium radiations shows that the radiative capture cross section of nitrogen is at most 160 millibarns.

Introduction

A preliminary report on the γ-rays produced by thermal neutron capture in beryllium, carbon, and nitrogen has appeared elsewhere (15). A more detailed description of these measurements is presented in this paper.

The method of measurement will be fully described in an article to be published shortly. The samples of material to be studied were enclosed in dural containers which were placed in a region of high neutron flux near the reacting vessel in the pile. A bismuth block was placed between the sample and the reactor to prevent radiation from the pile from entering the beam to be studied. Both the dural container and the bismuth block produce unwanted radiations which are superposed on the energy spectrum of the γ-rays produced by the sample. These unwanted radiations were identified by a separate experiment in which an empty container was used.†

In a survey measurement for each sample, the γ-ray spectrum was explored from 3 Mev. to beyond that expected for the binding energy of the product nucleus. This measurement was followed by detailed studies of the coincidence peaks produced by individual radiations. The intensities of the radiations were such that counting times up to one hour were required at each point. The resolution of the spectrometer was chosen to be about 4% for the survey of the γ-rays produced by carbon, and about 2% for all the other measurements.

[1] *Manuscript received August 25, 1950.*
Contribution from the Atomic Energy Project, National Research Council of Canada, Chalk River, Ontario, Canada. Issued as N.R.C. No. 2266.
* *Present address: Department of Chemistry, McMaster University, Hamilton, Ontario.*
† *The spectrum of the empty container (see Fig. 1) is mainly composed of aluminum radiations; two small bumps on either side of the ground state radiation of aluminum are due to copper and manganese. Magnesium does not contribute to the container spectrum in measurable amount.*

Beryllium was irradiated in the form of beryllium oxide. Radiations from oxygen have not been observed, partly because the cross section for capture is very low—about 1.6 millibarns—and because the binding energy of the neutron in O^{17} is low (about 4 Mev.).

Carbon was irradiated in the form of a solid graphite cylinder 4 in. in diameter and 6 in. long. The cylinder was cut from a graphite sample of very high purity. A block of chemically pure lead, 4 in. in diameter and 4 in. long, was placed in the experimental hole between the bismuth plug and the graphite sample in order to absorb the γ-rays produced by neutron capture in the aluminum container enclosing the bismuth plug. An extra lead collimator was placed between the graphite and the spectrometer to ensure that no radiations emitted from the sides of the hole could be seen by the spectrometer. With these precautions aluminum radiations were prevented from entering the spectrometer and ensured that the only radiations below 6 Mev. which might be detected must be due to carbon. Other experiments have shown that lead emits no appreciable amount of radiation below 6.68 Mev. (16).

For the nitrogen experiments samples of beryllium nitride, Be_3N_2, and urea, $CO(NH_2)_2$, were used. Both samples were enclosed in dural containers. The nitrogen radiations are easily recognized from a comparison of the spectra produced by these compounds and by beryllium oxide.

Beryllium

The γ-ray spectrum produced by beryllium oxide in its container and that of the container itself is shown in Fig. 1*, the ordinates of the latter curve being reduced to make the heights of the 7.7 Mev. aluminum peak the same. Within the statistical accuracy the two spectra coincide everywhere except for the broad peak at 4.17 Mev. which appears enhanced in the spectrum of the container, and the peak at 6.79 Mev. and its immediate vicinity. The 4.17 Mev. radiation is due to neutron capture in bismuth and is described elsewhere. (16). This radiation is not appreciably absorbed in the container and is therefore observed in the container spectrum with its full intensity. The transmission of this radiation through beryllium oxide reduces its intensity by about 40%, in rough agreement with the amount expected from calculation.

Fig. 2 shows the results of a more detailed examination of the 6.79 Mev. radiation, the only γ-ray shown in Fig. 1, which can be ascribed to beryllium. The energy of the γ-ray is 6.794 ± 0.008 Mev. When corrected for the recoil of the beryllium nucleus, the transition energy, which is the binding energy of the neutron in Be^{10}, is found to be 6.797 ± 0.008 Mev.

This energy is in good agreement with that calculated from the energy balance of the $Be^9(d, p)Be^{10}$ reaction. For this quantity, Buechner and Strait

* *In all the coincidence spectra shown in this paper, the energy of a γ-ray is given by the abscissa of the linearly extrapolated upper limit of its coincidence peak. The ordinates are not corrected for the variation of the efficiency of the spectrometer with energy.*

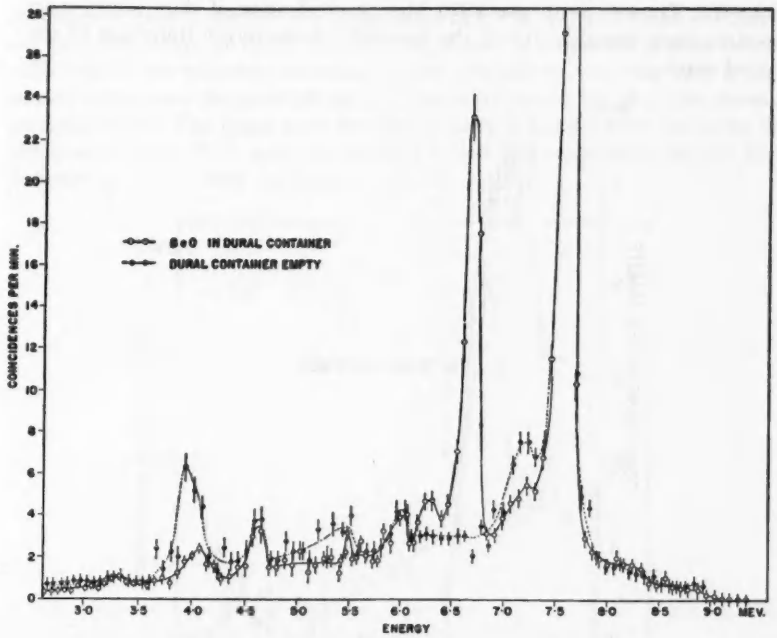

FIG. 1. *Survey spectrum of beryllium capture gamma-radiation.*

(4) have found the value 4.576 ± 0.012 Mev. Using the value of the disintegration energy of the deuteron obtained by Bell and Elliott (1), viz., 2.231 ± 0.007 Mev., and adding the equations:

$$Be^9 + H^2 = Be^{10} + H^1 + 4.576 \pm 0.012 \text{ Mev.}$$
$$H^1 + n = H^2 + 2.231 \pm 0.007 \text{ Mev.}$$

the neutron binding energy is given by:—

$$Be^9 + n = Be^{10} + 6.807 \pm 0.014 \text{ Mev.}$$

Fig. 1 shows little evidence for the existence of any other radiations emitted by beryllium. The small bump on the low energy side of the 6.79 Mev. peak is substantiated by only two points, which are insufficient evidence to prove the existence of a γ-ray. Only one bound excited state is known in Be^{10}. Its energy is 3.375 Mev. (4). A radiative transition from the capturing state to this excited state would have an energy of 3.42 Mev. With a resolution of 2%, the two radiations with energies of 3.375 and 3.42 Mev. would probably appear as a single broad peak in the coincidence spectrum. No such peak was observed (Fig. 1). The ratio of the efficiency for detection by the spectrometer at 3.4 Mev. to that at 6.8 Mev. is 0.07. If it is assumed that the 3.4 Mev. peak would be detectable if its intensity were 0.6 coincidence per minute above the background (or a total of 1.6 coincidences per minute in Fig. 1) then the ratio

of the intensity of the cascaded transitions to the direct transition would be about 0.4. Transitions to the 3.375 Mev. excited state, if they occur, must therefore have less than 0.4 of the intensity of the direct transition to the ground state.

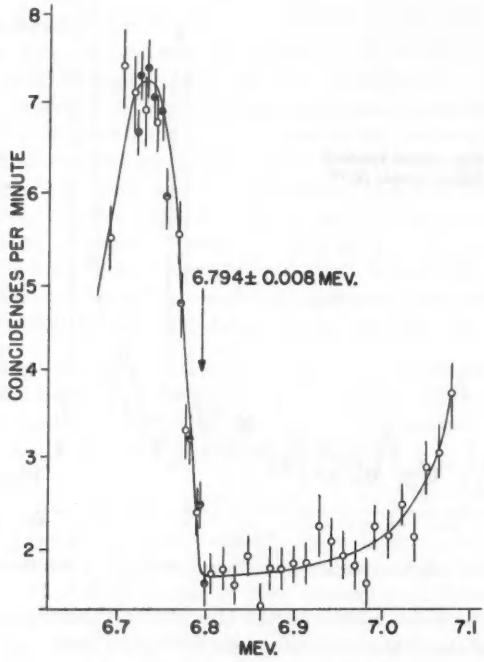

FIG. 2. *Detail of beryllium radiation.*

Carbon

The result of a survey measurement of the γ-rays emitted by carbon between 3 and 5.5 Mev. is shown in Fig. 3. The 4.9 Mev. radiation is emitted in the direct ground state transition in C^{13}. There is some indication of a radiation at 5.3 Mev. It is unlikely that a coincidence peak at this point could be produced by any of the known impurities in the graphite sample used in these experiments. The only impurity with a strong radiation in this region of energy is silicon. However, the amount of this impurity and its cross section are too low to account for the peak observed. No evidence for such a radiation was found in measurements taken with a higher resolution; however, the counting rates observed were so low that a coincidence peak of the height expected was difficult to distinguish against statistical fluctuations.

There is some evidence in Fig. 3 for radiations with energies between 3.4 and 3.7 Mev. These radiations must be due to impurities, for no γ-rays produced

by the excitation of the two low-lying states of C^{13} (5, 17) at 3.1 and 4.0 Mev. can lie in this range. An upper limit may be put on the intensities of these latter radiations if the minimum detectable peak coincidence counting rate is assumed to be twice the probable error of the ordinates of Fig. 3 at the corresponding energy. The upper limit for the intensity of the 3.1 Mev. radiation is found to be about 75%, and that of the 4.0 Mev. radiation about 30% of the intensity of the 4.9 Mev. radiation.

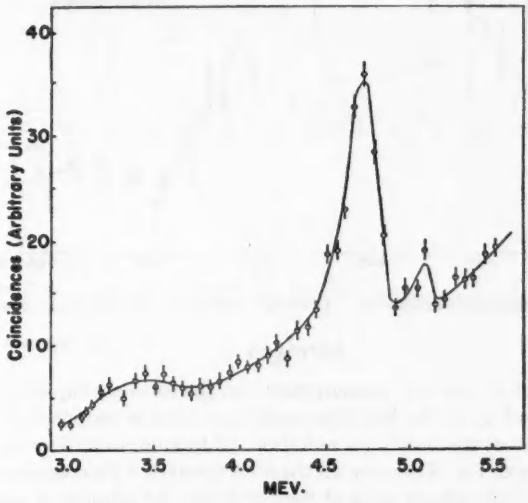

FIG. 3. *Survey spectrum of carbon capture gamma-radiation.*

Fig. 4 shows the result of a detailed examination of the 4.9 Mev. radiation. The energy of this γ-ray is 4.947 ± 0.008 Mev. Correcting for the recoil of the carbon nucleus the corresponding transition energy is 4.948 ± 0.008 Mev. and this must be the binding energy of a neutron to C^{13}. Another value for this energy may be obtained by the addition of the following equations:

$$C^{12} + H^2 = N^{13} + n - 0.281 \pm 0.003 \text{ Mev. (2).}$$
$$N^{13} = C^{13} + 2m_0c^2 + 1.202 \pm 0.005 \text{ Mev. (14, 20).}$$
$$n + H^1 = H^2 + 2.231 \pm 0.007 \text{ Mev. (1).}$$
$$n - H^1 = 0.782 \pm 0.002 \text{ Mev. (19).}$$

The result is:

$$C^{12} + n = C^{13} + 4.954 \pm 0.010 \text{ Mev.}$$

Alternatively, the energy balance, Q, in the C^{12} (d, p) C^{13} reaction is 2.729 ± 0.009 Mev. (5). From this result and the binding energy of the deuteron we find:

$$C^{12} + n = C^{13} + 4.960 \pm 0.012 \text{ Mev.}$$

All three values are in good agreement.

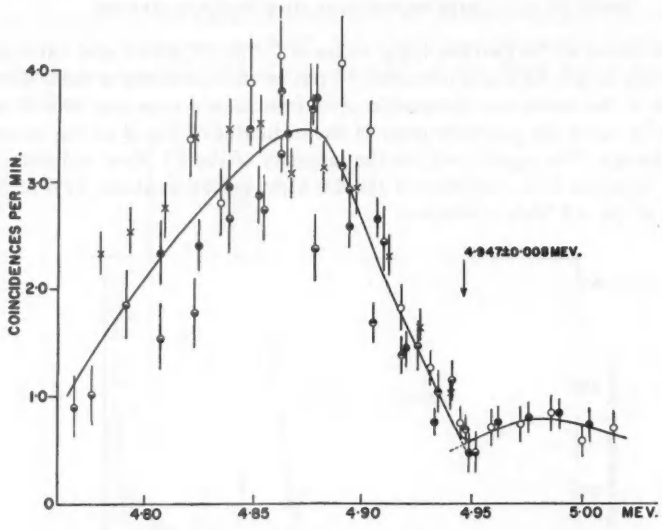

FIG. 4. *Detail of carbon radiation. The results of different experiments are indicated.*

Nitrogen

The results of the survey measurements on the nitrogen capture radiations are contained in Fig. 5. The beryllium oxide spectrum is included in this figure for identification of the beryllium radiation. Aluminum radiation is present in all three spectra of Fig. 5 because all three compounds were contained in dural containers. The coincidence rates of the beryllium and aluminum peaks in the beryllium oxide spectrum are higher than those of the other two spectra because a thicker radiator was used. The difference between the peak counting rates of the nitrogen γ-rays in the urea and beryllium nitride spectra can be accounted for quantitatively in terms of the difference in the nitrogen content of these materials. The nine radiations, lettered A to I in Fig. 5 are assigned to nitrogen.

Figs. 6 to 10 show the results of more detailed studies of the nitrogen radiations obtained with beryllium nitride. Table I contains a summary of the energies of these radiations and the relative intensities after correction of the peak coincidence counting rates for the energy sensitivity of the spectrometer.* The detail of the lower energy radiations is shown in Fig. 6. The peak at 4.70 Mev. is due to the aluminum of the container. The feeble peak at I, however, is certainly due to nitrogen; its intensity relative to the 4.70 Mev. peak has been carefully measured both for urea and for beryllium nitride, the ratio of the two intensities being in the ratio of the numbers of nitrogen atoms con-

* *The relative intensities given in Table I are slightly different from those previously reported (15), minor corrections to the efficiency calculations having been made since.*

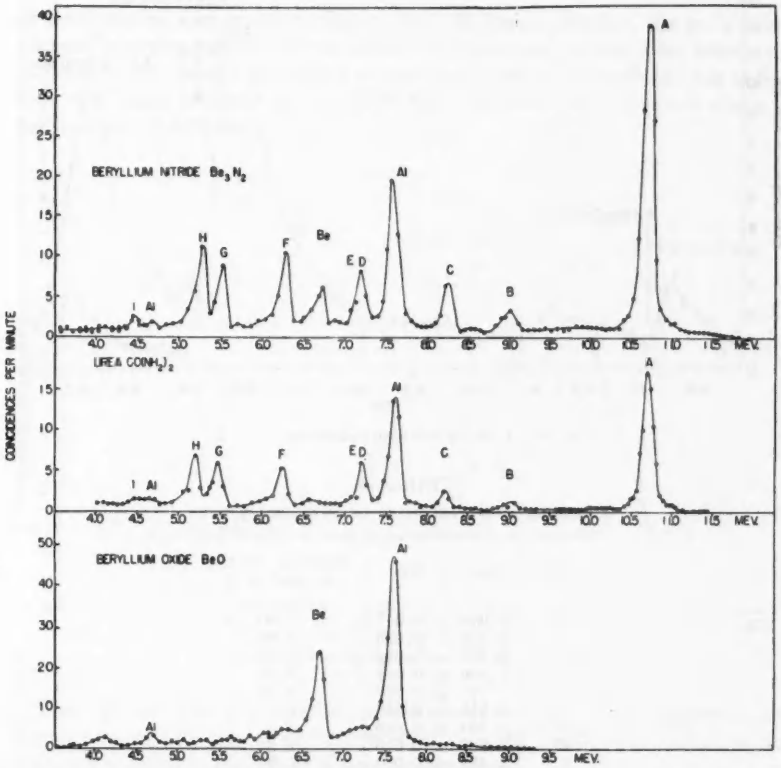

FIG. 5. *Survey spectrum of nitrogen capture gamma-radiation. The nitrogen radiations may be recognized by comparing the three spectra.*

tained by the two samples. The 4.95 Mev. γ-ray due to capture by C^{12} has been identified in a detailed study using urea; the coincidence counting rate was very low and only just enough to be distinguished above the statistical error of the measurements. The height of the peak was roughly equal to that calculated from the preceding carbon measurements. Fig. 6 shows some evidence for radiation at 5.11 Mev. on the tail of the peak H. A similar bump was observed on the tail of this peak in a detailed experiment using urea. In addition some indications have been found for radiations with energies of 5.66 and 6.88 Mev.

The γ-ray F appears to be single and is shown in Fig. 7. The 7 Mev. radiations are shown in detail in Fig. 8; there is good evidence here for two radiations at 7.16 and 7.36 Mev. Since the neutron binding energy in N^{15} is given by the energy of the γ-ray A, viz. 10.82 Mev., the radiation at 7.36 Mev. might be expected to be in cascade with a radiation having an energy of 3.46 Mev.

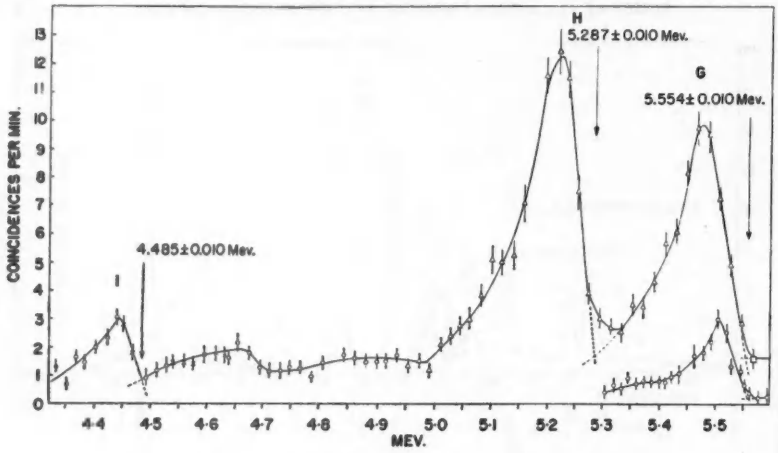

FIG. 6. *Detail of nitrogen radiations, G, H, I.*

TABLE I

ENERGIES AND INTENSITIES OF NITROGEN γ-RAYS

γ-ray	Energy, Mev.	Intensity relative to that of A
A	10.816 ± 0.015	1.00
B	9.156 ± 0.030	0.09
C	8.278 ± 0.016	0.19
D	7.356 ± 0.012	0.56
E	7.164 ± 0.010	0.19
F	6.318 ± 0.010	0.9
G	5.554 ± 0.010	1.5
H	5.287 ± 0.010	2.3
I	4.485 ± 0.010	0.8

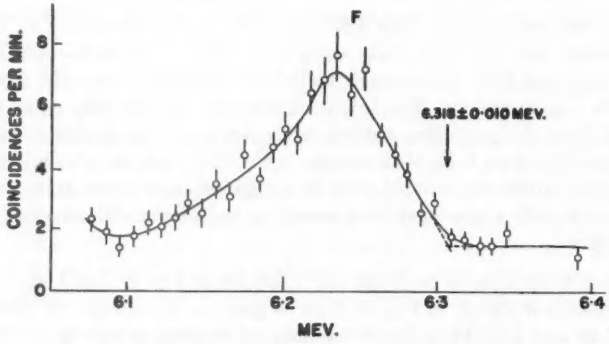

FIG. 7. *Detail of nitrogen radiation F.*

If its intensity were equal to that of the 7.36 Mev. radiation, the peak coincidence counting rate should be 0.03 coincidence per minute after allowance is made for the energy sensitivity of the spectrometer. A search for this radiation was made between 3.0 and 3.75 Mev. but none was detected above a background of 0.05 coincidence per minute.

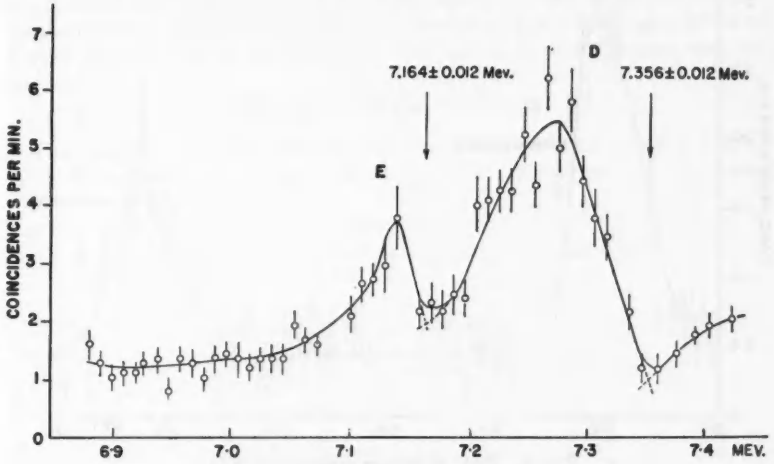

FIG. 8. *Detail of nitrogen radiations D and E.*

The 8.28 and 9.16 Mev. radiations are shown in Fig. 9. Both appear to be homogeneous. The ground state transition, i.e., the 10.82 Mev. radiation A, is shown in detail in Fig. 10. It is also homogeneous.

The energies of the γ-rays H and G, and those of I and F, add up to give the energy of the γ-ray A, and therefore are in cascade. The binding energy of a neutron in N^{15} may be obtained from the energies of the direct radiation A and the sum of the energies of these cascading radiations. Correcting for nuclear recoil and adding, these energies are

From A	10.820 ± 0.015 Mev.
From H + G	10.843 ± 0.014 Mev.
From F + I	10.805 ± 0.014 Mev.

The average of these determinations is:

$$N^{14} + n = N^{15} + 10.823 \pm 0.012 \text{ Mev.}$$

The Q of the N^{14} (d, p) N^{15} reaction reported by Lauritsen (17) is 8.57 Mev. A more recent and probably more accurate determination is 8.61 ± 0.02 Mev. (18). The latter leads to a neutron binding energy in N^{15} of 10.84 ± 0.02 Mev., which is in good agreement with the above value.

The neutron binding energies of C^{13} and N^{15} may be used to calculate the values of certain mass differences which may be compared with mass spectrographic measurements. Taking into account the probable errors of the three

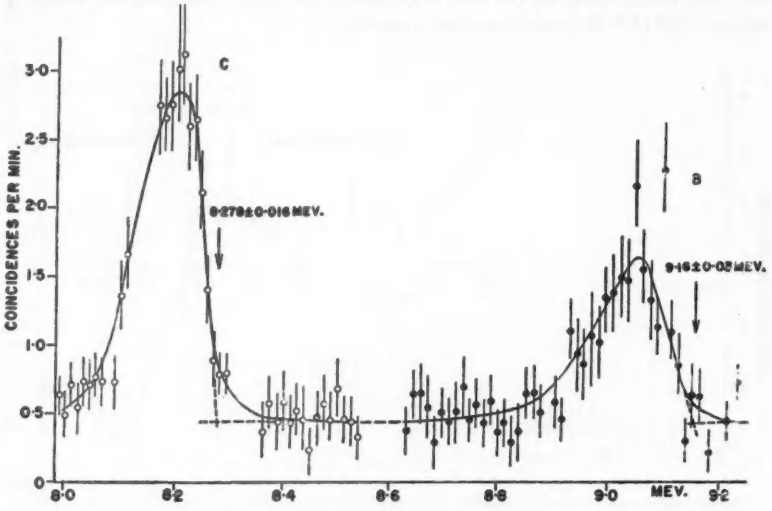

FIG. 9. *Detail of nitrogen radiations B and C.*

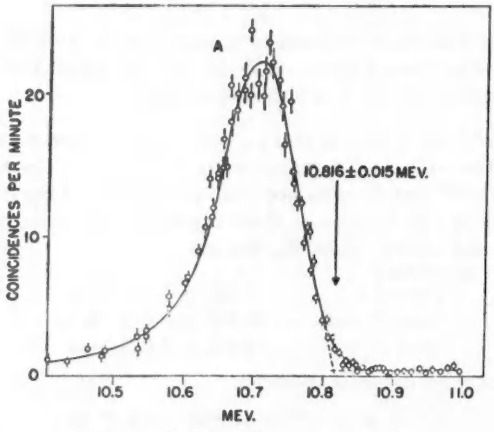

FIG. 10. *Detail of nitrogen radiation A.*

results for the binding energy of C^{13}, the mean binding energy is 4.953 ± 0.006 Mev. From this we obtain:

$$C^{12}H^{1} - C^{13} = 44.80 \pm 0.06 \times 10^{-4} \text{ mu.}$$

Using our value for the binding energy of N^{15} we obtain:

$$N^{14}H^{1} - N^{15} = 107.85 \pm 0.11 \times 10^{-4} \text{ mu.}$$

The first of these two results is significantly higher than that obtained directly by Ewald, (10) viz., $44.10 \pm 0.08 \times 10^{-4}$ mu. Our measurement of the binding energy of a neutron in C^{13} therefore confirms a discrepancy between the transmutation and mass spectrographic data indicated by the results of the measurement of the Q of the C^{12} (d, p) C^{13} reaction. For the nitrogen difference Ewald obtained $107.76 \pm 0.20 \times 10^{-4}$ mu, which is in agreement with our results.

Discussion of the N^{15} Levels

The nitrogen radiations may be fitted to the level scheme shown in Fig. 11. With the exception of the new level at 9.16 Mev., this scheme is in agreement

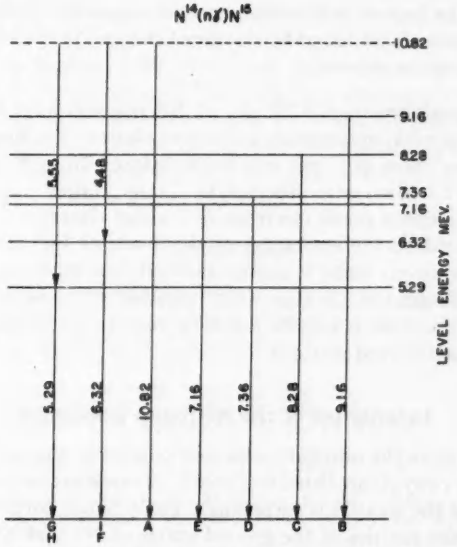

FIG. 11. *Energy level diagram and capture gamma-ray decay scheme of* N^{15}.

with the results of other authors. The 5.3 Mev. level was first observed by Cockcroft and Lewis (6) using the N^{14} (d, p) N^{15} reaction. Lauritsen (17) shows four levels below the binding energy of the neutron in N^{15}; their energies are 5.29, 6.0, 7.2, and 8.2 Mev. The 9 Mev. level seems to have been observed as a proton group in the (d, p) reaction by Guggenheimer, Heitler, and Powell (12) with 6 Mev. deuterons. Most other observers, with deuterons of 1 Mev. or less, as might be expected, have not observed a proton group corresponding to this excitation. It is possible that the 9.16 Mev. γ-ray does not arise from a transition to the ground state from a level with this excitation energy; it can result

from a transition from the capturing state to a level at 1.66 Mev. A proton group corresponding to a level at 1.53 Mev. excitation has been observed by Holloway and Moore (13) using 1.07 Mev. deuterons. This group, however, has not been detected by other observers.

Some of the nitrogen levels seem to possess a fine structure. Malm and Buechner (18) report the presence of two proton groups from the (d, p) reaction corresponding to excitations at 5.29 and 5.32 Mev. The resolving power of the present experiments has not been sufficient to separate such a close doublet. Wyly (21) has shown that both the 6.4 and the 7.3 Mev. levels are double. The energy of the deuterons in his experiments was insufficient to produce in its entirety the proton peak corresponding to the 8.2 Mev. level, but the work of Guggenheimer *et al.* shows that this level is probably double also. The present experiments, however, demonstrate the doublet character of the 7.3 Mev. level but give no evidence for doublet structure in the 6.4 and 8.2 Mev. γ-rays. The lack of such evidence is not surprising; one cannot be sure that a multiplet structure found by the use of charged particle reactions should appear in the γ-ray spectrum.

The γ-rays produced by the N^{14} (d, p) N^{15} reaction have been studied by several observers with, unfortunately, little resolution. The first measurements to be made were those of Crane and his associates (8). γ-Rays with energies of 8.2, 6.6, and 5.1 Mev. were observed by Crane, Halpern, and Oleson (9) by the study of Compton recoil electrons in a cloud chamber. These radiations clearly correspond to the excitation of the levels of Fig. 10. Gaerttner and Pardue (11), however, using a similar method, but studying the energies of electron pairs, found the 5.3 Mev. γ-ray together with one at 7.2 Mev. Their results did not show the 6.6 or the 8.2 Mev. radiations mentioned above. This discrepancy has not been clarified.

Intensities of the Nitrogen Radiations

The intensities of the nitrogen radiations relative to that of the ground state transition, the γ-ray A, are listed in Table I. In consideration of its high energy, the intensity of the γ-ray A is surprisingly weak. Single particle nuclear models indicate that the parities of the ground states of N^{14} and N^{15} should be even and odd respectively. Since the spins of N^{14} and N^{15} are 1 and 1/2 respectively, the ground state transition must be electric dipole. However, A is no more intense than radiations G or I which have only about one half of its energy. It is worth noting that the intensity of the cascading radiations G and H are not equal. The γ-ray H being more intense than G, it is clear that the 5.29 Mev. state is excited, in part, by transitions from higher levels; the radiations, corresponding to these transitions, however, are separately too weak, or possess energies too low to be observed. On the other hand, the γ-rays F and I, which are also in cascade, are of nearly equal intensity.

Radiative Capture Cross Section for Nitrogen

The total number of captures in nitrogen will be roughly proportional to the sum of the intensities of the radiations A, B, C, D, E, F, and H. The ratio of the cross sections for thermal neutron capture by nitrogen and by beryllium will be equal to the ratio of the sum of the nitrogen γ-ray intensities (from beryllium nitride) to that of the beryllium γ-ray, multiplied by 3/2, the ratio of the numbers of beryllium to nitrogen atoms in beryllium nitride. The cross section ratio is 18, whence it may be deduced, that if the cross section of beryllium is 9 millibarns, the radiative capture cross section of nitrogen is 160 millibarns. If there is appreciable excitation of the 3.375 Mev. level in Be^{10}, the nitrogen cross section will be lower in proportion. The above value is therefore an upper limit for the cross section.

This estimate of the nitrogen capture cross section leads to a rough value for the proton width of the capturing state. The total absorption cross section of nitrogen is 1.7 barns (7) and the penetrability of the Coulomb barrier for a proton of 600 kev. is about 1/27. If then the radiation width is of the order of a few volts (3), as would seem probable for light elements, the proton width without barrier is greater than this by a factor which is equal to the reciprocal of the penetrability multiplied by the ratio of the total absorption cross section to the radiative capture cross section. The proton width, therefore, is of the order of a kilovolt. This is a very low result.

References

1. Bell, R. E. Private communication. June, 1950.
2. Bonner, T. W., Evans, J. E., and Hill, J. E. Phys. Rev. 75: 1398. 1949.
3. Brostrom, K. J., Huus, T., and Tangen, R. Phys. Rev. 71: 661. 1947.
4. Buechner, W. W. and Strait, E. N. Phys. Rev. 76: 1547. 1949.
5. Buechner, W. W., Strait, E. N., Sperduto, A., and Malm, R. Phys. Rev. 76: 1543. 1949.
6. Cockcroft, J. D. and Lewis, W. B. Proc. Roy. Soc. (London), A, 154: 261. 1936.
7. Coon, J. H. and Nobles, R. A. Phys. Rev. 75: 1358. 1949.
8. Crane, H. R., Delsasso, L. A., Fowler, W. A., and Lauritsen, C. C. Phys. Rev. 48: 100. 1935.
9. Crane, H. R., Halpern, J., and Oleson, N. L. Phys. Rev. 57: 13. 1940.
10. Ewald, H. Z. Naturforsch. 1: 131. 1946.
11. Gaerttner, E. R. and Pardue, L. A. Phys. Rev. 57: 386. 1940.
12. Guggenheimer, K. M., Heitler, H., and Powell, C. F. Proc. Roy. Soc. (London), A, 190: 196. 1947.
13. Holloway, M. G. and Moore, B. L. Phys. Rev. 56: 705. 1939.
14. Hornyak, W. F. and Lauritsen, T. Phys. Rev. 77: 160. 1950.
15. Kinsey, B. B., Bartholomew, G. A., and Walker, W. H. Phys. Rev. 77: 723. 1950.
16. Kinsey, B. B., Bartholomew, G. A., and Walker, W. H. Phys. Rev. 78: 77. 1950.
17. Lauritsen, T. Nuclear Sci. Ser. Preliminary Rept. No. 5. 1948.
18. Malm, R. and Buechner, W. W. Phys. Rev. 78: 337. 1950.
19. Taschek, R. F., Argo, H. V., Hemmendinger, A., and Jarvis, G. A. Phys. Rev. 76: 325. 1949.
20. Tollestrup, A., Fowler, W. A., and Lauritsen, C. C. Phys. Rev. 78: 372. 1950.
21. Wyly, L. D. Phys. Rev. 76: 316. 1949.

THE ANGULAR DISTRIBUTION OF THE RADIATION AT THE INTERFACE OF TWO ADJOINING MEDIA[1]

By S. Chandrasekhar

Abstract

In this paper the results contained in a recent paper by B. Davison entitled "Angular Distribution of Neutrons at the Interface of Two Adjoining Media" are derived by certain elementary methods based on certain simple invariances characterizing the problem.

1. In a recent paper published in this Journal, B. Davison (2) has considered a problem in the theory of radiative transfer which can be formulated as follows:

The half-space ($\tau < 0$) above a semi-infinite plane-parallel isotropically scattering atmosphere with an albedo ϖ_1 for single scattering is filled with an isotropically scattering atmosphere, similarly stratified, and with an albedo ϖ_2 different from ϖ_1. The equations of transfer valid for $0 < \tau < \infty$ and $0 > \tau > -\infty$ are, respectively,

$$\mu \frac{dI(\tau, \mu)}{d\tau} = I(\tau, \mu) - \tfrac{1}{2}\varpi_1 \int_{-1}^{+1} I(\tau, \mu')d\mu' \quad (\tau > 0) \tag{1}$$

and

$$\mu \frac{dI(\tau, \mu)}{d\tau} = I(\tau, \mu) - \tfrac{1}{2}\varpi_2 \int_{-1}^{+1} I(\tau, \mu')d\mu' \quad (\tau < 0), \tag{2}$$

where τ is the optical thickness measured from the interface of the two media inwards and μ is the cosine of the angle to the outward normal.

It is known that Equation (1) admits an integral of the form

$$I(\tau, \mu) = L_0 \frac{e^{k_1\tau}}{1 - k_1\mu}, \tag{3}$$

where L_0 is a constant and k_1 is the positive root less than 1 of the characteristic equation

$$\varpi_1 \log [(1 + k_1)/(1 - k_1)] = 2k_1. \tag{4}$$

Consider the solution of Equations (1) and (2) which has the asymptotic behavior (3) for $\tau \to \infty$ and which vanishes for $\tau \to -\infty$. The problem is: What is the angular distribution of the radiation at the interface, $\tau = 0$, of the two adjoining media? In the paper we have referred to, Davison has solved this problem by making use of the integral equations of the Schwarzschild–Milne type which govern the problem. However, we shall show that all of Davison's results can be obtained by entirely elementary methods by appealing to certain invariances of the problem in the manner developed by the writer in recent

[1] *Manuscript received August 31, 1950.*
Contribution from Yerkes Observatory, Williams Bay, Wisconsin, U.S.A.

years and summarized in his book (1) (hereafter referred to as *Radiative Transfer*).

2. Let the law of diffuse reflection by a semi-infinite plane-parallel atmosphere be expressed in terms of a scattering function S in the usual fashion (*Radiative Transfer*, p. 90). For an isotropically scattering atmosphere with an albedo ϖ the scattering function is given by (*Radiative Transfer*, pp. 97-98)

$$S(\mu, \mu') = \varpi \frac{\mu\mu'}{\mu + \mu'} H(\mu)H(\mu'), \tag{5}$$

where $-\mu'$ refers to the incident direction and μ to the scattered direction and

$$H(\mu) = 1 + \tfrac{1}{2}\int_0^1 S(\mu, \mu') \frac{d\mu'}{\mu'}, \tag{6}$$

satisfies the integral equation

$$H(\mu) = 1 + \tfrac{1}{2}\varpi\mu H(\mu)\int_0^1 \frac{H(\mu')}{\mu + \mu'} d\mu'. \tag{7}$$

An alternative form of Equation (7) which we shall find useful is

$$\frac{1}{H(\mu)} = 1 - \tfrac{1}{2}\varpi\mu\int_0^1 \frac{H(\mu')}{\mu + \mu'} d\mu'. \tag{8}$$

3. Let $I(\tau, +\mu)$ and $I(\tau, -\mu)$ $(0 < \mu \leqslant 1)$ refer to the outward and the inward directed radiations at the level τ. Now the inward directed radiation $I(\tau, -\mu)$ at a level $\tau > 0$ must be reflected by the semi-infinite atmosphere below τ according to the scattering function $S_1(\mu, \mu')$, appropriate for an isotropically scattering atmosphere with an albedo ϖ_1. (We shall use a subscript 1 to all functions referring to an atmosphere with an albedo ϖ_1 and similarly a subscript 2 to all functions referring to an atmosphere with an albedo ϖ_2.) It is evident that this reflection of the radiation $I(\tau, -\mu)$ by the atmosphere below τ must account for the difference between $I(\tau, +\mu)$ and $I(0, +\mu)$. Indeed, a little consideration shows that (cf. *Radiative Transfer*, p. 81, for the analogous formulation in the conservative case)

$$I(\tau, +\mu) = e^{k_1\tau} I(0, +\mu) + \frac{e^{-k_1\tau}}{2\mu}\int_0^1 S_1(\mu, \mu') I(\tau, -\mu')d\mu' \quad (\tau > 0). \tag{9}$$

The reason for the appearance of the factors $e^{k_1\tau}$ and $e^{-k_1\tau}$ in Equation (9) is that we are considering a situation in which the asymptotic behavior at $\tau = \infty$ is

$$I(\tau, \mu) \to L_0 \frac{e^{k_1\tau}}{1 - k_1\mu}. \tag{10}$$

Accordingly, there is an infinite source of radiation at great depths and the transformation $\tau \to \tau + t$, where t is a constant, is equivalent to multiplying all outward intensities by $e^{k_1 t}$ and all the inward intensities by $e^{-k_1 t}$.

Similarly, considering the inward directed radiation $I(\tau, -\mu)$ at a level $\tau < 0$, we must have

$$I(\tau, -\mu) = e^{k_1\tau} I(0, -\mu) + \frac{e^{-k_1\tau}}{2\mu} \int_0^1 S_2(\mu, \mu')\, I(\tau, +\mu') d\mu' \quad (\tau < 0). \tag{11}$$

We can obtain a pair of integral equations connecting $I(0, +\mu)$ and $I(0, -\mu)$ by differentiating Equations (9) and (11) and passing to the limits $\tau = +0$ and $\tau = -0$, respectively. Thus, from Equation (9) we obtain

$$\begin{aligned}\left[\frac{dI(\tau, +\mu)}{d\tau}\right]_{\tau=+0} &= k_1 I(0, +\mu) - \frac{k_1}{2\mu}\int_0^1 S_1(\mu, \mu') I(0, -\mu')\, d\mu' \\ &\quad + \frac{1}{2\mu}\int_0^1 S_1(\mu, \mu')\left[\frac{dI(\tau, -\mu')}{d\tau}\right]_{\tau=+0} d\mu'.\end{aligned} \tag{12}$$

On the other hand from the equation of transfer (1) (which is appropriate for $\tau > 0$) we conclude that

$$\begin{aligned}\left[\frac{dI(\tau, +\mu)}{d\tau}\right]_{\tau=+0} &= \frac{1}{\mu}[I(0, +\mu) - \varpi_1 J(0)] \\ \text{and} \qquad \left[\frac{dI(\tau, -\mu)}{d\tau}\right]_{\tau=+0} &= \frac{1}{\mu}[\varpi_1 J(0) - I(0, -\mu)],\end{aligned} \tag{13}$$

where we have written

$$J(0) = \tfrac{1}{2}\int_{-1}^{+1} I(0, \mu)\, d\mu. \tag{14}$$

Substituting from Equations (13) in Equation (11) we obtain after some minor rearranging of the terms:

$$\begin{aligned}(1 - k_1\mu)\, I(0, +\mu) &= \varpi_1 J(0)\left[1 + \tfrac{1}{2}\int_0^1 S_1(\mu, \mu')\frac{d\mu'}{\mu'}\right] \\ &\quad - \tfrac{1}{2}\int_0^1 S_1(\mu, \mu')\,(1 + k_1\mu') I(0, -\mu')\frac{d\mu'}{\mu'}.\end{aligned} \tag{15}$$

Similarly, from Equation (11) we obtain

$$\begin{aligned}(1 + k_1\mu)\, I(0, -\mu) &= \varpi_2 J(0)\left[1 + \tfrac{1}{2}\int_0^1 S_2(\mu, \mu')\frac{d\mu'}{\mu'}\right] \\ &\quad - \tfrac{1}{2}\int_0^1 S_2(\mu, \mu')\,(1 - k_1\mu')\, I(0, +\mu')\frac{d\mu'}{\mu'}.\end{aligned} \tag{16}$$

Equations (15) *and* (16) *are the mathematical expressions of the invariance of the angular distribution of the radiation at the interface adjoining the two media for arbitrary normal displacements of the interface.*

Now substituting for S_1 and S_2 according to Equations (5) and (6), we obtain

$$(1 - k_1\mu)\, I(0, +\mu) = \varpi_1 J(0) H_1(\mu) - \tfrac{1}{2}\varpi_1 \mu H_1(\mu) \int_0^1 \frac{H_1(\mu')}{\mu + \mu'} (1 + k_1\mu') I(0, -\mu') d\mu' \tag{17}$$

and

$$(1 + k_1\mu) I(0, -\mu) = \varpi_2 J(0) H_2(\mu) - \tfrac{1}{2}\varpi_2 \mu H_2(\mu) \int_0^1 \frac{H_2(\mu')}{\mu + \mu'} (1 - k_1\mu')\, I(0, +\mu') d\mu'. \tag{18}$$

Equations (17) and (18) represent a pair of integral equations governing $I(0, +\mu)$ and $I(0, -\mu)$.

Writing

$$(1 - k_1\mu) I(0, +\mu) = \varpi_1 J(0) F_1(\mu) \tag{19}$$

and

$$(1 + k_1\mu) I(0, -\mu) = \varpi_2 J(0) F_2(\mu),$$

we observe that Equations (17) and (18) become

$$F_1(\mu) = H_1(\mu) \left[1 - \tfrac{1}{2}\varpi_2 \mu \int_0^1 \frac{H_1(\mu')}{\mu + \mu'} F_2(\mu') d\mu' \right] \tag{20}$$

and

$$F_2(\mu) = H_2(\mu) \left[1 - \tfrac{1}{2}\varpi_1 \mu \int_0^1 \frac{H_2(\mu')}{\mu + \mu'} F_1(\mu') d\mu' \right].$$

From these equations it is at once evident that

$$F_1(\mu) = \frac{H_1(\mu)}{H_2(\mu)} \text{ and } F_2(\mu) = \frac{H_2(\mu)}{H_1(\mu)}. \tag{21}$$

The angular distribution of the radiation at $\tau = 0$ is, therefore, given by

$$I(0, +\mu) = \varpi_1 J(0) \frac{H_1(\mu)}{H_2(\mu)(1 - k_1\mu)} \tag{22}$$

and

$$I(0, -\mu) = \varpi_2 J(0) \frac{H_2(\mu)}{H_1(\mu)(1 + k_1\mu)}.$$

It can be verified that the foregoing solution is equivalent to that given by Davison (*loc. cit.* Equations [21] and [30]).

4. For the solution (22) to be self-consistent it is necessary that

$$J(0) = \tfrac{1}{2} \int_0^1 [I(0, +\mu) + I(0, -\mu)]\, d\mu = J(0) \left\{ \tfrac{1}{2}\varpi_1 \int_0^1 \frac{H_1(\mu)}{H_2(\mu)(1 - k_1\mu)} d\mu + \tfrac{1}{2}\varpi_2 \int_0^1 \frac{H_2(\mu)}{H_1(\mu)(1 + k_1\mu)} d\mu \right\}. \tag{23}$$

In other words, we must have

$$\tfrac{1}{2}\varpi_1 \int_0^1 \frac{H_1(\mu)}{H_2(\mu)(1 - k_1\mu)} d\mu + \tfrac{1}{2}\varpi_2 \int_0^1 \frac{H_2(\mu)}{H_1(\mu)(1 + k_1\mu)} d\mu = 1. \tag{24}$$

The truth of this identity can be verified as follows:

Substituting for $1/H_2(\mu)$ according to Equation (8) in the first integral in Equation (24), we have

$$\begin{aligned}&\tfrac{1}{2}\varpi_1\int_0^1\frac{H_1(\mu)}{H_2(\mu)(1-k_1\mu)}\,d\mu\\&\quad=\tfrac{1}{2}\varpi_1\int_0^1 d\mu\,\frac{H_1(\mu)}{1-k_1\mu}\left\{1-\tfrac{1}{2}\varpi_2\,\mu\int_0^1\frac{H_2(\mu')}{\mu+\mu'}\,d\mu'\right\}.\end{aligned}\tag{25}$$

On the other hand, since $-1/k_1$ is a pole of $H_1(\mu)$ (*Radiative Transfer*, pp. 123 and 350),

$$\tfrac{1}{2}\varpi_1\int_0^1\frac{H_1(\mu)}{1-k_1\mu}\,d\mu=1.\tag{26}$$

The right-hand side of Equation (25) therefore becomes

$$1-\tfrac{1}{4}\varpi_1\varpi_2\int_0^1\int_0^1\frac{\mu H_1(\mu)H_2(\mu')}{(1-k_1\mu)\,(\mu+\mu')}\,d\mu\,d\mu'.\tag{27}$$

Now it can be readily verified* that

$$\tfrac{1}{2}\varpi_1\int_0^1\frac{\mu H_1(\mu)}{(1+b\mu)(\mu+\mu')}\,d\mu=\frac{1}{1-b\mu'}\left[\frac{1}{H_1(\mu')}-\frac{1}{H_1(1/b)}\right],\tag{28}$$

where b is a constant. For $b=-1/k_1$, this relation reduces to (cf. the remarks preceding Equation 26)

$$\tfrac{1}{2}\varpi_1\int_0^1\frac{\mu H_1(\mu)}{(1-k_1\mu)(\mu+\mu')}\,d\mu=\frac{1}{(1+k_1\mu')\,H_1(\mu')}.\tag{29}$$

Accordingly the integration over μ in (27) can be performed and we are left with

$$\tfrac{1}{2}\varpi_1\int_0^1\frac{H_1(\mu)}{H_2(\mu)(1-k_1\mu)}\,d\mu=1-\tfrac{1}{2}\varpi_2\int_0^1\frac{H_2(\mu')}{(1+k_1\mu')H_1(\mu')}\,d\mu'.\tag{30}$$

This completes the verification of the identity (24).

5. The net flux $\pi F(0)$ of the radiation at $\tau=0$ can also be directly evaluated. Thus

$$\begin{aligned}2\int_0^1 I(0,+\mu)\,\mu d\mu&=2\varpi_1 J(0)\int_0^1\frac{H_1(\mu)\mu}{H_2(\mu)(1-k_1\mu)}\,d\mu\\&=\frac{2\varpi_1}{k_1}J(0)\left[\int_0^1 d\mu H_1(\mu)\left\{\frac{1}{1-k_1\mu}-1\right\}\left\{1-\tfrac{1}{2}\varpi_2\mu\int_0^1 d\mu'\frac{H_2(\mu')}{\mu+\mu'}\right\}\right]\\&=\frac{4}{k_1}J(0)\left[1-\{1-(1-\varpi_1)^{1/2}\}-\tfrac{1}{4}\varpi_1\varpi_2\int_0^1 d\mu' H_2(\mu')\right.\end{aligned}$$

* *By expressing* $\mu/[(1+b\mu)(\mu+\mu')]$ *in partial fractions and using the equation satisfied by* $H_1(\mu)$.

$$\times\left\{\int_0^1 d\mu\,\frac{H_1(\mu)\mu}{(\mu+\mu')(1-k_1\mu)}-\int_0^1 d\mu\,\frac{H_1(\mu)\mu}{\mu+\mu'}\right\}\Bigg]$$

$$=\frac{4}{k_1}J(0)\Bigg[(1-\varpi_1)^{1/2}-\tfrac{1}{2}\varpi_2\int_0^1 d\mu' H_2(\mu')\left\{\frac{1}{(1+k_1\mu')H_1(\mu')}\right. \tag{31}$$

$$\left.-\frac{1}{H_1(\mu')}+(1-\varpi_1)^{1/2}\right\}\Bigg]$$

$$=\frac{4}{k_1}J(0)\Bigg[(1-\varpi_1)^{1/2}-(1-\varpi_1)^{1/2}\left\{1-(1-\varpi_2)^{1/2}\right\}$$

$$+\tfrac{1}{2}\varpi_2 k_1\int_0^1\frac{H_2(\mu')\mu'}{(1+k_1\mu')H_1(\mu')}d\mu'\Bigg]$$

$$=\frac{4}{k_1}(1-\varpi_1)^{1/2}(1-\varpi_2)^{1/2}J(0)+2\int_0^1 I(0,-\mu)\mu d\mu.$$

In the foregoing reductions we have made use of the various integral properties of the H-functions (*Radiative Transfer*, Chap. V.). We have thus proved that

$$\frac{F(0)}{J(0)}=\frac{4}{k_1}(1-\varpi_1)^{1/2}(1-\varpi_2)^{1/2}. \tag{32}$$

6. Finally, we may draw attention to a further invariance characterizing the problem. Considering the radiation at the interface $\tau=0$, we observe that the inward directed radiation $I(0,-\mu)$ at $\tau=0$ can be regarded as resulting from the reflection of the outward directed radiation $I(0,+\mu)$ by the semi-infinite atmosphere overlying $\tau=0$. Thus:

$$I(0,-\mu)=\frac{1}{2\mu}\int_0^1 S_2(\mu,\mu')I(0,+\mu')d\mu',$$

$$\text{or}\qquad I(0,-\mu)=\tfrac{1}{2}\varpi_2 H_2(\mu)\int_0^1\frac{\mu' H_2(\mu')}{\mu+\mu'}I(0,+\mu')\,d\mu'. \tag{33}$$

On the other hand the reflection of $I(0,-\mu)$ by the atmosphere below $\tau=0$ cannot account for all of $I(0,+\mu)$; it can account for only that part of the outward directed direction at $\tau=0$ which is in *excess* of what will be present in the absence of an atmosphere above $\tau=0$. Now we know that when there is no atmosphere above $\tau=0$ the angular distribution of the emergent radiation is given by (*Radiative Transfer*, p. 346)

$$I(0,+\mu)=\frac{L_0}{H_1(1/k_1)}\frac{H_1(\mu)}{1-k_1\mu}. \tag{34}$$

Accordingly

$$I(0,+\mu)-\frac{L_0}{H_1(1/k_1)}\frac{H_1(\mu)}{1-k_1\mu}=\frac{1}{2\mu}\int_0^1 S_1(\mu,\mu')I(0,-\mu')\,d\mu'$$

$$=\tfrac{1}{2}\varpi_1 H_1(\mu)\int_0^1\frac{H_1(\mu')\mu'}{\mu+\mu'}I(0,-\mu')\,d\mu'. \tag{35}$$

It can be directly verified that with $I(0, +\mu)$ and $I(0, -\mu)$ given by Equations (22) the invariance (33) is identically satisfied. Moreover, the evaluation of the right-hand side of Equation (35) for $I(0, -\mu)$ given by (22) leads to a determination of the constant L_0 in the asymptotic behavior of the solution at $\tau = \infty$. We find

$$L_0 = \varpi_1 J(0) \frac{H_1(1/k_1)}{H_2(1/k_1)}. \tag{36}$$

7. In conclusion it may be stated that there is no difficulty in extending the methods of this paper to more general laws of scattering (cf. *Radiative Transfer*, Chaps. VI, IX, X, and Appendix III).

References

1. CHANDRASEKHAR, S. Radiative transfer. Oxford University Press. 1950.
2. DAVISON, B. Can. J. Research, A, 28: 303. 1950.

THE EFFECTS OF PLASTIC DEFORMATION ON MAGNETIC PROPERTIES OF POLYCRYSTALLINE METALS[1]

By Ursula M. Martius

Abstract

Most of the laws of the ferromagnetic behavior of metals and alloys were derived from studies of single crystals. In order to apply these laws to polycrystalline metals the effect of the crystallographic composition of the polycrystalline body has to be taken into account. For this purpose the concept of a "closed flux shell" as a fundamental quality of polycrystalline metal is put forward on the basis of the following trend of thought:

One of the most important factors determining the size and arrangement of ferromagnetic domains in a single crystal is the tendency to close the magnetic flux throughout the specimen by a suitable arrangement of these domains. The size of the crystal defines the limits within which the flux can be closed. In a polycrystalline metal, a "crystal" is defined as a region of one crystallographic orientation separated by crystal boundaries from neighboring regions of different orientation. The corresponding unit, as far as ferromagnetic properties are concerned, will be a closed flux shell which may contain many domains but is always a region of closed magnetic flux. Neighboring regions, having different crystallographic orientation, will each also consist of a closed magnetic flux shell. Crystal boundaries are regarded as lattice discontinuities which separate regions of different orientation and at the same time separate different closed flux shells.

The consequences of this model and experimental evidence supporting it are discussed. An explanation of the effect of plastic deformation on magnetic properties is suggested by considering the changes in the size of the closed flux shell which will occur during plastic deformation.

Recently, both the theory of mechanical behavior and the theory of ferromagnetic properties of metals have been advanced considerably. At present it seems worth while to investigate the effect of mechanical changes in metals on their magnetic properties with the object of using the observed changes in magnetic properties to obtain a more thorough understanding of the mechanism of deformation and failure of metals.

The Ontario Research Foundation has been engaged for some time in such an investigation. In utilizing present ferromagnetic theory to explain the observed behavior of magnetic materials during deformation, it became quite apparent that the magnetic properties were not changing in our polycrystalline samples in any way that could be explained fully by the domain theory as we know it. This theory has been derived mainly from the study of single crystals. It became evident that the introduction of a new unit of magnetic structure was necessary in our consideration of the behavior of polycrystalline metals.

The conception of a "*closed flux shell*" as the unit of magnetic structure in a polycrystalline metal is put forward in this paper. This conception has

[1] *Manuscript received July 11, 1950.*
Contribution from the Department of Engineering and Metallurgy, Ontario Research Foundation, Toronto, Ont. Presented at the fifth Annual Congress of the Canadian Association of Physicists, McMaster University, Hamilton, Ont., May, 1950.

proved useful in visualizing and predicting the magnetic behavior of polycrystalline metals under the influence of external stress, particularly in the range where plastic deformation of the metal occurs. In order to discuss the consequences of this conception, it will be necessary to give a brief account of the present status of the dislocation theory of plastic deformation and of the domain theory of ferromagnetism.

The Dislocation Theory and Plastic Deformation

The current ideas on the strength of solids are based mainly on the dislocation theory (5).

According to this theory, every real crystal contains a certain number of dislocations. A dislocation is a linear lattice defect which exists in a crystal when two atomic planes are displaced in respect to each other over part of their surface. There are two main types of dislocations, namely "edge" and "screw" dislocations, the difference depending on the direction of displacement.

The dislocation is characterized by its mobility along the glide plane and the fact that such movement causes the one half-crystal on either side of the glide plane to be displaced in the slip direction. Edge and screw dislocations differ only in the direction of the dislocation axis relative to the slip direction. These specific properties distinguish dislocations sharply from other types of lattice defects. A dislocation as a lattice discontinuity cannot end within the crystal but continues on to the crystal boundaries or else forms a closed loop. It is possible to treat grain boundaries as arrays of dislocations, as Shockley and Read have done recently (10).

Because of the atomic displacements, which define them, dislocations are centers of internal stress. The stress falls off inversely with the distance from the center of the dislocation. Through this stress field a dislocation can interact with other dislocations, with crystal boundaries, foreign atoms and irregularities of the lattice. In many cases the mechanism of interaction can be predicted. If, for instance, an atom in an interstitial position causes a local lattice expansion, it will migrate under the action of the stress field of a dislocation to the locally expanded region at the crystal around the dislocation. Atoms causing compression will consequently concentrate in the compression zone.

It is the basic conception of the theory that plastic deformation in crystalline solids takes place through the motion of dislocations. This idea has proved extremely successful because, in connection with the established properties of dislocations, it affords an explanation of creep and slip, of the existence of an elastic limit and its dependence on preworking and other properties of the metal.

If an external force is sufficiently strong, it will cause a dislocation to move. That is equivalent to saying that the forces will cause slipping of one part of a crystal with respect to another. Considering the details of this mechanism,

it is postulated that new dislocations can be created in the same slip plane which then move under the same external forces. This process cannot be extended indefinitely, since resistance to further deformation increases with the amount of plastic deformation a metal has already undergone. This can only mean that it becomes more difficult to produce or move a dislocation. The forces necessary to move a dislocation increase with increasing numbers of dislocations. The stress fields of the dislocations interact and this interaction limits the dislocation density. Eventually the positions of the dislocations with respect to each other will be fixed in some regular pattern. On this basis it is possible to understand why the deformed metal has a higher elastic limit and why the resistance to further deformation increases with the amount of previous deformation. These new conceptions will have considerable bearing on our interpretation of the ferromagnetic properties of metals.

Domain Theory of Ferromagnetism

The main achievement in the recent work on problems of ferromagnetism has been the explanation and prediction of domain structures under given experimental conditions (7).

It has long been realized that a ferromagnetic body is composed of "domains" magnetized to saturation and separated by transition layers called Bloch walls. The domains are so oriented that in the absence of an external field no over-all magnetization occurs. The observed magnetization process can always be explained by changes in domain size and changes in direction of magnetization of a domain with respect to the field.

The thermodynamical reason for the formation of domains is that the free energy of the specimen can thus be reduced considerably. On the basis of the conception of minimum energy it is possible to derive domain structures for a given crystal. These structures have been verified experimentally by Williams and coworkers who also succeeded in showing the change in domain size caused by the action of an external field. These experiments are the most important confirmation of the basic ideas of the domain theory (11, 12).

It is known today that there are two characteristic kinds of domains: interior domains and surface domains. The domains in the interior are fairly large and of simple structure. Their directions of magnetization are antiparallel (9). The surface domains are more complicated and their structure is mainly determined by the surface energy of the specimen. Their arrangement is always such that they close the magnetic flux throughout the specimen in order to avoid "free magnetic charges" on the surface of the sample.

The idea that the tendency to establish a closed flux structure is one of the most important factors determining the domain structure was first put forward by Landau and Lifshitz, then taken up and extended by Néel and others (9).

The actual size and arrangement of the domains depends largely on size, shape, and condition of the sample and the crystallographic properties of the metal.

Ferromagnetic single crystals have strong directional properties. They show certain preferred crystallographic directions along which they can be magnetized with a minimum amount of external energy. Considerable additional energy is required to turn the magnetization from this "easy" direction into a "hard" one. This anisotropy energy relates the ferromagnetic to the crystallographic properties. It is also the root of the phenomenon of "magnetostriction". Positive magnetostriction means that during magnetization the linear dimensions of a crystal increase in the direction of the applied field and that, conversely, under stress the magnetization increases in the direction of the applied tension. By virtue of this fundamental relationship, it is possible to influence the magnetization process by external stresses.

There is, however, also an indirect effect of the stress. Every external stress will cause strains in the lattice and these deviations from perfect regularity will influence the domain behavior. Roughly speaking, the internal strains increase the resistance towards movement of the Bloch walls and cause changes in the anisotropy conditions.

These considerations are valid only for stresses below the elastic limit of the metal.

Magnetic Structure of Polycrystalline Metals

The laws of the behavior of ferromagnetic domains outlined above are derived from investigations of single crystals. For a polycrystalline metal without special texture, the same considerations should be valid. However, quite generally, the properties of a polycrystalline metal are not just the sum of the corresponding properties of all single crystals, suitably averaged. There are essential differences: for instance, the influence of the crystal surfaces and of the presence of the neighboring crystals will enter the picture and these effects will become increasingly prominent with decreasing grain size.

A polycrystalline metal can be described as an assembly of small crystals oriented at random and separated by crystal boundaries. A crystal would then be defined as a region of one crystallographic orientation separated from the neighboring similar regions with different orientation by a crystal boundary. If this polycrystalline metal is ferromagnetic, the size and shape of the crystals will strongly influence the domain structure. As outlined for the case of single crystals, the presence of the crystal surface and the fact of the finite size of the crystal are the reasons for the formation of the surface domains which tend to close the magnetic flux throughout the specimen. Thus, as far as the ferromagnetic properties are concerned we regard a "crystal" as a region which may contain many domains but has a single closed magnetic flux structure.

The neighboring "crystal", again a region of closed magnetic flux in itself, will have a different crystallographic orientation, and the whole polycrystalline metal can be pictured as an arrangement of these closed flux regions.

It is a purpose of this paper to introduce this concept of "closed flux shells" as a fundamental quality of polycrystalline ferromagnetic metals. As long as a region in the polycrystalline metal has the same crystallographic orientation, it will also form *one* closed flux shell. Any lattice discontinuity that acts as a boundary in the crystallographic sense by separating regions of different orientation will also act as a surface in the ferromagnetic picture by giving rise to the formation of surface domains and dividing closed flux regions.

The polycrystalline metal would then be composed of closed flux shells separated by shell surfaces. Each shell would consist of an arrangement of domains. The domains within the shells are separated by Bloch walls.

There is a fundamental difference between Bloch walls and shell surfaces. The Bloch walls are transition layers between regions of different magnetization, that is, different spin orientation (but it is assumed that the angle between neighboring spins is small and that there is no change in lattice parameter). The shell surfaces, on the other hand, separate regions of different crystallographic orientations and, at the same time, regions belonging to different magnetic "circuits". Bloch walls can be displaced by an external magnetic field, whereas the field cannot act on the shell surfaces as such. Its only effect on a surface is an indirect one, caused by the change in the surface conditions through the displacement of the Bloch walls.

The behavior of polycrystalline ferromagnetic metals under external forces will then be the superposition of two factors; (*a*) the action of the external forces on the single closed flux shell (where the laws of the behavior of single crystals are completely applicable), and (*b*) the action of the external forces on the arrangement of the shells.

In the case of an external magnetic field, this may seem trivial. In this case it is always possible to take the action on the arrangement into account by considering the change in the internal demagnetization field, but even here the closed flux shell model points to some further conclusions:

Within a closed flux shell the size and the distribution of the domains depends on the shape and size of the shell and on the conditions of the shell surface for any given metal. With decreasing shell size, which corresponds to decreasing grain size, the surface domains will become more and more predominant. They are separated by 90° walls so that with decreasing shell size the influence of the 90° walls will increase. This should affect the values of the coercive force and the hysteresis losses.

Effect of External Stress on Magnetic Properties

If external stress is acting on the polycrystalline metal, the influence of the two different factors of the magnetic structure becomes even more obvious. As long as the stress is, for every crystal, below the elastic limit, there will be only the action of the stress on the domains within the shell in the way outlined

above for single crystals. Experimental evidence for this was again provided by powder pattern technique (11, 12). However, as soon as the stress exceeds the elastic limit in any grain, a new mechanism starts because now the mechanical state of the sample changes. Up to this point we could regard the number and size of closed flux shells in a given specimen as constant. These will depend on pretreatment and chemical composition of the metal, but will not change during the various magnetization processes. As soon as plastic deformation starts, this assumption is valid no longer.

A crystal, after deformation, has undergone displacement of the part above the slip plane with respect to the part below. During slip new dislocations can be created in the slip plane and after slip the parts of the crystal now separated by an array of dislocations have a tilt of approximately 10 to 15 min. of arc. These changes in the mechanical state also change the magnetic properties.

There are numerous experimental results showing how the ferromagnetic behavior of a metal under stress changes abruptly when the stress exceeds the elastic limit. This is much easier to understand with our model in mind.

The direction of slip is for most metals a direction of hard magnetization. The dislocations in the slip plane, the aggregation of foreign atoms around these dislocations, the angular displacement of one crystal part with respect to its neighbor, all these will make the slip plane and its vicinity not only a new boundary in the crystallographic sense but also a new shell surface in the ferromagnetic sense. The original closed flux shell will split into two new shells and the slip plane will be the new shell surface.

The basic assumption of this model is that the lattice discontinuities, which are formed in the course of plastic deformation, not only separate two regions of different crystallographic orientation, but also two different closed flux regions.

In support of this assumption, there is first of all the experimental evidence afforded by numerous observations of the change in magnetic properties of metals under stress.

There are two principle types of experiments being carried out to relate the changes in magnetic properties of a metal to its mechanical characteristics:

The experiments of the first type measure the magnetization curve of the sample at a given constant stress. The observed change in magnetic properties is then related to the changes in the mechanical state. The results of these types of experiments are obtained by measuring magnetic properties under a known load that remains constant during the individual measurement. That must be kept in mind when studying these data, even where they are eventually plotted as magnetic properties *vs.* stress. The experiments of the second type are of another nature. Here an attempt is made to record structure sensitive properties *during* the course of loading in order to follow the process of mechanical changes.

The structure sensitive property recorded in Type II is usually the effective coercive force obtained by measuring the hysteresis loop at low frequencies and low fields, by recording the core losses in a sample in a very weak field and at frequencies of several kilocycles or by similar setups.

Type I contains the classical experiments on the influence of stress on magnetic properties by Ewing, Becker, and others (1).

The conditions of these experiments make it difficult to follow the changes near or above the elastic limit of the metal, but, even so, they indicate the complete change in magnetic behavior of a plastically deformed metal. Fig. 1 shows the change in induction under stress and illustrates the rapid change in the neighborhood of the elastic limit (6).

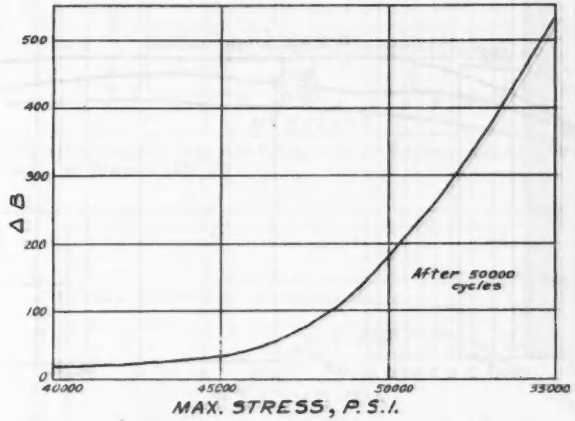

FIG. 1. *Change in magnetic induction of steel under tension. M. F. Fischer, 1928 (6).*

Figs. 2 and 3 show the results of experiments somewhat in between Types I and II (8). Here the change in induction is recorded for a specimen under repeated constant loading. The induction remains constant as long as the load is below the elastic limit. The slight initial increase is due to relief of internal stress during the first period of loading. As soon as the stress reaches the elastic limit of the metal, the induction increases abruptly. If repeated loading in this range is applied for a short enough interval so that failure does not occur, the magnetic characteristics of the metals change completely after removal of the load, as shown in Fig. 3.

Fig. 4 gives a record of an experiment representative for Type II (4). In this case the diameter of the minor hysteresis loop under low frequencies (125 c.p.s.) and low fields was measured for steel samples. The samples were loaded above the elastic limit (5). The load was released at the same speed, and the loading process was then repeated in the same way. The solid curve

corresponds to loading, the dotted curve to unloading. Under the given experimental conditions, the X-axis intercept of the hysteresis loop is inversely proportional to the effective coercive force. This means that the effective coercive force of the original sample remains constant till the load reaches about 5000 lb. Here too, initial increases at low loads occur sometimes, owing to the relief of interal stresses.

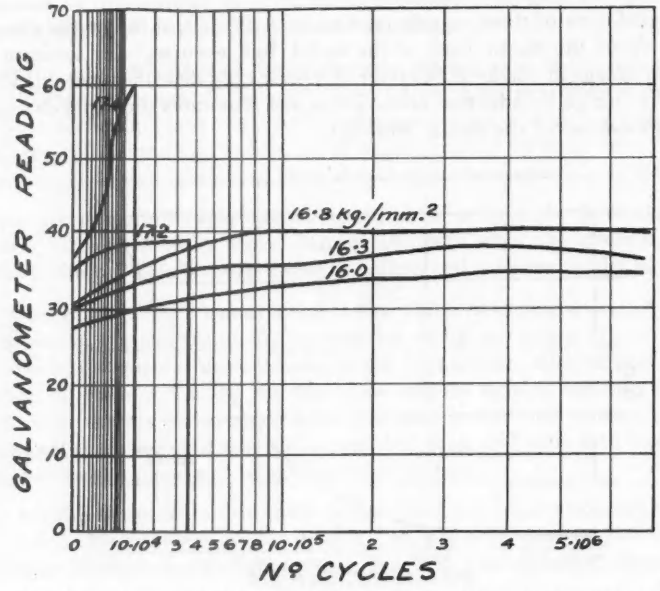

FIG. 2. *Change in magnetic induction during repeated loading. E. Moench, 1940 (8).*

The data obtained at the first low loading depend on the individual mechanical state of the sample, whereas the remainder of the curve is rather independent of individual variations and representative for the general behavior of steel under stress. A further increase in load gives a sharp increase in effective coercive force at a stress level which is below the elastic limit. This increase is due to mechanical changes initiated by the start of plastic deformation in the individual crystals. Relief of the load brings first a slight decrease in the effective coercive force because of the mechanical recovery of the metal and the corresponding decrease of the internal demagnetization field. This process is completed around 5000 lb. and the effective coercive force, now larger than in the undeformed metal, remains constant till the load has decreased to about 3000 lb. Further removal of the load brings a sharp increase in effective coercive force.

This increase, which can be overcome by renewed loading, can be explained as follows: In our model, plastic deformation means that some of the original

closed flux shells are split up into new smaller shells. The creation of new shell surfaces results in the formation of new surface domains which have 90° walls toward the basic domains. These basic domains are separated by 180°

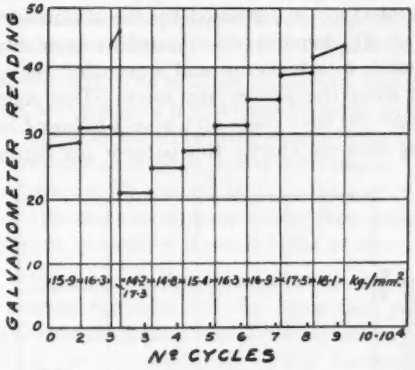

FIG. 3. *Change in magnetic induction during repeated loading. Load briefly increased above the elastic limit. E. Moench, 1940 (8).*

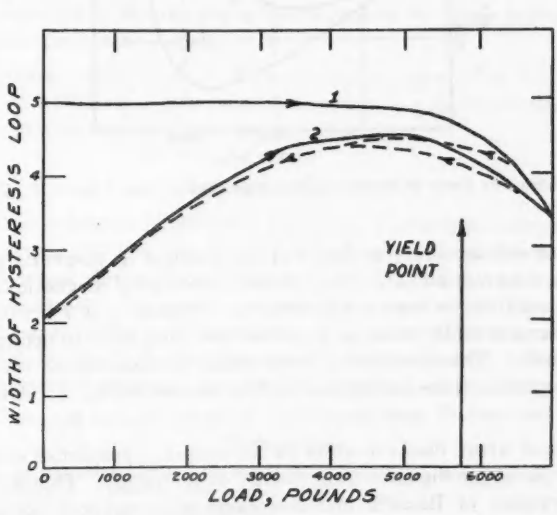

FIG. 4. *Width of minor hysteresis loop under increasing tension (3).*

walls. As far as the action of the stress is concerned, magnetic domains separated by 180° walls are symmetrical toward the direction of stress and their volume will not change under external stresses. Domains separated by 90° walls, however, are affected by external stresses. Those favorably oriented

toward the direction of stress will grow by wall movement at the expense of those unfavorably oriented.

The effective coercive force which we measure by following the hysteresis loop can be pictured as being proportional to the resistance against wall displacement. This resistance is decreased by the action of the stress on the 90° walls. When all 90° domains are oriented as favorably to the direction of stress as it is possible to achieve by wall movement, the additional effect of the stress does not enter the picture any more. This stage is reached at a load of about 3000 lb. and from there on Curve 2 follows Curve 1. Repeated or decreased loading does not change this pattern any further.

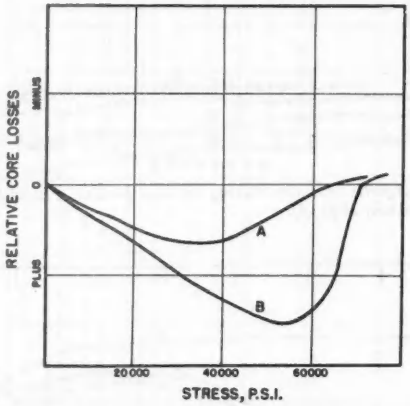

FIG. 5. *Relative core losses under increasing tension (weak field, 5 kc.). P. E. Cavanagh, 1946 (4).*

Fig. 5 gives similar direct evidence of the changes in magnetic properties under plastic deformation (3). They show recordings of magnetic core losses under stress obtained in very weak fields of a frequency at 7 kc. (Curve A). The losses increase under stress as expected and then start to decrease below the elastic limit. This decrease in core losses corresponds to the decrease in effective coercive force during plastic deformation in Fig. 4. After plastic deformation the over-all core losses have increased (Curve B).

The effects of lattice discontinuities on the magnetic properties will be more pronounced the larger the anisotropy energy of the metal. This is confirmed by an observation of Bozorth and coworkers who reported domains in a material of low anisotropy energy going right across grain boundaries as an exceptional case (2).* Williams showed the appearance of new lines in the powder pattern of plastically deformed permalloy crystals. These lines remained even after repeated magnetization and demagnetization and reapplication of the colloid in the same place on the crystal. They could not be observed without the application of the colloid. Williams relates these lines

* *The Ontario Research Foundation is indebted to Dr. Bozorth for this private communication.*

to the plastic deformation of the crystal and suggests the use of the powder technique to observe early stages of plastic deformation (11, 12).

It seems rather obvious that these lines are new shell surfaces created by plastic deformation at the slip plane, since they cannot be displaced by a magnetic field. Shell surfaces separate different regions of closed flux, so it should be possible to detect them by means of the powder technique.

Néel has derived the structure of domains around impurities or cavities in ferromagnetic metal, and Williams has obtained powder pictures which verified Néel's prediction. There seems to be little doubt that, if these impurities or cavities or their arrangements have linear dimensions comparable to the dimensions of the domains, this would lead to the formation of a new shell surface, surface domains and two separate closed flux configurations. We are going to carry out more quantitive investigations in this line.

The concept of a closed flux shell outlined above seems to be consistent with the present experimental material and the theoretical picture of the ferromagnetic as well as of the mechanical properties of the metal. It is suggested as an explanation of the discontinuities of the ferromagnetic behavior of plastically deformed metals. It helps us to visualize the effects of plastic deformation on magnetic properties and attempts to provide means for consistent application of the results of investigations on single crystals to polycrystalline ferromagnetic metals.

The necessary conditions of crystallographic orientation and anisotropy energy which will cause a given slip plane to act as a shell boundary are going to be derived quantitatively in a forthcoming paper.

Acknowledgments

The author is greatly indebted to Mr. P. E. Cavanagh, Assistant Director of the Department of Engineering and Metallurgy, Ontario Research Foundation, under whose direction this work was carried out, for his constant help and encouragement. Stimulating discussions with Prof. B. Chalmers of the Department of Metallurgical Engineering, University of Toronto, and with Dr. O. W. Ellis, Director of the Department of Engineering and Metallurgy, Ontario Research Foundation, are equally thankfully acknowledged.

References

1. BECKER, R. and DÖRING, W. Ferromagnetismus. Verlag von Julius Springer, Berlin; reprinted J. W. Edwards, Ann Arbor. 1939.
2. BOZORTH, R. M. Private communication.
3. CAVANAGH, P. E. Trans. Am. Soc. Metals, 36: 137. 1946.
4. CAVANAGH, R. L. Unpublished results.
5. COTTRELL, A. H. Progress in metal physics. Butterworths Scientific Publications, London. 1949.
6. FISCHER, M. F. Bur. Standards J. Research, 1: 721. 1928.
7. KITTEL, C. Rev. Modern Phys. 21: 541. 1949.
8. MOENCH, E. Forsch. Gebiete Ingenieuru. 11: 324. 1940.
9. NÉEL, L. J. phys. radium, 5: 241. 1944.
10. READ, W. T. and SHOCKLEY, W. Phys. Rev. 78: 275. 1950.
11. WILLIAMS, H. J., BOZORTH, R. M., and SHOCKLEY, W. Phys. Rev. 75: 155. 1949.
12. WILLIAMS, H. J. and SHOCKLEY, W. Phys. Rev. 75: 178. 1949.

THE ANGULAR CORRELATION OF ANNIHILATION RADIATION[1]

By P. E. Argyle and J. B. Warren

Abstract

The angular distribution of annihilation radiation from copper 64 has been measured with a pair of scintillation counters in coincidence. Coincidences were found when the counters and source were not quite collinear. The relation between the noncollinear coincidence rate and angle of deviation λ could be closely approximated to by an exponential of the form $e^{-\lambda/\lambda_0}$, where $\lambda_0 = (3.60 \pm 0.04)\ 10^{-3}$ radian. Interpreting this departure from antiparallelism of the two photons as arising from the residual motion of the annihilating pair, the average momentum of their mass center in copper is found to be $(7.20\ mc.) \times 10^{-3}$ which corresponds to an electron energy of 13.2 ev., if the positron is assumed to be thermalized before annihilation.

Introduction

By 1934 the general predictions of the Dirac theory as to the properties of positive electrons had been verified. Since then only a few of the finer details of the behavior of positrons have been investigated. One of these, the exactness of the collinearity of the two annihilation quanta, was investigated by Beringer and Montgomery in 1942 (1) who found no evidence for any lack of collinearity within the angular resolution of their experiment. It seemed worth while to repeat this experiment using scintillation counters and a stronger source, to ascertain whether all positrons are thermalized before annihilation and to obtain the order of magnitude of the momentum of the center of gravity of the pair at the moment of annihilation.

Our measurements are similar to those recently described by DeBenedetti *et al.* (2) and our results are in agreement with theirs.

Experimental Arrangement

Two scintillation counters, one fixed and one mounted on a traveling microscope carriage, movable in a horizontal direction were placed on either side of, and 200 cm. from, a strong copper 64 source. The source, about 40 millicuries in strength at the start of the experiment, was a piece of copper 6 by 3 by 0.6 mm. irradiated in the Chalk River pile. The length of the source parallel to the line joining the counters was limited to 6 mm. to avoid attenuation of the annihilation radiation but this was sufficient to stop most of the positrons by self-absorption. No heavy absorbing material was placed over the copper to stop positrons emerging, since the thickness required would be such that more annihilation radiation would be absorbed than produced and the angular resolution of the apparatus would be reduced owing to the increase in source width. The copper was supported in a thin aluminum frame. The whole

[1] *Manuscript received August 23, 1950.*
Contribution from the Department of Physics, University of British Columbia, Vancouver, B.C.

source was small in comparison with the detector size so that corrections for source size were unnecessary.

Two clear rectangular blocks of naphthalene 2 by 1 by 1 in. were used as phosphors with a pair of RCA 5819 photomultipliers. The tubes were run at a relatively low potential (900 to 1000 volts), obtained from a battery referenced stabilized supply, and were cooled via their bases with solid carbon dioxide. This simple cooling reduced the noise background count, with the discriminator setting used, to about 40/sec., a negligible amount.

The output pulses were fed via head and main amplifiers (rise time of 0.2 μsec.) into a conventional mixer of resolving time 0.30 μsec. and with recovery time set at 20 μsec., the longest dead time in the electronics. Care was taken to minimize overshooting in the amplifiers by the use of diode pumps.

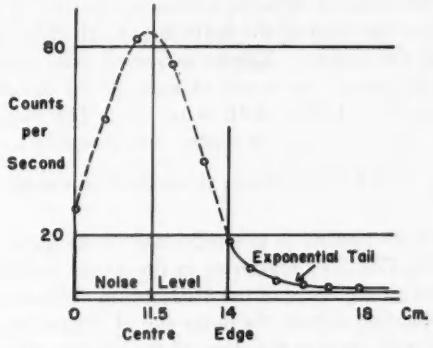

FIG. 1. *Plot of coincidence rate against displacement.*

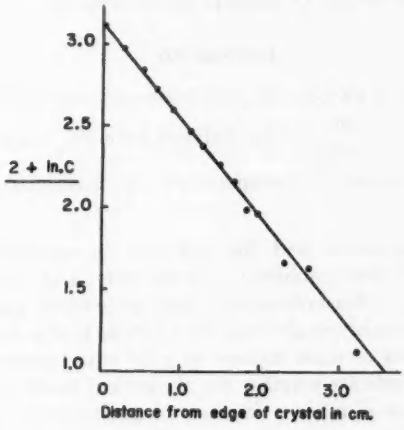

FIG. 2. *Logarithmic plot of tail of coincidence rate-displacement curve.*

Procedure

After careful alignment of the detectors and source the coincidence rate and the rates in each channel were recorded as a function of the horizontal displacement of the movable detector. Corrections for accidentals, dead time losses, and source decay were made to the observed coincidence rate in that order. Fig. 1 gives the general shape of the curve obtained and Fig. 2 a logarithmic plot of the exponential tail. The method of least squares was used to obtain the best slope, each point being weighted by the factor $\left(\frac{\text{count}}{\text{standard deviation}}\right)^2$.

Results

It was found that the tail of the distribution curve could be accurately represented by an exponential form, $e^{-\lambda/\lambda_0}$, where $\lambda_0 = (3.60 \pm 0.04)\ 10^{-3}$ radian and λ is the angle of departure from collinearity of the two photons. This value includes the effect of the finite angles subtended in the two planes by the crystal at the source. The reduction of this measured curve to a momentum distribution of the center of mass of the annihilating pairs was done by the method of DeBenedetti *et al.* (2). The mean center of mass momentum for annihilating pairs in copper corresponding to this value of λ_0 is $p_{cu} = 0.98 \times \frac{mc.}{137}$ which is equivalent to an electron energy of 13 ev.

No corrections were applied in this reduction of the measured curve for the effect of small angle Compton scattering in the source nor for the effect of the finite detector sizes on the shape of the distribution. The Compton scattering would raise the counting rate at the outer end of the tail by about 1% which would not significantly change the slope of the curve. The effect of the size of the naphthalene blocks is to flatten the distribution curve, which might decrease the slope of the tail by perhaps as much as 5%.

Discussion

The value obtained lies within the probable experimental error of Dumond (4) who gives a value of $1.1\ \frac{mc.}{137}$ for p_{cu} deduced from the wave length profile of the annihilation radiation. It compares with DeBenedetti's value of 1.2 for gold.

The result is in agreement with the view that the majority of the positrons are thermalized and then annihilate with the outer and conduction electrons in the copper lattice. Measurements of this type in which positrons are slowed down in different materials would thus yield data as to the energies of the outer electrons, information of some interest in solid state theory. Thus far this technique does not indicate whether the theoretical predictions (5) regarding the annihilation of a significant fraction of positrons in rapid motion are

correct (3), since the maximum center of mass momentum observed corresponded to an energy of about 500 ev.

Acknowledgments

One of us (P.E.A.) was assisted by a grant from the National Research Council of Canada during this work which was carried out in partial fulfillment of the requirements for a Master of Arts degree at this University. This work was carried out in the Nuclear Physics Techniques Laboratory set up with the generous assistance of the Defence Research Board.

References

1. BERINGER, R. and MONTGOMERY, C. G. Phys. Rev. 61: 222. 1942.
2. DEBENEDETTI, S., COWAN, C. E., KONNEKER, W. R., and PRIMAKOFF, H. Phys. Rev. 77: 205. 1950.
3. DEUTSCH, M. Phys. Rev. 72: 729. 1947.
4. DUMOND, J. W. M., LIND, D. A., and WATSON, B. B. Phys. Rev. 75: 1226. 1949.
5. HEITLER, W. The quantum theory of radiation. 2nd ed. Oxford University Press. 1944. p. 230.

THE SCATTERING LENGTHS OF THE DEUTERON[1]

By D. G. Hurst and N. Z. Alcock

Abstract

The angular variation of the scattering of neutrons of 0.0724 ev. energy by deuterium gas has been measured. Comparison with theoretical calculations of this variation gives a ratio of scattering lengths:

$$a_{\frac{1}{2}}/a_{\frac{3}{2}} = 0.12 \pm 0.04 \text{ or } 3.2 \pm 0.3.$$

In combination with the known total scattering cross section of the free deuteron of 3.44 ± 0.06 barns this gives for the scattering lengths the two sets of values:

$$\left.\begin{aligned} a_{\frac{1}{2}} &= 0.07 \pm 0.03 \\ a_{\frac{3}{2}} &= 0.638 \pm 0.006 \end{aligned}\right\} \text{ or } \left.\begin{aligned} &0.826 \pm 0.012 \\ &0.26 \pm 0.02 \end{aligned}\right\} \times 10^{-12} \text{ cm.}$$

I. Introduction

Information about molecular structures and nuclear properties may be obtained from measurements of slow neutron scattering by gases. Preliminary measurements at Chalk River on oxygen and carbon dioxide gases (1) showed the feasibility of measuring the scattered neutron intensity as a function of angle. Consequently further work was undertaken with a new spectrometer; and in the present paper, a precise measurement of the angular variation of scattering by deuterium is reported.

The scattering and absorption of slow neutrons by free deuterons is completely defined by two scattering lengths (5), $a_{\frac{3}{2}}$, and $a_{\frac{1}{2}}$ corresponding to the two possible spins 3/2 and 1/2 of the compound nucleus. In general, scattering lengths are complex, but when absorption is negligible, as is the case with deuterium, they are real. Accurate values of these scattering lengths are of interest for they are quantities with which theories of nuclear forces may be compared.

The structure of the deuterium molecule is well known. The expected scattering has been calculated by the methods of Hamermesh and Schwinger (8, 9) and Spiers (16, 17), and in addition corrected for the ground state vibration. Comparison with the measured scattering gives the value of $(a_{\frac{3}{2}} - a_{\frac{1}{2}})^2(2a_{\frac{3}{2}} + a_{\frac{1}{2}})^{-2}$. This is a quadratic function of the ratio $a_{\frac{1}{2}}/a_{\frac{3}{2}}$ and has two roots. The scattering lengths corresponding to each of these roots are obtained by combining each value of $a_{\frac{1}{2}}/a_{\frac{3}{2}}$ with σ_T, the measured total cross section of free deuterons (6) which is equal to $4\pi\ (\frac{2}{3}a_{\frac{3}{2}}^2 + \frac{1}{3}a_{\frac{1}{2}}^2)$. This leads to four values of each scattering length. Two of these are eliminated by the crystal diffraction result, discussed in the next paragraph, that $2a_{\frac{3}{2}} + a_{\frac{1}{2}}$ is positive. The remaining ambiguity could be resolved only by experiments with polarised neutrons (8).

Two previous investigations in principle give the scattering lengths, but owing to lack of precision the authors did not carry the analysis to this end.

[1] *Manuscript received August 22, 1950.*
Contribution from the Atomic Energy Project, National Research Council of Canada, Chalk River, Ontario, Canada. Issued as N.R.C. No. 2284.

Shull *et al.* (15) using the diffracted intensity from powdered sodium deuteride, and later thorium deuteride (Wollan *et al.* (18)) obtained the coherent scattering length $f_D = \frac{3}{2}(\frac{2}{3}a_{\frac{1}{2}} + \frac{1}{3}a_{\frac{1}{2}})$ and showed that it is positive. A measured value of f_D combined with a measured σ_T gives the scattering lengths. Fermi and Marshall (6) measured the transmission cross section of deuterium gas for very low energy neutrons, and the total cross section of the free deuteron. From the results, they gave rough limits for the ratio $a_{\frac{1}{2}}/a_{\frac{3}{2}}$ and showed that it is positive. In Section VI(*b*) below, a comparison is made of these methods with the present work.

II. Theory

(*a*) *The Deuterium Molecule*

The deuterium molecule is diatomic, with identical nuclei having spin 1. Owing to the symmetry properties of the molecule, there are two parities, depending on whether J, the quantum number of the rotational state, is even or odd. States of even J are called orthodeuterium, and odd J paradeuterium.

The rotational energy of the state of quantum number J is

$$E_J = \frac{(h/2\pi)^2}{2\,M r_e^2} J(J+1) = E_1 \frac{J(J+1)}{2}$$

where h = Planck's constant,
M = mass of the hydrogen atom,
r_e = separation of the nuclei in a rigid model of the molecule.

At a temperature T the Jth state has statistical weight

$W_J = G(2J+1)\exp(-E_J/k_bT)$
$G = 6$ for J even,
$= 3$ for J odd,
k_b = Boltzmann's constant.

The gas contains 66.7% orthodeuterium at room temperature, 70.3% at liquid nitrogen temperature. Transitions between the two parities are very rare and are of importance only under the action of catalysts. When the gas is cooled from room temperature the new equilibrium is set up slowly.

In addition to rotational states, the molecule possesses vibrational states. The excitation energy of the vibrational states is so large that in the scattering gas only the ground state occurs. The wave function of the ground state extends over about one tenth of the internuclear separation. This modifies the neutron scattering in that the scattering material is not confined to a thin spherical shell as on the "rigid" model.

The Maxwellian distribution of the velocities of the molecules influences the scattering by affecting the relative momentum of the neutron and molecule. At room temperature, the motion of molecules of average velocity causes a difference in the effective neutron wave length of about $\pm$ 30% for the extremes of motion away from and towards the neutron. At lower temperatures, the spread of effective wave lengths is correspondingly reduced. For this reason, and to have few rotational states excited, the experiments were performed at low temperature.

(*b*) *Outline of the Calculations*

The basic formulas for the scattering of neutrons by deuterium were derived by Hamermesh and Schwinger (8) who were concerned mainly with the behavior of the total cross section. To put their results for the differential cross sections into suitable form to compare with our measurements required that the cross sections be transformed from the center of mass system to the laboratory system, and averaged over the Maxwell distribution of molecular velocities.

Spiers has done this (16) and gives the cross sections for molecules at rest for scattering angles between 0° and 180° and the averaged cross sections for molecules in a gas at a temperature of 90°K. (liquid oxygen temperature) at scattering angles of 30°, 60°, 90°, 120°. From his report the region of scattering angles between 10° and 70° was chosen as the most promising for an experimental determination of the ratio of scattering lengths. Accordingly a second set of cross sections was computed for a gas temperature of 77.4°K. at angles of 10°, 30°, 50°, 70°. The temperature 77.4°K. is the temperature of liquid nitrogen, the refrigerant used in the experiment.

There is a partial cross section for each transition $J \rightarrow J'$. These partial cross sections have to be summed over all J' and J, the statistical weights being applied in the sum over J. The result is a differential cross section $\sigma(\phi)$ expressed as a linear combination of two quantities σ_A and σ_B which can be calculated without a knowledge of the scattering lengths. Thus

$$\sigma(\phi) = A\sigma_A(\phi) + B\sigma_B(\phi), \tag{1}$$

ϕ being the angle of scattering in the laboratory system. The scattering lengths occur only in the coefficients A and B.

The measured scattering $s(\phi)$ should be proportional to $\sigma(\phi)$ and we may write $cs(\phi) = A\sigma_A + B\sigma_B$ which transforms to $\dfrac{s(\phi)}{\sigma_B} = (A\sigma_A/\sigma_B + B)/c$, where c is a constant of the apparatus. A plot of $s(\phi)/\sigma_B$ against σ_A/σ_B should be a straight line cutting the axis of abscissas at $-B/A$. From B/A the value of $a_{\frac{1}{2}}/a_{\frac{3}{2}}$ can be found.

The calculations on which σ_A, σ_B are based assume a rigid molecule. The effect of the ground state vibration of the molecule was calculated and the experimental intensities were modified before comparison with σ_A, σ_B.

The next section contains the details of the calculation of σ_A and σ_B and the subsequent section is the discussion of the vibration correction.

(*c*) *Cross Sections Averaged over the Thermal Motion*

In the center of mass system, the differential cross section for scattering of a neutron of momentum p_0 through an angle θ by a deuterium molecule which undergoes a transition as the result of the scattering, the rotational quantum number changing from J to J', is (16)

$$\sigma_{JJ'}(\theta, p_0) = \mu (2J' + 1) \frac{p}{p_0} \sum_L (2L + 1) C_{LJJ'} j_L^2(kr_e),$$

where p is the momentum of the neutron after the collision and differs from p_0 because of the difference of energies of the rotational states. Assuming a rigid molecule having the nuclei at a separation r_e

$$p^2 = p_0^2 + 4/5 \frac{(h/2\pi)^2}{r_e^2}\Big[J(J+1) - J'(J'+1)\Big].$$

The values of L are $|J - J'|, |J - J'| + 2, \ldots, J + J'$. The coefficients $C_{LJJ'}$ are discussed in references (8) and (16). k is the magnitude of the vector $\boldsymbol{k}$ given by

$$h\boldsymbol{k} = \pi(\boldsymbol{p}_0 - \boldsymbol{p})$$

$j_L(x)$ is the spherical Bessel function of order $L + 1/2$, μ is determined by the scattering lengths $a_{3/2}$ and $a_{1/2}$. They enter in the combinations

$$(2a_{3/2} + a_{1/2})^2 = A$$
$$(a_{3/2} - a_{1/2})^2 = B$$

and μ depends on the initial and final states according to Table I.

TABLE I

THE QUANTITY μ FOR THE POSSIBLE TYPES OF TRANSITION

Transition	J J'	μ
Ortho-ortho	Even – even	$\frac{16}{25}$ $(A + (5/4)\ B)$
Para-para	Odd – odd	$\frac{16}{25}$ $(A + (1/2)\ B)$
Ortho-para	Even – odd	$\frac{16}{25}$ $(3/4)\ B$
Para-ortho	Odd – even	$\frac{16}{25}$ $(3/2)\ B$

In terms of a function

$$P_{JJ'}(x) = (2J' + 1) \sum_L (2L + 1) C_{LJJ'} j_L^2(x)$$

the formula may be written

$$\sigma_{JJ'}(\theta, p_0) = \mu \frac{p}{p_0} P_{JJ'}(k r_e). \tag{2}$$

Formula (2) is fundamental for the subsequent work. It gives the cross section in the center of mass system for a neutron of arbitrary momentum p_0. Transforming to a system in which the molecule is moving with a velocity V and the neutron with momentum p_0' equal to the incident neutron momentum in the laboratory, and averaging over all V according to the Maxwell distribution, gives the required cross section corrected for thermal motion.

Spiers shows how to integrate over two components of the velocity, and the resulting formula is

$$\sigma_{JJ'}(\phi) = \mu g \int_0^{\pi - \phi} X(a) P_{JJ'}(\eta) e^{-\eta^2} da, \tag{3}$$

where ϕ is the angle of scattering in the laboratory system. The variables are expressed in terms of the angle α between the vectors $\boldsymbol{p}_0'$ and $\boldsymbol{k}$. If

$$
\begin{aligned}
E &= \text{energy of incident neutrons,}\\
E_1 &= \text{energy of first rotational state of the molecule,}\\
T &= \text{temperature of the gas,}\\
\text{then}\quad g &= \frac{25}{8}\sqrt{\frac{E}{\pi k_b T}}\,,\\
\gamma &= 25E/4k_bT,\\
X(\alpha) &= \sin^2\alpha \operatorname{cosec}^3(\alpha+\phi),\\
\xi &= 0.8\cos\alpha - 0.5\sin\phi \operatorname{cosec}(\alpha+\phi),\\
&\quad + 0.2(E_1/E)\,[J(J+1) - J'(J'+1)]\sin(\alpha+\phi)\operatorname{cosec}(\phi),\\
\eta &= \sqrt{(E/2E_1)}\sin\phi\operatorname{cosec}(\alpha+\phi).
\end{aligned}
$$

To keep all errors in the computations less than the experimental error, it was necessary to carry out numerical integrations using Equation (3). For each integration 11 values of α were taken at 5 degree intervals, with α_0 as the mid-point where α_0 is the value of α for which $\xi = 0$. Simpson's rule was applied to get the integrals. Although the number of points used in the integrations is small, the shape of the curve is such that Simpson's rule should give the areas accurately. Thirty-six partial cross sections were corrected in this way for thermal motion. Values for molecules at rest taken from Spiers' report were used for other cross sections which contribute only slightly to the final results.

Apart from general physical constants the quantities required for the computation are T the temperature of the gas, E the energy of the incident neutrons, and E_1 the energy of the first rotational state of the molecule.

T was assumed to be the temperature of liquid nitrogen, 77.4°K., for reasons discussed in Section III*b* below. In any case the temperature has only a small influence on the result and a considerable departure from this temperature would cause no serious error.

The value of E used in the calculations was 0.07 ev. Although this differs somewhat from the experimental value 0.0724 ev. as measured by crystal diffraction, (Section IV), it allowed a direct comparison to be made with Spiers' results which were based on 0.07 ev. Also it was not convenient, at the time the computing was begun, to settle on a final value.

E_1 was taken to be 0.007416 ev. and determines the internuclear separation r_e in a rigid molecule by the formula $r_e = (h/2\pi)/\sqrt{ME_1} = 0.747 \times 10^{-8}$ cm. The correction for vibration was based on a molecule having the separation r_0, the value of r for the maximum density of the zero point vibration. Consequently r_0 should have been used in the calculations instead of the r_e which is implicit in E_1. The relationship is $r_0 = 1.0056\, r_e$.

To allow for the above alterations in neutron energy and internuclear separation, the theoretical cross sections were taken to apply to angles differing

slightly from the angles used in the computing. The basis for this change is that kr_e is the variable that determines the angular variation of cross section, and to a sufficient approximation kr_e is proportional to $r \sin(\theta/2)/\lambda$. With the new values of r and λ, θ was changed to keep this quantity unaltered. The values of θ were then transformed to the laboratory system giving the new angles.

For each transition $J \rightarrow J'$ and angle ϕ the quantity computed is $\sigma_{JJ'}(\phi)/\mu = S_{JJ'}$. The sum of $\sigma_{JJ'}$ over J' is

$$\sigma_J = \frac{16}{25} \begin{cases} \left(A + \frac{5}{4}B\right)\sum_{J' \text{ even}} S_{JJ'} + \frac{3}{4}B \sum_{J' \text{ odd}} S_{JJ'} & \text{even } J \\ \left(A + \frac{1}{2}B\right)\sum_{J' \text{ odd}} S_{JJ'} + \frac{3}{2}B \sum_{J' \text{ even}} S_{JJ'} & \text{odd } J \end{cases}$$

as can be seen from Table I.

The σ_J's are added according to the statistical weight of the Jth state. The ratio of ortho to paradeuterium was not determined experimentally and consequently the statistical weights are not known exactly. The extreme cases, however, correspond on the one hand to room temperature (2/3 ortho, 1/3 para) and on the other hand to 77.4°K. (70.3% ortho, 29.7% para). The first case will be called "normal" the second case "equilibrium" mixture. The fraction of molecules in a state J is either

$$f_J = \frac{W_J}{\sum W_J} \quad \text{for equilibrium mixture}$$

or $f_{J\,(\text{even})} = 2W_J/(3\sum_{J\,\text{even}} W_J)$; $f_{J\,(\text{odd})} = W_J/(3\sum_{J\,\text{odd}} W_J)$ for normal mixture. In all cases W_J is computed for a temperature of 77.4°K.

The cross section per molecule is

$$\sigma = \sum_J \sigma_J f_J$$

and this becomes $\sigma = A\,\sigma_A + B\,\sigma_B$

where $$\sigma_A = \frac{16}{25}\left\{ \sum_{J\,\text{even}} f_J \sum_{J'\,\text{even}} S_{JJ'} + \sum_{J\,\text{odd}} f_J \sum_{J'\,\text{odd}} S_{JJ'} \right\}$$

$$\sigma_B = \frac{16}{25}\left\{ \sum_{J\,\text{even}} f_J \left(\frac{5}{4}\sum_{J'\,\text{even}} S_{JJ'} + \frac{3}{4}\sum_{J'\,\text{odd}} S_{JJ'}\right) + \sum_{J'\,\text{odd}} f_J \left(\frac{3}{2}\sum_{J'\,\text{even}} S_{JJ'} + \frac{1}{2}\sum_{J'\,\text{odd}} S_{JJ'}\right)\right\}.$$

In Table II are tabulated the $S_{JJ'}$ for molecules at rest and for a gas temperature 77.4°K. The percentage contribution of each transition to the σ_A and σ_B is included. It is interesting to note that at small angles the scattering is almost entirely elastic, but that at larger angles inelastic scattering predominates. This has the consequence that changes in parity can be of importance only at the larger angles. The two sets of σ_A, σ_B for "normal" and "equilibrium" mix-

tures corrected for thermal motion are in Table III. From the experimental results the ratio of the scattering lengths was found to differ by 5.6% depending on whether "normal" or "equilibrium" mixture is assumed. Values

TABLE II

THE SCATTERING FACTORS $S_{JJ'}$

J	J'	$S_{JJ'}$		Percentage contribution	
		Molecules at rest	Gas temperature, 77.4°K.	to σ_A*	to σ_B*
(*a*) *Scattering angle* $\phi = 10°$					
0	0	(1.480)**	1.496	59.4	68.6
0	1	(0.0727)	0.0751		2.1
0	2	(0.0022)	0.0027	0.1	0.1
0	3	0.0005			0.01
1	0	(0.0279)	0.0287		0.8
1	1	(1.480)	1.497	29.3	13.5
1	2	(0.0583)	0.0613		1.6
1	3	0.0062		0.1	0.06
2	0	0.0005			
2	1	(0.0429)	0.0445		0.2
2	2	(1.480)	1.495	10.6	12.2
2	3	0.0749			0.4
2	4	0.0253		0.2	0.2
3	0	0			
3	1	0.0018			
3	2	0.0603			0.02
3	3	1.486		0.3	0.1
3	4	0.0927			0.03
(*b*) *Scattering angle* $\phi = 30°$					
0	0	(0.9604)	0.9618	57.2	48.7
0	1	(0.4376)	0.4473		13.6
0	2	(0.0344)	0.0363	2.2	1.8
0	3	0.0029			0.08
1	0	(0.1690)	0.1724		5.2
1	1	(0.9770)	0.9800	28.8	9.8
1	2	(0.2762)	0.2828		8.5
1	3	0.0240		0.7	0.3
2	0	0.0136		0.1	0.1
2	1	(0.2206)	0.2254		1.2
2	2	(0.9723)	0.9741	10.3	8.7
2	3	0.2479			1.3
2	4	0.0392		0.4	0.4
3	0	0.0005			
3	1	0.0226			
3	2	0.2537			0.07
3	3	0.9634		0.3	0.08
3	4	0.2256			0.06

* *The* σ_A, σ_B *are for equilibrium at 77.4°.*

** *Values in brackets ( ) were not used in the calculations.*

TABLE II—*Continued*

THE SCATTERING FACTORS $S_{JJ'}$

J	J'	$S_{JJ'}$		Percentage contribution	
		Molecules at rest	Gas temperature, 77.4°K.	to σ_A*	to σ_B*
(*c*) *Scattering angle* $\phi = 50°$					
0	0	(0.4109)	0.4054	44.6	24.7
0	1	(0.6718)	0.6803		24.8
0	2	(0.1285)	0.1331	14.6	8.1
0	3	0.0110			0.4
1	0	(0.2542)	0.2566		9.2
1	1	(0.4835)	0.4807	26.1	5.8
1	2	(0.4220)	0.4280		15.4
1	3	(0.0637)	0.0621	3.4	0.7
2	0	(0.0511)	0.0530	1.0	0.6
2	1	(0.3286)	0.3323		2.1
2	2	(0.4631)	0.4595	9.0	5.0
2	3	0.3451			2.2
2	4	0.0519		1.0	0.6
3	0	0.0042			
3	1	0.0819		0.04	0.01
3	2	0.3671			0.12
3	3	0.4596		0.2	0.05
3	4	0.3038			0.10
(*d*) *Scattering angle* $\phi = 70°$					
0	0	(0.1160)	0.1112	19.5	8.7
0	1	(0.6062)	0.5956		28.1
0	2	(0.2212)	0.2301	40.3	18.1
0	3	0.0173			.8
1	0	(0.2211)	0.2208		10.3
1	1	(0.2478)	0.2470	21.3	3.8
1	2	(0.3963)	0.3949		18.4
1	3	(0.0933)	0.0931	8.0	1.4
2	0	(0.0893)	0.0920	2.9	1.3
2	1	(0.2952)	0.2953		2.5
2	2	(0.2177)	0.2101	6.5	2.9
2	3	0.3204			2.7
2	4	0.0408		1.3	0.6
3	0	0.01421			0.005
3	1	0.1364		0.1	0.02
3	2	0.3203			0.13
3	3	0.2054		0.2	0.03
3	4	0.2754			0.11

* *The* σ_A, σ_B *are for equilibrium at 77.4°.*

** *Values in brackets ( ) were not used in the calculations.*

of σ_A and σ_B midway between "normal" and "equilibrium" were finally used, introducing at most an error $\pm$ 2.8%. It is possible that the gas was in such an intermediate stage between "normal" and "equilibrium" because at our pres-

sure and temperature and in metal containers the para-ortho hydrogen conversion takes place in a few days (4, page 61).

Before computation of the above results was begun an attempt was made to avoid the numerical integration of Equation (3). γ is so large at 77.4°K. that the main contribution to the integral is from the region close to $\xi = 0$. If the variable is changed from α to ξ the integrand near $\xi = 0$ may be written as a power series in ξ multiplied by $\exp(-\gamma\xi^2)$. An integration of the first few terms between the limits $\pm\infty$ for ξ gives an approximate cross section which seemed at first to be a promising alternative to numerical integration. However, no simple reliable estimate could be made of the error and this method was abandoned, except that cross sections so computed were compared with the results of the numerical integrations as a check for gross errors in the latter.

TABLE III

THE QUANTITIES σ_A, σ_B

Scattering angle	Equilibrium mixture		Normal mixture		Final choice	
	σ_A	σ_B	σ_A	σ_B	σ_A	σ_B
10°	0.9616	1.041	0.9616	1.017	0.9616	1.029
30°	0.6419	0.9421	0.6419	0.9326	0.6419	0.9374
50°	0.3472	0.7843	0.3472	0.7867	0.3472	0.7855
70°	0.2183	0.6069	0.2183	0.6117	0.2183	0.6093

(*d*) *Correction for Molecular Vibration*

The energy difference between vibrational levels is so large (≈ 0.5 ev.) that only the ground state occurs in the gas, and the neutrons have insufficient energy to cause transitions to higher vibrational levels. The scattering may then be treated as being off the probability density of the ground state vibration. This interpretation is in accord with the result of retaining the vibrational wave functions in Equations (10) to (20) of reference (8). (An analogous case is the elastic scattering from a single rotational level as may be seen from Equation (19) of reference (8).)

For a Morse potential (13, page 273) the radial probability density of the ground state vibration is given by

$$Y\,dr = a\sqrt{\frac{b}{2\pi}}\left(1 + \frac{bu^3}{6}\right)\exp\left(-\frac{1}{2}bu^2\right)dr, \tag{4}$$

where $u = a(r - r_0)$,

r_0 = separation of maximum density,

$b = 46.56$,

$a = 1.49/r_0$.

The constants of the deuterium molecule were obtained from reference (4) Table 54.

The difference between the scattering from diatomic molecules having line scatterers with the radial distribution of Equation (4), and diatomic molecules having point scatterers at a fixed separation r_0, was calculated with the result

$$U_{\pm} = \frac{I_{\pm} - I_0}{I_0} = -\frac{0.00244\left\{0.333\,x^2 \pm (0.98 + x^2)\frac{\sin x}{x} \pm 0.98\cos x\right\}}{1 \pm \frac{\sin x}{x}} \quad (5)$$

$I_{\pm}$ is the intensity scattered by the vibrating molecule,
I_0 is the intensity scattered by the rigid molecule,
$x = \dfrac{4\pi r_0 \sin\theta/2}{5\lambda/4}$,
θ = angle of scattering in the center of mass system,
$5\lambda/4$ = neutron wave length in the center of mass system.

The upper signs refer to scattering without change of parity, the lower signs to scattering with change of parity. A semiclassical approximation was used instead of an accurate summation over rotational transitions. This is the same as the method used for calculating X-ray scattering (2, page 159). The molecule was treated as a rigid structure of scatterers, and the intensity of the wave scattered in the direction θ was calculated and then averaged over all orientations of the molecule. The calculation was done in the center of mass system and subsequently transformed to the laboratory system. This method was justified experimentally as an approximation for molecules without nuclear spin (1). Spiers (16, 17) has given a theoretical discussion and has shown that with deuterium, a distinction is necessary between transitions in which the parity is unchanged and transitions in which the parity changes. In the former case the two nuclei scatter identically; in the latter case, a phase difference of 180° is introduced.

The fraction $\bar{U}$ by which the scattered intensity differs from that calculated for a rigid rotator is the weighted mean of U_+ and U_-. The semiclassical formulation (16) for a rigid rotator gives $(1/2)\mu\left(1 + \dfrac{\sin x}{x}\right)$ = sum of $\sigma_{JJ'}$ over J' of same parity as J, $(1/2)\mu\left(1 - \dfrac{\sin x}{x}\right)$ = sum of $\sigma_{JJ'}$ over J' of different parity from J. With the obvious notation $\mu_{00} = \mu$ for ortho-ortho transitions, etc., and with $\omega_{\pm} = (1/2)\left(1 \pm \dfrac{\sin x}{x}\right)$, the differential cross section is

$$\sigma = \sum_J f_J \sum_{J'} \sigma_{JJ'} = \alpha\omega_+ + \beta\omega_- ,$$

$$\text{where } \alpha = \mu_{00} \sum_{J\ even} f_J + \mu_{pp} \sum_{J\ odd} f_J ,$$

$$\beta = \mu_{0p} \sum_{J\ even} f_J + \mu_{p0} \sum_{J\ odd} f_J .$$

The effect of vibration is to change σ to $\sigma(1 + \bar{U})$ and $\omega_{\pm}$ to $\omega_{\pm}(1 + U_{\pm})$. As intensity is proportional to σ it follows that

$$\bar{U} = \frac{\alpha\omega_+ U_+ + \beta\omega_- U_-}{\alpha\omega_+ + \beta\omega_-} .$$

The values of $U_{\pm}$ and $\bar{U}$ are plotted in Fig. 1 as functions of the angle of scattering in the laboratory system.

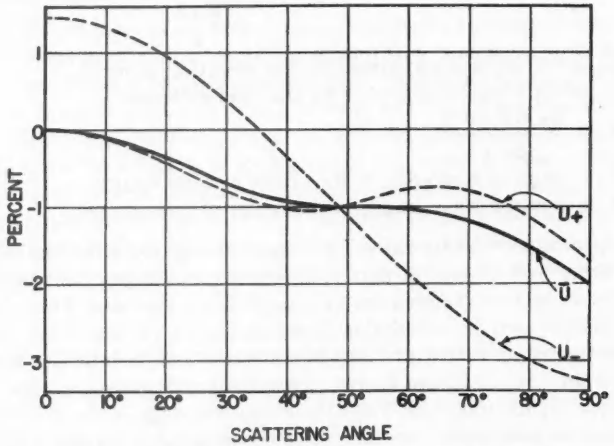

FIG. 1. *The effect of ground state vibration of the molecules. The three curves show the change required in the scattering calculated for a rigid rotator model to yield the correct scattering. U_+ applies when there is no change in parity, U_- when there is change in parity, and $\bar{U}$ is the average for the gas at 77.4°K.*

It is possible to avoid the semiclassical calculation and correct the individual $\sigma_{JJ'}$'s from a comparison of $j_L(kr_e)$ with the average of $j_L(kr)$ over the vibration. The increased labor was not justifiable except for small angles ($< 30°$) where a good approximation is readily obtained. In this region close agreement was found with the semiclassical values. This gives confidence in Fig. 1.

For convenience, the experimental results were modified for comparison with the rigid rotator model, i.e., the experimental results were divided by $1 + \bar{U}$.

III. Apparatus

(*a*) *Spectrometer*

Fig. 2 shows the experimental arrangements used for the gas scattering experiments. A beam of neutrons from the reactor impinged on a sodium chloride crystal set to diffract neutrons having a wave length of 1.063Å. The diffracted beam passed through the scattering cell where a fraction was scattered by the gas. A boron trifluoride counter was used to measure the scattered intensity as a function of scattering angle over the range 11° to 67°. Steel collimators defined the primary, diffracted, and scattered beams. They were 81 in., 13 in., and 14 in. long, respectively, and had 1/2 in. by 1 in. rectangular holes cut down their lengths. Surrounding the first and part of the second collimator was a fast neutron and γ-ray shield of paraffin and barytes and a further layer of steel. Surrounding the third collimator and the counter was a neutron shield of 8 in. of paraffin and 1 in. of boron carbide.

The first collimator formed part of the "hole extender", a 12 ft. tube used to offset the spectrometer from the congested area of the reactor face. Internal details of this extender, not shown in Fig. 2, were irises of boron carbide and lead to reduce radiation in the neighborhood of the extender, and a 12 ft. evacuated tube to prevent reduction of the beam intensity by air scattering.

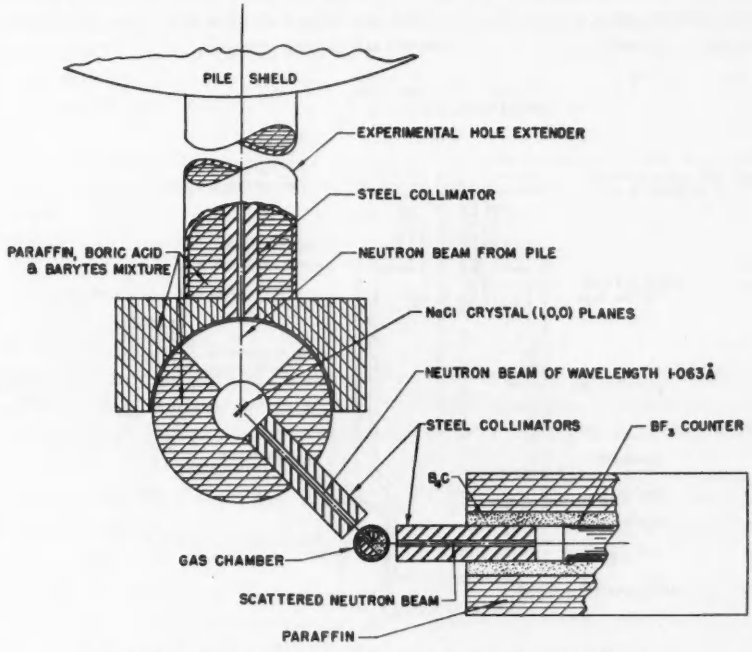

FIG. 2. *Neutron crystal spectrometer as arranged for gas scattering.*

The neutron counter, an enriched boron trifluoride proportional counter 2.5 in. diameter by 25 in. long, has been described previously (7). It should be noted that the counting efficiency is almost independent of neutron energy in the region 0.07 ev. This characteristic was important because the energy of a scattered neutron depended on the scattering angle, the translational energy of the scattering molecule, and any change in rotational energy of the molecule. The range of neutron energies, however, was such that differences in counting efficiency could be ignored.

The spectrometer was operated automatically. A servo-mechanism drove the counter arm through the chosen angular range, setting it at regular 8° intervals with a repeatable angular accuracy of $\pm$ 2′. The servo-mechanism was triggered by the last scaler of a neutron counting circuit, after a preset number of counts. The time taken at each point depended on the reactor power level

during the counting interval. Therefore $\int_0^t Ndt$ was recorded, where N was proportional to the neutron flux in the primary beam. This was done by recording for each point the total number of counts in a neutron counter located vertically above the spectrometer crystal. This monitor provided adequately for small fluctuations in reactor power. To ensure, moreover, that the measurements were made under the steadiest conditions, counts were allowed to accumulate only when the reactor was on automatic control.

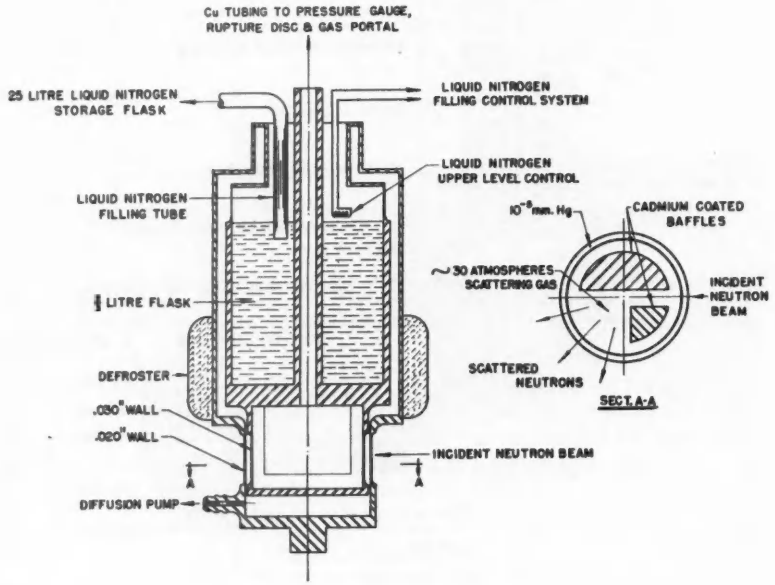

FIG. 3. *Scattering chamber.*

(b) Scattering Chamber

The scattering chamber shown in Fig. 3 was a double-walled steel Dewar flask with an upper compartment for the liquid nitrogen, and a lower cell for the deuterium gas. This gas cell was 2 in. in diameter and 2.5 in. high with a 0.030 ± 0.0005 in. thick polished steel wall. Internal cadmium-coated steel baffles served two purposes. Primarily they reduced double scattering, but also, since they were firmly screwed to the underside of the liquid nitrogen compartment, the baffles helped maintain the gas at a uniform temperature of 77.4°K. The Dewar was continuously evacuated with an oil diffusion pump to about 3.10^{-4} mm. of mercury pressure.

At small angles ($< 30°$) the neutron counter was exposed to part of the wall of the gas cell which was in the neutron beam, (Fig. 3, Section A–A). This, of

course, increased the background of slow neutrons. However, the effect was not as great as might be expected, for the steel wall was crystalline and most of its scattering, like that of a crystalline powder, was into Debye–Scherrer cones. No cone was inside an angle of 30°, and there was little diffuse scattering.

An Ashcroft Laboratory test gauge, 0–1000 p.s.i. range with 5 p.s.i. subdivisions, and evacuating and filling needle valves, were connected to the gas cell with a length of copper tubing. The pressure gauge was calibrated by the Design and Development Branch at Chalk River and found to be accurate. Liquid nitrogen was blown into the Dewar from a 25 liter flask at 15 min. intervals by means of an electrically actuated compressed air valve, the valve being opened by a time switch and shut off by a tungsten coil (Fig. 3) connected into a balanced bridge. As a precaution against failure of the liquid nitrogen system, which would produce a dangerously high gas pressure, there was in the system a rupture disk rated at 525 p.s.i. maximum. An external heater prevented dew formation on the outside of the Dewar at the gas level.

IV. Experimental Results

(*a*) *Angular Distributions*

The intensity of neutrons scattered from deuterium gas was measured at eight equally spaced angles: 11.2°, 19.2°. . . . 67.2°. One thousand counts were recorded at each point and the whole angular range was swept back and forth through 16 half cycles, the whole run lasting 64 hr.

Background runs, with the gas cell evacuated and at room temperature, were made before and after the gas scattering run. The first background run was five half cycles, the second three, with 100 counts at each point.

A separate measurement was made of the fast neutron background alone, by substituting a composite absorber of sheet cadmium, paraffin, and boron carbide for the gas cell. With 100 counts at each point, a run of three half cycles was made.

To calibrate the angular scale, a transit was mounted on the axis of rotation of the counter arm. The telescope was aligned on a distant point, and the counter arm and transit scales were correlated through an angle of 90°. Zero angle was determined by measuring the shape of the monokinetic beam, and finding the mid-point. A neutron absorber was used to reduce the intensity of the main beam. This was done both before and after the angular distribution measurements, and the two measurements agreed.

The measured angular distribution had a 12: 1 variation in counting rate. This large variation was due to the true deuterium pattern, the geometry of the gas cell and collimator slit system, and the background. The total background varied 30: 1; but the fast neutron component was constant. The counting rates are illustrated in Table IV for three angles: 11.2°, 35.2°, 67.2°. These rates are expressed as counts per minute for clarity, though in all the calcula-

tions counts per 10^4 monitor counts were used. The gas was at an average 21 atm. pressure and 77.4°K. The errors quoted are standard deviations.

TABLE IV

MEASURED NEUTRON INTENSITIES SCATTERED FROM DEUTERIUM GAS (21 ATM. AND 77.4°K.) AS A FUNCTION OF SCATTERING ANGLE

	Scattering angle		
	11.2°	35.2°	67.2°
Gas-scattered + Total background (c/m)	200.3 ± 1.6	54.2 ± 0.4	17.4 ± 0.1
Total background (c/m)	68.7 ± 2.6	4.7 ± 0.2	2.4 ± 0.1
Fast neutron background (c/m)	1.2 ± 0.1	1.2 ± 0.1	1.2 ± 0.1

(*b*) *Wave Length Measurement*

The neutron energy in the monokinetic beam from the crystal spectrometer was measured before and after the gas scattering experiments. For this the gas cell was replaced with a sodium chloride crystal, and rocking curves were made on both sides of the beam from the first crystal. The narrow rocking curve obtained when the planes of the two crystals are parallel is a measure of the imperfections of the crystals, while the broad curve obtained when the crystals are antiparallel is a measure of the energy spectrum of the diffracted neutron beam. The angle between the two peaks is four times the Bragg angle θ_B, and the neutron wave length is $\lambda = d \sin \theta_B$, where $d = 5.628$Å is the lattice spacing of the crystal.

The angle between the maxima of the diffracted peaks was 43.56°, corresponding to a neutron wave length of 1.063Å or an energy of 0.0724 ev. The width at half maximum of the broad diffraction peak was 1.15° and of the narrow peak 0.22°. Therefore, the spread in wave length of the diffracted neutron beam from the spectrometer was approximately $\pm$ 0.05Å.

(*c*) *Gas Purity*

Deuterium gas, drawn from the gas cell at the end of the angular distribution run, was analyzed for isotopic composition by the Chemical Control Laboratory at Chalk River, using a Nier-type 60° mass spectrometer. The average result of four samples taken was D_2 molecules 99.20%, HD molecules $0.80 \pm 0.06\%$.

(*d*) *Transmission Measurements*

Transmission measurements were made on the scattering gas and cell walls as a rough over-all check on these materials. For these measurements, the counter arm was set to 0°, and the beam was stopped down with a cadmium iris.

The scattering cross section per atom of deuterium gas at 21 atm. pressure and 77.4°K. for 0.0724 ev. neutrons was found to be 3.4 ± 0.4 barns. This is

in agreement with the accurate cross section for neutrons of a few volts energy: 3.44 ± 0.06 barns (6). The scattering cross section of iron for 0.0724 ev. neutrons was found to be 12.6 ± 0.5 barns, in agreement with the known value 12.7 barns.

V. Reduction of Experimental Results

Before the measured angular distribution can be compared with theory, attention must be given to background, gas pressure, effective scattering volume, double scattering, and hydrogen impurity. These complications are treated below in the order of their application.

(*a*) *Background*

Background arose from two sources: fast neutrons which penetrated the counter shield; and slow neutrons which had been scattered into the counter collimator by the steel walls of the gas cell. The fast neutron component was unaffected by the addition of gas to the cell. The slow neutron component was assumed to traverse the cell, and the measured value was multiplied by exp $(-ds)$, where d is the cell diameter and s is the fraction of beam scattered per unit length by the gas. This correction for gas transmission is appreciable at small scattering angles but is only 0.5% of the gas-scattered intensity for angles greater than 30°. After this adjustment the background was subtracted from the total intensity to give the gas-scattered intensity.

(*b*) *Gas Pressure*

A small leak in the system caused the gas pressure to drop steadily throughout the experiment, from 22.5 to 19.5 atm. Frequent readings of gas pressure were made and a smooth curve of pressure versus time has been drawn from which the exact gas pressure for each 1000 count interval was determined. The gas-scattered intensity for each interval was then corrected for any pressure deviation from an average 21 atm.

The 15 min. liquid nitrogen filling cycle caused a varying temperature gradient along the filling pipe and therefore a fluctuation in the gas pressure of about plus or minus 1%. Since the average error resulting from this ripple must be very much less than 1%, it has been neglected.

(*c*) *Scattering Volume*

The effective scattering volume of gas as a function of the scattering angle is

$$V = r\left[2r\left(\psi - \frac{\phi}{2}\right) + \frac{w\cos\left(\psi - \frac{\phi}{2}\right)}{\cos\frac{\phi}{2}}\right] \quad \text{for } 0 < \phi \leqslant 2\psi$$

$$= \frac{w^2}{\sin\phi} \quad \text{for } 2\psi \leqslant \phi \leqslant \frac{\pi}{2}$$

where $\psi = \sin^{-1}\frac{w}{2r}$. V is the volume of gas of unit height, r is the radius of

the gas cell, w is the collimator slit width, and ϕ is the scattering angle. The gas-scattered intensities were therefore divided by V to give the scattering per unit volume.

(*d*) *Double Scattering*

An approximate correction for double scattering in the gas, and between the gas and cell wall, was made. The correction was based on two very crude assumptions: that the gas scatters isotropically in the laboratory system, and the wall scatters not at all for scattering angles $< 30°$, isotropically for angles $> 30°$. The necessary integration was made numerically for the geometry of the experiment, i.e., 1/2 in. collimated beams, 2 in. I.D. gas cell, and internal nonreflecting baffles as shown in Fig. 3 (Section A–A). The result may be written:

$$I_D(\phi) = [aP(\phi) + bQ(\phi)]\, I_s,$$

where I_D is the intensity due to double scattering as a function of the scattering angle ϕ; I_s is the average intensity due to single scattering; a is the fraction of beam scattered by the gas, at the temperature and pressure of the experiment; b is the fraction of beam scattered by one wall; P and Q are functions of ϕ as given in Table V for the scattering angles 0°, 30°, 45°, 60°, and 90°.

TABLE V

DOUBLE SCATTERING TERMS

Scattering angle (ϕ)	$P(\phi)$	$Q(\phi)$
0°	0.177	0.229
30°	0.235	0.114
45°	0.269	0.108
60°	0.305	0.099
90°	0.280	0.073

$I_D(\phi)/I_s$ was found to be nearly independent of angle for the conditions of this experiment, varying between 3.1% and 3.4% over the angular range 11° to 67°. I_s corresponds approximately to the experimental intensity at 67.2°. This was determined by a numerical integration over 4π steradians of Spiers' differential cross section $\sigma_A + \frac{B}{A}\sigma_B$, $\frac{B}{A}$ being found by a successive approximation. Finally I_D was subtracted from the scattered intensity per unit volume, leaving an experimental intensity $I(\phi)$.

(*e*) *Hydrogen Impurity*

The scattering cross section of hydrogen is approximately six times that of deuterium, and since the deuterium gas of this experiment contained 0.4% hydrogen, a correction for this impurity was required.

At such a low concentration the hydrogen would be entirely in the form of HD molecules. Dr. N. K. Pope of this laboratory has kindly calculated the

differential cross section for the HD molecule and from his general formula has derived the semiclassical approximation, viz.

$$\sigma_J(\theta) = \frac{9}{64}\left(A_H^2 + A_D^2 + 0.75\,B_H^2 + 2B_D^2 + 2A_H A_D \frac{\sin x}{x}\right) \qquad (6)$$

where $x = \dfrac{4\pi r_e \sin\dfrac{\theta}{2}}{4\lambda/3}$,

$r_e = 0.747$Å,
θ = angle of scattering in center of mass system,
λ = neutron wave length in laboratory system = 1.063Å,
$A_H = 3a_1 + a_0 = -0.75 \times 10^{-12}$ cm.,
$B_H = 2(a_1 - a_0) = 5.81 \times 10^{-12}$ cm.,
$A_D = 2a_{3/2} + a_{1/2} = 1.346 \times 10^{-12}$ cm.
$B_D = a_{3/2} - a_{1/2} = \pm 0.567 \times 10^{-12}$ cm.

a_1 and a_0 are the scattering lengths for hydrogen and are given most accurately by the total scattering cross section σ_0, and the coherent scattering amplitude a_H(10, 12).

$\sigma_0 = 4\pi(3/4\,a_1^2 + 1/4\,a_0^2) = 20.36 \times 10^{-24}$ cm^2.
$a_H = 2(3/4\,a_1 + 1/4\,a_0) = -0.375 \times {}^{-12}$ cm.

$a_{3/2}$ and $a_{1/2}$ are the scattering lengths for deuterium given in this report (Section VI). They were applied in a successive approximation.

The measured intensities are the sum of the intensities scattered by the *HD* and D_2 molecules. If $I(\phi)$ is the experimental intensity as given in (*d*) above, and $I(D_2, \phi)$ the intensity due to deuterium molecules.

$$I(D_2, \phi) = I(\phi)\frac{1}{1 + Nq}$$

where $q = \sigma_{HD}(\phi)/\sigma_{D2}(\phi)$,

$N = \dfrac{0.008}{0.992}$, is the number of *HD* molecules per D_2 molecule, and $\sigma_{HD}(\phi)$, $\sigma_{D2}(\phi)$ are the cross sections for scattering in the laboratory through an angle ϕ by *HD* and D_2 respectively. The semiclassical formula was used not only for σ_{HD}, but also for σ_{D2}, since the ratio of the two would then minimize differences between the approximate and exact formulas. The *HD* cross section of Equation (6) is independent of J and we have only to transform $\sigma_J(\theta)$ from the center of mass to the laboratory to get $\sigma_{HD}(\phi)$. The deuterium cross section had to be summed as described for the vibration (Section II(*d*)) and then transformed to the laboratory system. The correction increases smoothly from 2.6% at 11° to 5.2% at 67°.

(*f*) *Outer Effect*

Owing to the high pressure of the gas, the scattering at small angles is less than that for free molecules. Debye (3, 14) calls this the "outer" effect and

attributes it to the unavailability of the space occupied by the molecules. For X-ray scattering by a gas of diatomic molecules which act like spheres of diameter D in collisions, but like pairs of particles separated by a distance r_e in scattering, Debye has shown that the intensity is proportional to

$$(1/2)\left(1+\frac{\sin x}{x}\right)-4\pi D^2N\left(\frac{\sin x/2}{\frac{x}{2}}\right)^2\frac{\sin u - u\cos u}{u^3}, \qquad (7)$$

where $x = \dfrac{4\pi r_e}{\lambda}\sin\dfrac{\theta}{2}$,

$u = Dx/r_e$,
N = number of molecules per unit volume,
λ = wave length,
θ = scattering angle.

This formula applies also to neutron scattering by deuterium if transitions involving parity change are unimportant and the semiclassical approximation is assumed. Both these conditions hold at small angles ($< 20°$).

The ratio of the second term to the first was computed, using $D = 2.72$Å (11, page 183). The computation was made for the center of mass system, and then transformed to the laboratory system. The ratio was then applied to the calculated intensity with the result shown in Fig. 6, to give much better agreement with the experiment. It should be noted, however, that neither of the points affected by the "outer" effect was used in the plot from which $a_{1/2}/a_{3/2}$ was found.

VI. Determination of Scattering Lengths

(a) *Ratio of $a_{1/2}$ to $a_{3/2}$*

The final corrected experimental intensities, modified also for molecular vibration (Section II(d)), are given in Table VI. In Fig. 4 these experimental intensities, divided by σ_B, are plotted against σ_A/σ_B (Section II(b)) for the angles 27.2, 35.2, 43.2, 51.2, 59.2, and 67.2 degrees. The ordinate scale is arbitrary and is therefore not numbered. Two abscissa scales are shown, σ_A/σ_B and the corresponding scattering angles. The most probable straight line has been drawn through the points, and cuts the x-axis at $-B/A = -0.173$. A standard deviation has been assigned and is shown by two further straight lines. B/A is then 0.173 with a standard deviation of $\pm$ 0.022 and a probable error of

TABLE VI

EXPERIMENTAL SCATTERED NEUTRON INTENSITIES
(with all corrections applied) as a function of scattering angle

Scattering angle	11.2°	19.2°	27.2°	35.2°	43.2°	51.2°	59.2°	67.2°
Intensities with standard deviations	586.3 ± 12.9	578.2 ± 9.2	479.2 ± 5.7	392.4 ± 3.9	316.0 ± 3.2	255.6 ± 2.6	215.4 ± 2.2	185.3 ± 1.9

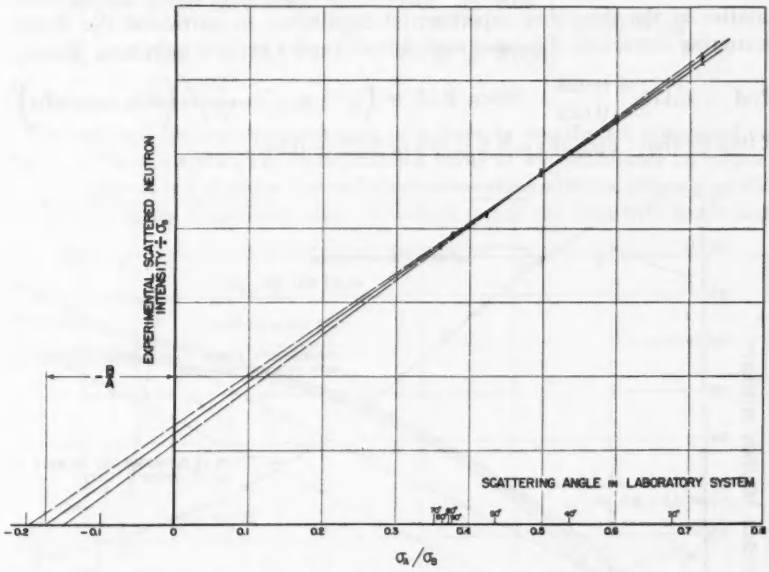

FIG. 4. *Plot of experimental intensities* $\div \sigma_B$ *versus* σ_A/σ_B.

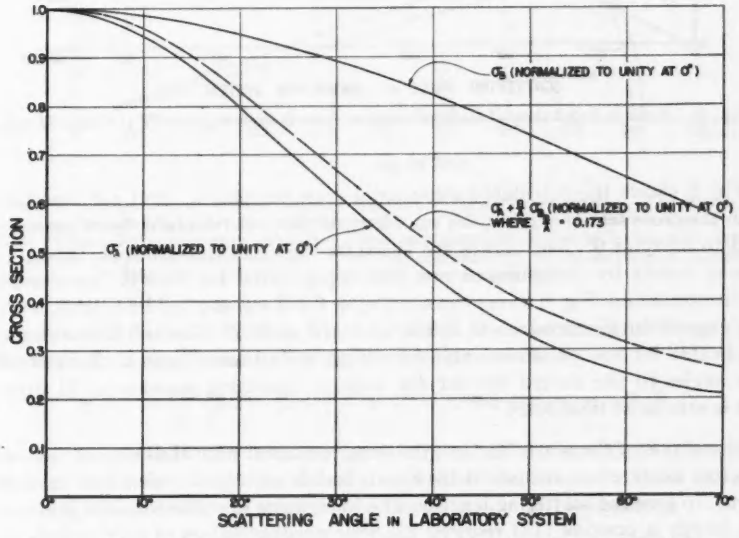

FIG. 5. *Theoretical differential cross sections corrected for thermal motion of molecules.*

$\pm$ 0.016. To the statistical error, $\pm$ 0.016, must be added errors due to uncertainties in the theory or experimental conditions; in particular the double scattering correction is inexact and the ortho-para ratio is unknown. Finally: $B/A = 0.173 \begin{matrix} +0.028 \\ -0.022 \end{matrix}$. Since $B/A = \left(1 - a_{1/2}/a_{3/2}\right)^2 \Big/ \left(2 + a_{1/2}/a_{3/2}\right)^2$, it follows that: $a_{1/2}/a_{3/2} = 3.2 \pm 0.3$ or 0.12 ± 0.04.

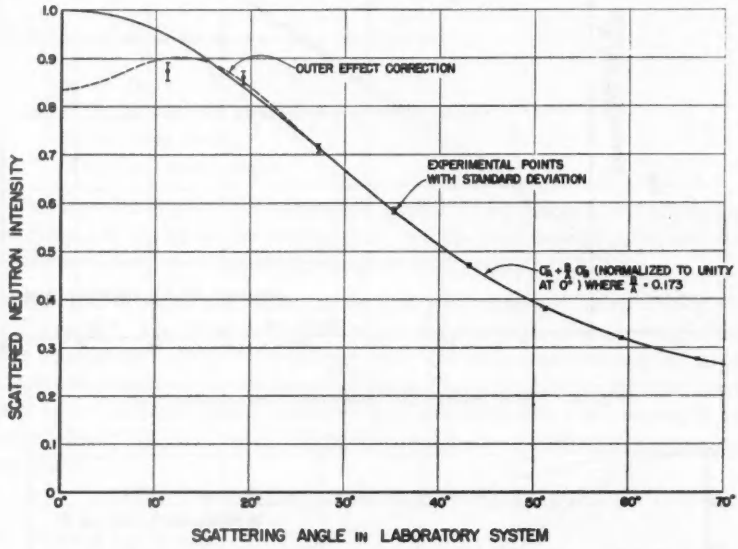

FIG. 6. *Angular distribution of scattered neutrons from deuterium gas at 77.4°K. and 21 atm. pressure.*

Fig. 5 shows the calculated differential cross sections σ_A and σ_B, together with the cross section $\sigma_A + 0.173\ \sigma_B$, where all three curves have been normalized to unity at 0°. The curves are based on the accurate values of Table II. Spiers' results for molecules at rest (but recalculated for 77.4°K) were used for interpolation. Fig. 6 shows the same $\sigma_A + 0.173\ \sigma_B$, as a full line curve, with the experimental intensities of Table VI fitted at 27.2°. The full line curve is applicable for low pressures only. According to formula (7), it is changed at low angles to the dotted line for the average operating pressure of 21 atm. but is otherwise unaffected.

The ratios of the scattering lengths were combined with the cross section of the free deuteron as measured by Fermi and Marshall (6), viz., 3.44 $\pm$ 0.06 barns, to give the scattering lengths. The knowledge that the coherent scattering length is positive (15) reduced the four possible values of each length to two values which are

$$\left.\begin{aligned} a_{1/2} &= 0.826 \pm 0.012 \\ a_{3/2} &= 0.26 \pm 0.02 \end{aligned}\right\} \quad \text{or} \quad \left.\begin{aligned} &0.07 \pm 0.03 \\ &0.638 \pm 0.006 \end{aligned}\right\} \times 10^{-12} \text{ cm.}$$

(*b*) *Previous Measurements*

The methods for the determination of scattering lengths are compared on Fig. 7. With $a_{1/2}$ and $a_{3/2}$ as co-ordinates a value of σ_T establishes an ellipse. A ratio $a_{1/2}/a_{3/2}$ is a straight line and the intersections with the ellipse give the scattering lengths. Experimental uncertainties spread the lines into bands and

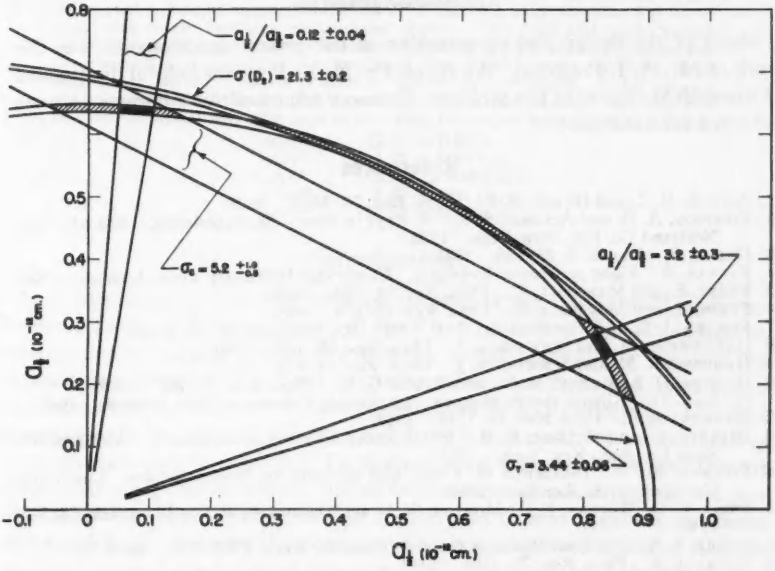

FIG. 7. *Comparison of methods for determination of the scattering lengths. The total cross section σ_T gives an ellipse and the scattering lengths are obtained from the intersections of this ellipse with another experimental quantity. Three such quantities are (i) $\sigma(D_2)$ the cross section of deuterium gas for low energy neutrons, Fermi and Marshall* (6), *(ii) σ_c the coherent scattering cross section, Wollan, et al.* (18), *(iii) $a_{\frac{1}{2}}$ $a_{\frac{1}{2}}$ from the present experiment.*

the intersections become areas. The analysis of the experiment of Fermi and Marshall (6) is equivalent to finding the intersection of

$$\sigma(D_2) = \frac{4\pi}{3}\left\{6.271\ (2a_{3/2}^2 + a_{1/2}^2) - 1.865\ (a_{3/2} - a_{1/2})^2\right\}$$

with σ_T. This is shown on the same figure. Crystal diffraction (15, 18) gives the coherent scattering length f_D (usually quoted in the form of a cross section $\sigma_c = 4\pi f_D^2$) from which the straight line $2a_{3/2} + a_{1/2} = 2f_D$ is obtained.

In principle the intersection of any two experimental lines on Fig. 7 yields a possible pair of scattering lengths, but the total cross section, being the

simplest to measure, is taken as fundamental. The shaded areas mark the regions of experimental values of $a_{3/2}$ and $a_{1/2}$ according to the three investigations, all referred to $\sigma_T = 3.44 \pm 0.06$. It will be seen that the values of $a_{3/2}$ and $a_{1/2}$ from gas scattering lie well outside the limits set by Fermi and Marshall. They lead to a coherent scattering cross section of 5.8 ± 0.2 barns, and so are consistent with those deduced from the Oak Ridge value of $5.2 \pm \frac{1.0}{0.5}$ barns; but they are more closely defined.

Acknowledgments

Much of the design and construction of the crystal spectrometer was the work of Mr. A. J. Pressesky. We thank Dr. N. K. Pope for helpful discussions of theoretical aspects of the problem. To many others of this laboratory we are indebted for assistance.

References

1. ALCOCK, N. Z. and HURST, D. G. Phys. Rev. 75: 1609. 1949.
2. COMPTON, A. H. and ALLISON, S. K. X-Rays in theory and experiment. 2nd ed. Van Nostrand Co. Inc., New York. 1935.
3. DEBYE, P. Physik. Z. 28: 135. 1937.
4. FARKAS, A. Light and heavy hydrogen. Cambridge University Press, London. 1935.
5. FERMI, E. and MARSHALL, L. Phys. Rev. 71: 666. 1947.
6. FERMI, E. and MARSHALL, L. Phys. Rev. 75: 578. 1949.
7. FOWLER, I. L. and TUNNICLIFFE, P. R. Rev. Sci. Instruments. In press.
8. HAMERMESH, M. and SCHWINGER, J. Phys. Rev. 69: 145. 1946.
9. HAMERMESH, M. and SCHWINGER, J. Phys. Rev. 71: 678. 1947.
10. HUGHES, D. J., BURGY, M. T., and RINGO, G. R. Phys. Rev. 77: 291. 1950.
11. JEANS, J. H. Kinetic theory of gases. Cambridge University Press, London. 1940.
12. MELKONIAN, E. Phys. Rev. 76: 1744. 1949.
13. PAULING, L. and WILSON, E. B. Introduction to quantum mechanics. McGraw-Hill Book Co., Inc., New York. 1935.
14. PIRENNE, M. H. Diffraction of X-rays and electrons by free molecules. Cambridge University Press, London. 1946.
15. SHULL, C. G., WOLLAN, E. O., MORTON, G. A., and DAVIDSON, W. L. Phys. Rev. 73: 842. 1948.
16. SPIERS, J. A. National Research Council (Canada), Rept. CRT-417. April, 1949.
17. SPIERS, J. A. Phys. Rev. 75: 1765. 1949.
18. WOLLAN, E. O., DAVIDSON, W. L., and SHULL, C. G. Phys. Rev. 75: 1348. 1949. The limits of error have been privately communicated.

THE PRECISION MEASUREMENT OF HALF LIVES OF RADIOACTIVE SUBSTANCES[1]

By Lorna M. Silver[2]

Abstract

A vibrating reed electrometer with feedback amplifier has been used in conjunction with a differential ionization chamber to measure accurately the decay periods of several radioactive isotopes. This method proved to be simple, reliable, and free from uncertain corrections, with a low background due to the differential technique adopted and a low drift rate (normally less than 5×10^{-17} amp.) due to the feedback electrometer circuit. This high and easily varied sensitivity enabled the decay to be followed over 12 periods, making possible the detection of, and correction for, any weak long lived impurity activity, thus eliminating one major source of error in half life measurements. Least squares analysis of the data showed that a quadratic mean error as small as 1/2% can be easily achieved with this apparatus. Half life values were found as follows:

$_{29}Cu^{64}$	12.88 ± 0.03 hr.
$_{29}Cu^{66}$	4.34 ± 0.03 min.
$_{28}Ni^{65}$	2.564 ± 0.005 hr.
$_{79}Au^{198}$	2.69 ± 0.01 days
$_{49}In^{116}$	53.93 ± 0.03 min.

Introduction

It is surprising to find that only 10 isotopes in the most recent Seaborg–Perlman Tables (12) have their half lives quoted to four significant figures, even though an accurate knowledge of decay periods is useful, for example, for radioactive standards, or in the monitoring of neutron fluxes and, more generally, for sorting out the various isotopes produced in an irradiation. This lack of precision in the present values of half lives is due partly to the methods of measurement usually employed. Techniques using Geiger–Müller counters are inadequate since the maximum and minimum rates of counting that are possible enable the decay to be followed for only six or seven periods and hence make it difficult to detect the presence of a weak long lived activity. Also the necessary corrections for dead time are a little uncertain, and the behavior of the counters is apt to vary during a run of several weeks. Peierls (10) has described the best method of taking counter data and subsequently evaluating the mean life of a substance, but it requires continuous recording and constant counter behavior during the run, so has not often been adopted. Ionization chambers with mechanical quartz fiber electrometers are more frequently used as they are more stable and no dead time correction arises. In their most usual form these are limited by the range of activities measurable and may suffer from mechanical zero drift, while highly sensitive instruments are difficult to set up. Vacuum tube electrometers for measuring ionization currents can be made quite sensitive and capable of covering a wide range but suffer from zero drift and for accuracy require continual calibration checking during a measure-

[1] *Manuscript received August 23, 1950.*
Contribution of the Chalk River Laboratories of the National Research Council of Canada. The experimental work was completed in August, 1948. Issued as N.R.C. No. 2283.
[2] *Now at the University of British Columbia, Vancouver, B.C.*

ment. Indeed, the early determinations of the period of Rn^{222} by Bothe (2) and by Curie (3) still represent two of the most accurate measurements ever made. The presence of a weak long lived activity is often the main source of error, and to detect and correct for this it is essential to use a technique that combines an extended range with a high sensitivity.

Experimental Method

The apparatus used in this work consisted of a differential ionization chamber and a vibrating reed condenser electrometer with feedback amplifier of the type described by Palevsky, Swank, and Grenchik (9). This electrometer is a very stable, wide range, sensitive instrument, its steady drift rate normally being less than 5.10^{-17} amp. A differential ionization chamber has the virtue that by careful balancing of the capacities of the two halves and thorough cleaning, the differential ionization current due to background activity can be practically neutralized. A scale diagram of the chamber is shown in Fig. 1. It is open to the air, thus necessitating a check on pressure, temperature, and humidity variations. The slots for the source holders enabled specimens to be replaced with exactly reproducible geometry, as was substantiated by the linearity of the results for a Zn^{65} monitor source. The electrometer head containing the vibrating reed and shorting switch was mounted on the heavy rigid steel case of the chamber. The experiment was carried out in an underground, air conditioned room where variations in temperature, humidity, and pressure were found to be insignificantly small when checked by following the decay of the relatively long lived Zn^{65} source.

Measurements of the ionization current were made by following the rise in potential of the chamber collection electrode with the vibrating reed electrometer by timing the pointer movement of a millivoltmeter having a 6 in. mirror scale, with a calibrated stop watch reading to 1/100 sec. Before using, the amplifier was carefully checked for linearity of response on the various ranges but the confirmatory test was the linearity of the results for a simply decaying isotope, In^{116}. It proved possible to follow the decay over 12 half lives, corresponding to a maximum range of 8000 mv. per min.—limited by timing accuracy—down to the background activity level of 0.8 mv. per min. Below 0.8 mv. per min., statistical errors due to fluctuations in ionization current become comparatively too large. The electrometer was operated continuously over the complete period of several weeks during which the measurements were taken in order to avoid errors due to drifts while warming up.

Sources were prepared by the irradiation of chemically pure samples in the Chalk River pile. In cases such as Cu^{64} and Cu^{66} the neutron flux and time of irradiation were adjusted to give the maximum ratio of desired to nuisance isotope abundances. The maximum initial activity corresponding to the 8000 mv. per min. deflection of the millivoltmeter was of the order of magnitude of 10 microcuries.

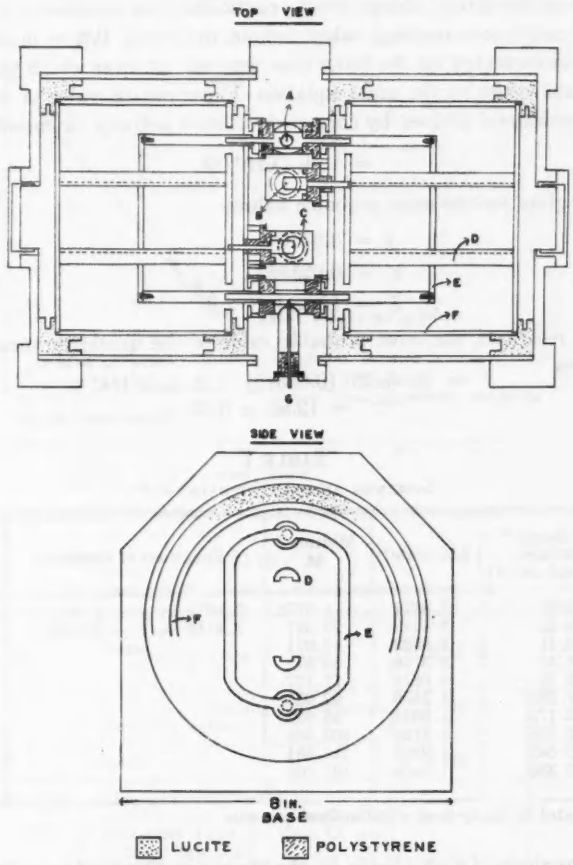

FIG. 1. *Differential ionization chamber. A—Connection to electrometer. B, C—H.T. connectors. D—Specimen holders. E—Ring collecting electrode. F—H.T. cylinder. G—Shorting key.*

Results

The decay periods were obtained by a least squares analysis of the data. Table I demonstrates this method of analysis in finding the most probable values of y and λ satisfying the decay equation:

$$\log(\lambda N) = y - \lambda' t,$$

where y = constant $\times \log(\lambda N_0)$

$$\lambda' = 0.43429\,\lambda$$

$$\lambda = \text{decay constant} = \frac{0.69315}{\text{half life}} = \frac{0.69315}{T}.$$

The value of the rate of charge at any particular time represents the average of several contiguous readings taken around that time. Where necessary this average was corrected for the finite time interval Δt, over which the batch of readings was taken by the usual equation: Experimental value of activity (at interval's midtime) divided by corrected value of activity (at interval's midtime)

$$= 1 + (\lambda \Delta t)^2/24.$$

The table gives for the most probable values

$$y = 3.9140$$
$$\lambda' = 0.023363$$
$$\therefore \quad T = 12.88 \text{ hr.}$$

From the residuals, the most probable value of the quadratic mean error in λ', $\epsilon_{\lambda'}$, gives

$$T = (0.43429)\,(0.69315)\,(1 \pm \epsilon_{\lambda'}/\lambda')/\lambda'$$
$$= 12.88 \pm 0.03 \text{ hr.}$$

TABLE I

SPECIMEN ANALYSIS OF DATA—Cu^{64}

Rate of charge,* millivolts/min. (Proportional to λN)	Log (rate)	Midtime, hr.	Equations of condition	Residuals
7712.88	3.8872	1.3178	$3.8872 = y - 1.3178\lambda'$	−.004009
2599.22	3.4148	21.597	$3.4148 = y - 21.597\lambda'$	−.005425
762.41	2.8822	44.071	etc.	+.002164
235.40	2.3718	65.911		+.002309
122.28	2.0874	77.757		+.009994
57.233	1.7576	92.021		+.006447
46.172	1.6644	95.922		+.008566
32.556	1.5124	102.936		−.003260
16.642	1.2212	115.661		−.009404
12.356	1.0919	121.109		−.007378

* = *Corrected for background of 0.8 millivolt per min.*

In the analysis of Cu^{64} (Table I), the change in sign of the residuals shows that the relationship between time and log (activity) is not linear, indicating the presence of a weak long lived activity—perhaps from some impurity in the copper sample. The residuals are much more sensitive to an impurity activity than any graphical plot of the relationship would be, as can be seen for example by comparing Fig. 2 and Table II, where the results for Ni^{65} are shown. In this case presumably Ni^{67} has been formed as well as Ni^{65}. The critical deviation of the final point was calculated from the statistical fluctuations of the readings at this near-background activity level, and the table shows how sensitive the precision is to the amount of long lived isotope assumed present. All points have been assigned equal weights in these analyses.

A list of the values obtained for the half lives of a few isotopes is given in Table III together with values obtained by other workers.

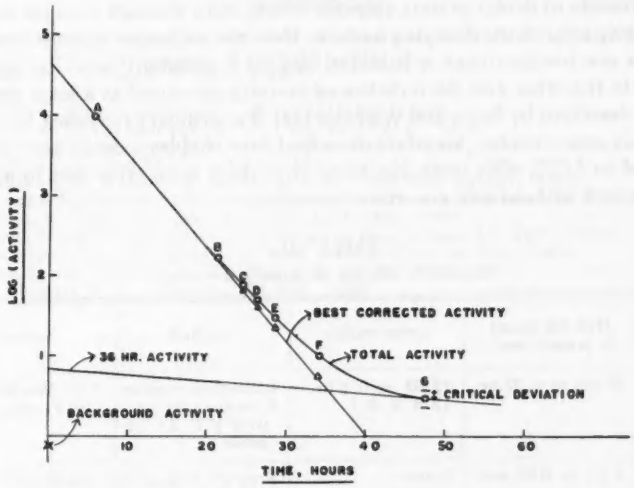

FIG. 2. *Correction for long lived activity in Ni^{65} sample.*

TABLE II

DETERMINATION OF BEST FITTING CURVE IN FIG. 2

Points used	Activity (rate of charge)	Half life	% Error
A, B, C, D, E, F	Total, i.e., neglecting the correction for 36 hr. activity	2.730 hr.	2.81
A, B, C, D, E	Total	2.628	0.73
A, B, C, D, E, F, G	Allowance made for 36 hr. activity assumed to correspond to measured value at time G, and activity taken as:		
	(1) Mean of experimental rates—critical deviation	2.614	0.83
	(2) Mean	2.564	0.192
	(3) Mean + critical deviation	2.500	1.38
Best value	*2.564 ± 0.005 hr.*		

Conclusions

The results indicate that it is possible to measure half lives quickly and easily to 1/2%. For the greatest precision after the singleness of the decay has been ascertained, one could use the double source differential chamber technique (3) in which, after establishing the small correction factors needed for pressure, temperature, and humidity, the precision is then limited only by the accuracy of the timing device and the strength of the available sources. The method could also be used to advantage for measurement of long periods and

in experiments to detect minute changes in half lives through changes in electron density around the decaying nucleus. Here the ionization current from the source in one compartment is balanced against a 'constant' activity (such as radium) in the other and the unbalanced activity measured at a later time, as recently described by Segre and Wiegand (13). For ordinary purposes, however, the simple experimental procedure described here enables a decay period to be measured to 1/2% with some assurance that there is no error due to a weak impurity and without any uncertain corrections.

TABLE III

PRECISION VALUES OF SOME HALF LIVES

Isotope	Half life found in present work	Other values	Method	Author
$_{29}Cu^{64}$	12.88 ± 0.03 hr.	12.62 ± 0.1 hr. 12.8 ± 0.1	Ionization chamber Pressure chamber with F.P. 54 amplifier	A. G. Ward* Van Voorhis (14)
$_{29}Cu^{66}$	4.34 ± 0.03 min.	5 min.	Pressure chamber and Perucca electrometer	Amaldi, others (1)
$_{28}Ni^{65}$	2.564 ± 0.005 hr.	2.6 ± 0.03 hr.		Livingood and Seaborg (7)
$_{79}Au^{198}$	2.69 ± 0.01 days	2.72 ± 0.05 days 2.73 ± 0.02 2.7 2.69	Ionization chamber Geiger–Müller counters Electroscope	A. G. Ward* Diemer and Groendijk (4) McMillan, Kamen, Ruben (8) D. Saxon (12)
$_{49}In^{116}$	53.93 ± 0.13 min.	54 min. 54 54.31 54.05 ± 0.16 54.4 ± 0.2 54.5 ± 0.3 54.02 ± 0.03	 Geiger–Müller counters, method independent of counting losses Ionization chamber Geiger counters uncorrected for small losses 	Amaldi, others (1) Lawson, Cork (6) Russel and Wattenberg (11) Graves and Walker (5) A. G. Ward* B. W. Sargent** Bobin and Lockett

* *Personal communication from Mr. A. G. Ward, Atomic Energy Research Establishment, Harwell, England.*

** *Personal communication from Dr. B. W. Sargent, Chalk River Labs., NRC, Canada.*

Acknowledgments

The author wishes to thank Mr. A. G. Ward, who designed the ionization chamber, for suggesting its present application and for his encouragement and interest in the measurements.

References

1. AMALDI, E., D'AGOSTINO, O., FERMI, E., PONTECORVO, B., ROSETTI, F., and SEGRE, E. Proc. Roy. Soc. (London), A, 149: 522. 1935.
2. BOTHE, W. Z. Physik, 16: 266. 1923.
3. CURIE, J. and CHAMIE, C. J. phys. radium, 5: 238. 1924.
4. DIEMER, C. and GROENDIJK, H. Physica, 11: 396. 1946.
5. GRAVES, A. C. and WALKER, R. L. Phys. Rev. 71: 1. 1947.
6. LAWSON, J. L. and CORK, J. M. Phys. Rev. 52: 531. 1937.
7. LIVINGOOD, J. J. and SEABORG, G. T. Phys. Rev. 53: 765. 1938.
8. MCMILLAN, E., KAMEN, M., and RUBEN, S. Phys. Rev. 52: 531. 1937.
9. PALEVSKY, H., SWANK, R. K., and GRENCHIK, R. Rev. Sci. Instruments, 18: 298. 1947.
10. PEIERLS, R. Proc. Roy. Soc. (London), A, 149: 467. 1935.
11. RUSSEL, B. and WATTENBERG, A. Plutonium Project Rept. CP-3305, October 1945.
12. SEABORG, G. T. and PERLMAN, I. Rev. Modern Phys. 20: 585. 1948.
13. SEGRE, E. and WIEGAND, C. E. Phys. Rev. 75: 39. 1949.
14. VAN VOORHIS, S. N. Phys. Rev. 50: 895. 1936.

NOTE ON THE RELATION BETWEEN FEYNMAN'S FORMULATION OF SCATTERING PROBLEMS AND THE BORN APPROXIMATION[1]

By J. R. H. Dempster

Abstract

Feynman's formulation of scattering problems is described briefly, and is compared with Born's approximation. The two procedures are shown to be equivalent and to be valid under the same conditions. Feynman's formulas are used to calculate the first and second order terms of the scattered particle wave function, with an arbitrary scattering potential.

Introduction

This paper deals with two methods of treating scattering problems in quantum mechanics which differ widely in approach. One, the well known Born approximation, is a perturbation theory solution of the Schrödinger equation. The other, described in recent papers by R. P. Feynman (1, 2), deals directly with the solutions of the wave equation, rather than with the equation itself.

In view of the fact that Feynman's approach leads to a simplified formulation of quantum electrodynamical problems, it seems desirable to establish a link between this procedure and the familiar Born approximation. The present paper accordingly carries out explicitly Feynman's treatment of a simple scattering problem and demonstrates the equivalence of the two methods.

The Born Approximation

Suppose that a particle of mass m and initial momentum $\hbar\vec{k}$* is scattered by a potential field $V(\vec{r})$. To apply the Born approximation, we set $\psi(\vec{r}, t) = u(\vec{r})e^{-i\omega t}$, with $\omega = \hbar k^2/2m$, and proceed to solve the time-independent Schrödinger equation

$$\{\nabla^2 + k^2 - (2m/\hbar^2)\ V(\vec{r})\}\ u(\vec{r}) = 0.$$

The method is well known, and we include here only those equations which will be compared directly with the Feynman solution. The wave function for the incident particle is $u_0 = e^{i\vec{k}\cdot\vec{r}}$. Green's solution of the first order equation is

$$u_1(\vec{r}_2) = (2m/\hbar^2) \int G(\vec{r}_2, \vec{r}_1)\ V(\vec{r}_1)u_0(\vec{r}_1)d\vec{r}_1\,, \tag{1}$$

where the Green's function $G(\vec{r}_2, \vec{r}_1) = -(4\pi\,|\,\vec{r}_2 - \vec{r}_1\,|)^{-1}\, e^{ik|\vec{r}_2 - \vec{r}_1|}$ satisfies the equation

$$\{\nabla_2^2 + k^2\}\ G(\vec{r}_2, \vec{r}_1) = \delta(\vec{r}_2 - \vec{r}_1). \tag{2}$$

[1] *Manuscript received August 8, 1950.*
Contribution from the Department of Physics, University of British Columbia, Vancouver, B.C. This paper is to be submitted in partial fulfillment of the requirements for an M.A. degree. The research was carried out with the aid of a Scholarship from the National Research Council of Canada.

* *The symbol $\hbar$ represents Planck's constant divided by 2π ($\hbar = 1.054 \times 10^{-27}$ erg. sec.).*

We write $d\vec{\tau} = dxdydz$; unless otherwise specified, the integration is to be taken over all space. The subscript 2 on ∇^2 means that it operates on the variables $\vec{r}_2$, and $\delta(\vec{r}_2 - \vec{r}_1) = \delta(x_2 - x_1)\,\delta(y_2 - y_1)\,\delta(z_2 - z_1)$.

For solutions at large r_2 we make the approximations

$$|\vec{r}_2 - \vec{r}_1| = r_2 - \vec{r}_1 \cdot \vec{r}_2/r_2 \approx r_2 \tag{3}$$

in the exponent and denominator respectively of the Green's function. The first and second order solutions are then:

$$u_1(\vec{r}_2) = -\frac{m}{2\pi\hbar^2}\frac{e^{ikr_2}}{r_2}\int V(\vec{r}_1)e^{i(\vec{k}-\vec{k}_2)\cdot\vec{r}_1}d\vec{r}_1 \tag{4}$$

$$u_2(\vec{r}_2) = \left(\frac{m}{2\pi\hbar^2}\right)^2\frac{e^{ikr_2}}{r_2}\int V(\vec{r}_2)e^{-i\vec{k}_2\cdot\vec{r}_2}\frac{e^{ikr_2}}{r_2}\int V(\vec{r}_1)e^{i(\vec{k}-\vec{k}_2)\cdot\vec{r}_1}d\vec{r}_1\,d\vec{r}_2 \tag{5}$$

where $\vec{k}_2 = k\vec{r}_2/r_2$, $\vec{k}_2 = k\vec{r}_2/r_2$.

Feynman's Formulation

Feynman's method is based on the probability amplitude for a particle to move from one space-time point to another. This function, called the kernel, is a sum of contributions $e^{iS/\hbar}$ from each possible path, where S is the classical action along the path. Denoting the point $\vec{r}_1$, t_1 by 1 and $\vec{r}_2$, t_2 by 2, $K(2, 1)$ is the amplitude for a particle known to be at $\vec{r}_1$, at the time t_1 to arrive at $\vec{r}_2$ at the time t_2. The wave function $\psi(2)$, representing the amplitude for the particle to be found at $\vec{r}_2$, t_2, is then given by the expression

$$\psi(2) = \int K(2, 1)\,\psi(1)\,d\vec{r}_1\,. \tag{6}$$

Feynman shows that the kernel is that solution of

$$\{i\hbar\partial/\partial t_2 - H_2\}\,K(2, 1) = i\hbar\delta(2, 1) \tag{7}$$

which vanishes for $t_2 < t_1$, where H is the Hamiltonian operator for the particle (the subscript 2 indicating that it acts on the variables 2), and $\delta(2, 1) = \delta(\vec{r}_2 - \vec{r}_1)\,\delta(t_2 - t_1)$. The kernel for a free particle is shown to be (for $t_2 > t_1$)

$$K_0(2, 1) = \left[\frac{m}{2\pi i\hbar(t_2 - t_1)}\right]^{\frac{3}{2}}\exp\left[\frac{im}{2\hbar}\frac{|\vec{r}_2 - \vec{r}_1|^2}{(t_2 - t_1)}\right]. \tag{8}$$

For a perturbation theory treatment of a particle in a potential $V(\vec{r})$, Feynman shows that the kernel may be expanded in increasing powers of V:

$$K(2, 1) = K_0(2, 1) + K_1(2, 1) + K_2(2, 1) + \ldots, \tag{9}$$

where
$$K_1(2, 1) = -(i/\hbar)\int K_0(2, 3)\,V(3)\,K_0(3, 1)\,d\tau_3 \tag{10a}$$

$$K_2(2, 1) = (-i/\hbar)^2\iint K_0(2, 3)\,V(3)\,K_0(3, 4)\,V(4)\,K_0(4, 1)\,d\tau_3\,d\tau_4 \tag{10b}$$

etc., using $d\tau = d\vec{r}dt$. The time integration is limited to the interval $t_2 > t_3 > t_1$ in (10a), $t_2 > t_3 > t_4 > t_1$ in (10b), by the condition $K(2, 1) = 0$ for $t_2 < t_1$.

The decisive advantage of Feynman's theory is the interpretation of the above formulas in terms of successive scattering. In (10*a*) for example we view the particle as moving freely from 1 to 3 (amplitude $K_0(3, 1)$), being scattered by the potential at 3 (amplitude $-(i/h)\ V(3)\ d\tau_3$), and moving as a free particle again to 2 ($K_0(2, 3)$). This is summed over all points 3, thus giving the term $K_1(2, 1)$. The successive terms of (9) are regarded as amplitudes for the particle to be scattered 0, 1, 2, etc., times by the potential V.

Corresponding to the expansion (9) of the kernel, the perturbed wave function may be written

$$\psi\ (2) = \psi_0(2) + \psi_1(2) + \psi_2(2) + \ldots, \tag{11}$$

where $\psi_0(1)$ is the wave function of the incident free particle, and

$$\psi_0(2) = \int K_0(2, 1)\ \psi_0(1)\ d\vec{\tau}_1, \tag{12a}$$

$$\psi_1(2) = -(i/h) \int K_0(2, 1)\ V(1)\ \psi_0(1)\ d\tau_1, \tag{12b}$$

etc.

Comparison of the Methods

From the foregoing discussion it is possible to show a close correspondence between the two methods. The similarity of Equations (12*b*) and (1) suggests identifying

$$G(\vec{r}_2, \vec{r}_1)e^{-i\omega t_2} = -(ih/2m) \int K_0(2, 1)e^{-i\omega t_1}\ dt_1\ . \tag{13}$$

Operating on (13) with $\{ih\partial/\partial t_2 + (h^2/2m)\ \nabla_2^2\}$ gives on the left, by (2),

$$(h^2/2m)\ \{\nabla_2^2 + k^2\}\ G(\vec{r}_2, \vec{r}_1)e^{-i\omega t_2} = (h^2/2m)\ \delta(\vec{r}_2 - \vec{r}_1)e^{-i\omega t_2},$$

and on the right, using (7) with $H = -(h^2/2m)\nabla_2^2$,

$$-(ih/2m) \int ih\ \delta(2, 1)e^{-i\omega t_1}\ dt_1 = (h^2/2m)\ \delta(\vec{r}_2 - \vec{r}_1)e^{-i\omega t_2}.$$

The equivalence of these two expressions does not prove Equation (13), since an arbitrary solution of the Schrödinger equation can still be added to one side. It does show however that there is an exact parallel between the two methods in spite of the wide difference in approach. Without giving a full proof of Equation (13), we will study the correspondence of the two methods from another point of view.

The n^{th} order perturbed solution is obtained by using for the kernel the first $n + 1$ terms of the series (9). We now seek to modify the Hamiltonian of the particle by introducing a potential function $V_n(\vec{r})$ such that $K_0(2, 1) + \ldots + K_n(2, 1)$ is the exact kernel for a particle moving in the potential $V_n(\vec{r})$. Applying Equation (7) gives

$$\{ih\partial/\partial t_2 + (h^2/2m)\ \nabla_2^2 - V_n(2)\}\ \{K_0(2, 1) + \ldots + K_n(2, 1)\} = ih\delta(2, 1), \tag{14}$$

which defines the function $V_n(\vec{r})$.

A general expression for the n^{th} order kernel is

$$K_n(2, 1) = -(i/h) \int K_0(2, 3)\ V(3)\ K_{n-1}(3, 1)\ d\tau_3.$$

Using the free particle form of Equation (7) gives therefore

$$\{ih\partial/\partial t_2 + (h^2/2m)\nabla_2^2\}\, K_n(2,1) = V(2)\, K_{n-1}(2,1).$$

Thus we see that $V_n(2)$ is given by the equation

$$V_n(2)\,\{K_0(2,1) + \ldots + K_n(2,1)\} = V(2)\,\{K_0(2,1) + \ldots + K_{n-1}(2,1)\}.$$

Multiplying this equation by $\psi_0(1)$ and integrating over $d\vec{r}_1$, we obtain

$$V_n(2)\,\{\psi_0(2) + \ldots + \psi_n(2)\} = V(2)\,\{\psi_0(2) + \ldots + \psi_{n-1}(2)\}. \qquad (15)$$

From the definition of V_n, the wave function $\psi_0 + \ldots + \psi_n$ must satisfy the modified Schrödinger equation containing this potential:

$$\{ih\partial/\partial t + (h^2/2m)\,\nabla^2 - V_n\}\,\{\psi_0 + \ldots + \psi_n\} = 0.$$

Using the expression (15) for V_n, this becomes

$$\{ih\partial/\partial t + (h^2/2m)\,\nabla^2\}\,\{\psi_0 + \ldots + \psi_n\} = V\{\psi_0 + \ldots + \psi_{n-1}\},$$

and subtracting the corresponding equation with n lowered by one gives

$$\{ih\partial/\partial t + (h^2/2m)\,\nabla^2\}\,\psi_n = V\,\psi_{n-1}. \qquad (16)$$

This is exactly the n^{th} order equation of the Born approximation. We have thus proved that the Born and Feynman solutions are identical, provided that the same incident particle wave function ψ_0 is chosen.

The condition for validity of either approximation is that the terms of the series expansion of the wave function (11) should decrease rapidly, i.e., that $|\psi_1| \ll |\psi_0| = 1$. Since the two methods give the same result for ψ_1, it is clear that they are valid under the same conditions.

Explicit Solution by Feynman's Method

To illustrate the equivalence of the two methods, we will use Feynman's formulas to calculate explicity the first and second order terms of the wave function. We set $\psi_0(1) = e^{i(\vec{k}\cdot\vec{r}_1 - \omega t_1)}$ for the wave function of the incident particle. The zero-order wave function (12*a*) should of course be the same. This is easily verified by direct integration using the expression (8) for the kernel.

The first order term, from (12*b*), is:

$$\psi_1(2) = -\frac{i}{h}\int\int_{-\infty}^{t_2}\left[\frac{m}{2\pi ih(t_2-t_1)}\right]^{\frac{3}{2}}\exp\left[\frac{im}{2h}\frac{|\vec{r}_2-\vec{r}_1|^2}{(t_2-t_1)}\right]V(\vec{r}_1)e^{i(\vec{k}\cdot\vec{r}_1-\omega t_1)}d\vec{r}_1\,dt_1$$

$$= -(i/h)e^{-i\omega t_2}\int T(|\vec{r}_2-\vec{r}_1|)\,V(\vec{r}_1)e^{i\vec{k}\cdot\vec{r}_1}d\vec{r}_1$$

where $$T(r) = \int_0^\infty (2\pi iht/m)^{-\frac{3}{2}}e^{imr^2/2ht}e^{i\omega t}dt$$

(using $r = |\vec{r}_2 - \vec{r}_1|$, $t = t_2 - t_1$) is the integral on the right of Equation (13), multiplied by $e^{i\omega t_2}$.

Now according to Feynman's interpretation of the perturbation formulas, $\psi_1(2)$ is due to particles scattered once at 1 and then proceeding as free particles to 2. Since a free particle has a definite velocity hk/m, we should expect a contribution to $T(r)$ only from the neighborhood of the point $t = (m/hk)r$. We rearrange the exponent, and make the substitution $t = (m/hk)\, r\,(1 + \xi)$:

$$T(r) = \left(\frac{m}{2\pi ih}\right)^{\frac{1}{2}} \int_0^\infty t^{-\frac{3}{2}} \exp\left[\tfrac{1}{2}ikr\,\frac{m}{hk}\,\frac{r}{t} + \tfrac{1}{2}ikr\,\frac{hk}{m}\,\frac{t}{r}\right] dt$$

$$= \left(\frac{m}{2\pi ih}\right)^{\frac{1}{2}} \left(\frac{mr}{hk}\right)^{-\frac{1}{2}} \int_{-1}^\infty (1+\xi)^{-\frac{3}{2}} \exp\left[\tfrac{1}{2}ikr\left(\frac{1}{1+\xi} + 1 + \xi\right)\right] d\xi$$

$$= \frac{m}{2\pi ih}\left(\frac{kr}{2\pi i}\right)^{\frac{1}{2}} \frac{e^{ikr}}{r} \int_{-1}^\infty (1+\xi)^{-\frac{3}{2}} e^{\frac{1}{2}ikr\xi^2/(1+\xi)} d\xi.$$

The coefficient of $i\xi$ in the exponent is $\frac{1}{2}kr\xi/(1 + \xi)$. For fairly energetic particles at large distances r_2, $kr \gg 1$. Hence except for the region $\xi \ll 1$ the exponential is a very rapidly oscillating function of ξ. The function $(1 + \xi)^{-\frac{3}{2}}$ varies slowly (except at $\xi \to -1$, and here the exponential oscillates with infinite frequency), and hence the integral vanishes except for very small values of ξ. Thus the physical reasoning of the previous paragraph is confirmed. For small ξ, we take $1 + \xi \approx 1$, and then, since $kr \gg 1$, extend the lower limit to $-\infty$. The integral becomes*

$$T(r) = \frac{m}{2\pi ih}\left(\frac{kr}{2\pi i}\right)^{\frac{1}{2}} \frac{e^{ikr}}{r} \int_{-\infty}^\infty e^{-(kr/2i)\xi^2} d\xi$$

$$= (m/2\pi ih) e^{ikr}/r.$$

Comparing this with the Green's function, we see that Equation (13) is verified.

Applying the asymptotic approximations (3), the first order wave function becomes

$$\psi_1(2) = -\frac{m}{2\pi h^2} \frac{e^{i(kr_2 - \omega t_2)}}{r_2} \int V(\vec{r}_1) e^{i(\vec{k} - \vec{k}_2)\cdot\vec{r}_1} d\vec{r}_1, \tag{17}$$

which agrees exactly with the Born approximation result (4).

From (10*b*), the second order wave function is:

$$\psi_2(2) = (-i/h)^2 \iint K_0(2, 3)\; V(3)\; K_0(3, 1)\; V(1)\; \psi_0(1) d\tau_3\, d\tau_1$$

$$= (-i/h)^2\, e^{-i\omega t_2} \iint T(|\vec{r}_2 - \vec{r}_3|)\; V(\vec{r}_3)\; T(|\vec{r}_3 - \vec{r}_1|)\; V(\vec{r}_1)\; e^{i\vec{k}\cdot\vec{r}_1} d\vec{r}_3 d\vec{r}_1$$

$$= \left(\frac{m}{2\pi h^2}\right)^2 \frac{e^{i(kr_2 - \omega t_2)}}{r_2} \int V(\vec{r}_3) e^{-i\vec{k}_2\cdot\vec{r}_3} \frac{e^{ikr_3}}{r_3} \int V(\vec{r}_1)\, e^{i(\vec{k} - \vec{k}_2)\cdot\vec{r}_1} d\vec{r}_1\, d\vec{r}_3 \tag{18}$$

using again the approximations (3). This is identical with the Born result (5).

* *In spite of the approximations used, this result is exact. With* $x = 1 + \xi$, $p = -ia = -\frac{1}{2}ikr$, *the integral is* $\int_0^\infty x^{-3/2} e^{-px + ia/x}\, dx$. *This can be evaluated by using a table of Laplace Transforms, such as* (*3*). *The method used has the advantage of affording a physical interpretation.*

It will be noted that the successive integrations involved in the higher order approximation do not lead to a more complicated time integral (as might be expected), but rather to simple products of the same function $T(r)$. This is due to the separation of the time dependence of Equation (13) in the factor $e^{-i\omega t_2}$. It is clear, in fact, that this time integral of the kernel will always give the same function provided only that the wave function can be separated in this way. Thus this integration, the most difficult step in the Feynman calculation, need not be repeated in every problem.

Acknowledgments

The author wishes to thank Dr. F. A. Kaempffer for suggesting the topic of this paper and for helpful discussion, and also the National Research Council of Canada for the award of a Bursary under which the research was carried out.

References

1. FEYNMAN, R. P. Rev. Modern Phys. 20: 367. 1948.
2. FEYNMAN, R. P. Phys. Rev. 76: 749. 1949.
3. MAGNUS, W. and OBERHETTINGER, F. Special functions of mathematical physics, Chelsea Publishing Company, New York. 1949. p. 127.

UPPER AND LOWER BOUNDS FOR THE ASYMPTOTIC NEUTRON DENSITY IN MILNE'S PROBLEM FOR THE SPHERE[1]

By W. Seidel[2] and R. E. Marshak[2]

Abstract

Rigorous upper and lower bounds for the asymptotic neutron density in Milne's problem for the sphere are calculated by means of an extension of Hopf's method for the plane.

We consider the following problem: a black sphere of radius a, i.e., a sphere which absorbs completely all neutrons which fall upon it, is surrounded by an infinite noncapturing medium which scatters neutrons isotropically without changing their velocity. No sources are present in the outer medium except that a current density of amount $\frac{F}{4\pi r^2}$ (F is a constant) is assumed to exist in the direction $-r$. We wish to determine upper and lower bounds for the asymptotic neutron distribution in the (outer) medium.

An exact determination of the neutron density for the present problem—by transform methods or otherwise—seems out of the question (Berlin (1) and Hansson (2)). Fortunately, for some problems of practical interest it is sufficient to know the asymptotic behavior of the neutron density. In a previous paper (Marshak (4)), * one of the authors solved the transport equation approximately by expanding the angular distribution in a finite number of spherical harmonics; this method has the advantage that it yields an approximate expression for the neutron density over the entire range. The disadvantage of the spherical harmonic method lies in the difficulty of estimating the error of any particular approximation. To check this point for the sphere, we derived the equivalent integral equation and from it — using methods first developed by Hopf (3)—we now derive rigorous upper and lower bounds for the asymptotic neutron density. A comparison of the results with the results of the spherical harmonic method enables one to judge the accuracy of the successive approximations in the harmonic method. A further value in reporting the present calculations lies in the possible extension of this method to other problems.

As shown in I, the asymptotic solution for $[r\psi_0(r)]$ is of the form $B(r - r_0)$, where r_0 is a function of a and for large a should go over into $(a - 0.7104)$. We start with the integral equation† for $[r\psi_0(r)]$, which is equivalent to the tran-

[1] *Manuscript received November 7, 1949.*
The contents of this paper were contained in a Montreal Report (MT-49) dated April 15, 1944.

[2] *University of Rochester, N.Y., U.S.A.*

* *This paper will be referred to as I and the same notation will be used.*

† *The derivation of this integral equation is straightforward and is given in our original report MT-49; cf. also references in (1).*

sport equation plus boundary condition $\psi(a, \mu)=0$ for $\mu>0$, and from this integral equation we obtain rigorous upper and lower bounds for r_0.

The integral equation in question* is:

$$r\psi_0(r) = \frac{1}{2}\int_a^\infty r'\psi_0(r')\left\{E(|r-r'|) - E\left(\sqrt{r^2-a^2}+\sqrt{r'^2-a^2}\right)\right\}dr'. \quad (1)$$

To derive upper and lower bounds for the asymptotic neutron density, we write: $r\psi_0(r) = r + q(r)$, where $q(r)$ satisfies the integral equation:

$$q(r) = \frac{1}{2}\int_a^\infty q(t)\left\{E(|r-t|) - E\left(\sqrt{r^2-a^2}+\sqrt{t^2-a^2}\right)\right\}dt + \frac{\bar{E}_3(r)}{2}, \quad (2)$$

with $$\bar{E}_3(r) = -\left\{aE_2(r-a) - E_3(r-a) + E_3\left(\sqrt{r^2-a^2}\right)\right\}. \quad (2a)$$

Making use of the properties of the E_n-functions, it can be shown that $\bar{E}_3(r)$ is negative for all $r > a$ (cf. Appendix). Further we remark that $q(r)$ satisfies the inequality $-a < q(r) \leqslant 0$(cf. Appendix) and must be a monotonically† increasing function of r. We now integrate Equation (2) with respect to r from $\tau \geqslant a$ to $M > \tau$. We get:

$$\int_\tau^M q(r)dr = \frac{1}{2}\int_\tau^M dr\int_a^\infty q(t)E(|r-t|)\,dt - \frac{1}{2}\int_\tau^M dr\int_a^\infty q(t)E\left(\sqrt{r^2-a^2} + \sqrt{t^2-a^2}\right)dt + \frac{1}{2}\int_\tau^M \bar{E}_3(r)dr.$$

In the second and third integrals the order of the integration may be reversed since the integrals with respect to t converge uniformly for r in $\tau \leqslant r \leqslant M$. Thus we find:

$$\begin{aligned}\int_\tau^M q(r)dr = {} & \frac{1}{2}\int_a^\tau q(t)dt\int_\tau^M E(r-t)dr + \frac{1}{2}\int_\tau^M q(t)dt\int_t^M E(r-t)dr \\ & + \frac{1}{2}\int_\tau^M q(t)dt\int_\tau^t E(t-r)dr + \frac{1}{2}\int_M^\infty q(t)dt\int_\tau^M E(t-r)dr \\ & - \frac{1}{2}\int_a^\infty q(t)dt\int_\tau^M E\left(\sqrt{r^2-a^2}+\sqrt{t^2-a^2}\right)dr + \frac{1}{2}\int_\tau^M \bar{E}_3(r)dr.\end{aligned}$$

With the help of relations between E_n-functions, we obtain:

* *The function $E_n(x) = \int_1^\infty e^{-xu}u^{-n}\,du$ for $x > 0$; the E_1-function is usually written without a subscript. For the elementary properties of the functions $E_n(x)$ the reader is referred to E. Hopf, loc. cit. pp. 26-27.*

† *This result follows from physical considerations and can be seen very roughly as follows: if the black core had a smaller radius, the asymptotic solution for $\psi_0(r)$, namely $\left(1-\frac{r_0}{r}\right)$, would be valid further inward than it is actually valid. Since this is not the case, the density must drop more rapidly than is given by r_0 because neutrons which further outward are scattered back are now—in the neighborhood of the core—lost owing to the absorption by the black core; this effect becomes more and more important (monotonicity!) as the core is approached. We have not succeeded in obtaining an analytic proof of the monotonicity.*

$$\int_\tau^M q(\tau)d\tau = \frac{1}{2}\int_a^\tau q(t)\{E_2(\tau - t) - E_2(M - t)\}dt + \frac{1}{2}\int_\tau^M q(t)\{1 - E_2(M - t)\}dt$$

$$+ \frac{1}{2}\int_\tau^M q(t)\{1 - E_2(t - \tau)\}dt + \frac{1}{2}\int_M^\infty q(t)\{E_2(t - M) - E_2(t - \tau)\}dt$$

$$- \frac{1}{2}\int_a^\infty q(t)dt\int_\tau^M E\left(\sqrt{\tau^2 - a^2} + \sqrt{t^2 - a^2}\right)d\tau + \frac{1}{2}\int_\tau^M \bar{E}_3(\tau)d\tau.$$

Hence,

$$0 = \int_a^\tau q(t)\{E_2(\tau - t) - E_2(M - t)\}\,dt - \int_\tau^M q(t)E_2(M - t)dt$$

$$- \int_\tau^M q(t)E_2(t - \tau)dt + \int_M^\infty q(t)\{E_2(t - M) - E_2(t - \tau)\}\,dt$$

$$- \int_a^\infty q(t)dt\int_\tau^M E\left(\sqrt{\tau^2 - a^2} + \sqrt{t^2 - a^2}\right)d\tau + \int_\tau^M \bar{E}_3(\tau)d\tau. \tag{3}$$

There are eight integrals which will be denoted by $I_1, I_2, \ldots, I_8$ respectively.

We now examine each integral as $M \to \infty$.* It is clear that I_1 remains unchanged, $I_2 \to 0$, $I_4 \to -\int_\tau^\infty q(t)E_2(t - \tau)\,dt$, $I_6 \to 0$, $I_7 \to -\int_a^\infty q(t)dt\int_\tau^\infty E\left(\sqrt{\tau^2 - a^2} + \sqrt{t^2 - a^2}\right)d\tau$, $I_8 \to \int_\tau^\infty \bar{E}_3(\tau)d\tau$. It remains to study I_3 and I_5.

We shall now use the fact that $|q(t)|$ is a monotonically decreasing function. We then have, since $|q(t)|$ is bounded, that

$$\lim_{t \to \infty} |\,q(t)\,| = r_0$$

exists. We consider:

$$\lim_{M \to \infty}\left[\int_M^\infty q(t)E_2(t - M)dt - \int_\tau^M q(t)E_2(M - t)dt\right]$$

$$= \lim_{M \to \infty}\left[\int_0^\infty q(x + M)E_2(x)dx - \int_0^{M-\tau} q(M - x)E_2(x)dx\right]$$

$$= -r_0\int_0^\infty E_2(x)dx - \lim_{M \to \infty}\int_0^{M-\tau} q(M - x)E_2(x)dx.$$

We wish to show that:

$$\lim_{M \to \infty}\int_0^{M-\tau} q(M - x)E_2(x)dx = -\frac{r_0}{2}. \tag{4}$$

To this end, we write:

$$\int_0^{M-\tau}|q(M - x)|E_2(x)dx \geq r_0\int_0^{M-\tau} E_2(x)dx = r_0\left\{\frac{1}{2} - E_3(M - \tau)\right\}.$$

* *The passage to the limit under the integral sign may be readily justified in each case.*

On the other hand,*

$$\int_0^{M-\tau} |q(M-x)|\,E_2(x)dx$$

$$= \int_\tau^M |q(t)|\,E_2(M-t)dt = \int_\tau^{M/2} |q(t)|\,E_2(M-t)\,dt + \int_{M/2}^M |q(t)|\,E_2(M-t)\,dt$$

$$\leqslant E_2\left(\frac{M}{2}\right)\left|q(\tau)\right|\left(\frac{M}{2}-\tau\right) + \left|q\left(\frac{M}{2}\right)\right|\int_{M/2}^M E_2(M-t)\,dt$$

$$\leqslant E_2\left(\frac{M}{2}\right)a\left(\frac{M}{2}-\tau\right) + \left|q\left(\frac{M}{2}\right)\right|\left\{\frac{1}{2} - E_3\left(\frac{M}{2}\right)\right\}.$$

Thus, we have

$$r_0\left\{\frac{1}{2} - E_2(M-\tau)\right\} \leqslant \int_0^{M-\tau} |q(M-x)|\,E_2(x)dx \leqslant E_2\left(\frac{M}{2}\right)a\left(\frac{M}{2}-\tau\right) + \left|q\left(\frac{M}{2}\right)\right|\left\{\frac{1}{2} - E_3\left(\frac{M}{2}\right)\right\}.$$

Allowing $M \to \infty$ in the above inequality, we obtain

$$\frac{r_0}{2} \leqslant \lim_{M\to\infty} \int_0^{M-\tau} |q(M-x)|E_2(x)dx \leqslant \frac{r_0}{2}.$$

This proves (4) so that finally

$$\lim_{M\to\infty} (I_3 + I_5) = 0.$$

Letting $M \to \infty$ in (3), we obtain:

$$0 = \int_a^\tau q(t)E_2(\tau - t)dt - \int_\tau^\infty q(t)E_2(t-\tau)dt - \int_a^\infty q(t)dt \int_\tau^\infty E\left(\sqrt{r^2-a^2} + \sqrt{t^2-a^2}\right)dr + \int_\tau^\infty \bar{E}_3(\tau)d\tau. \quad (5)$$

Let $\tau = a$ in (5); then:

$$0 = \int_a^\infty q(t)E_2(t-a)dt + \int_a^\infty q(t)dt \int_a^\infty E\left(\sqrt{r^2-a^2} + \sqrt{t^2-a^2}\right)dr - \int_a^\infty \bar{E}_3(r)dr. \quad (6)$$

If we multiply (6) through by -1, we find

$$\int_a^\infty |q(t)|\,dt \int_a^\infty E\left(\sqrt{r^2-a^2} + \sqrt{t^2-a^2}\right)dr + \int_a^\infty |q(t)|\,E_2(t-a)dt = \int_a^\infty |\bar{E}_3(r)|dr.$$

Since $|q(t)|$ is monotonically decreasing, we may write:

$$r_0\left\{\int_a^\infty E_2(t-a)dt + \int_a^\infty dt \int_a^\infty E\left(\sqrt{r^2-a^2} + \sqrt{t^2-a^2}\right)dr\right\} \leqslant \int_a^\infty |\bar{E}_3(r)|\,dr,$$

* *We implicitly assume* $\tau < \frac{M}{2}$ *; this is justified since we allow* $M \to \infty$ *in the end.*

or finally:

$$r_0 \leqslant \frac{\int_a^\infty |\bar{E}_3(r)|\, dr}{\frac{1}{2} + \int_a^\infty dt \int_a^\infty E(\sqrt{r^2 - a^2} + \sqrt{t^2 - a^2})\, dr}. \tag{7}$$

The inequality (7) gives a bound from above for the quantity r_0. To obtain a bound from below, we return to Equation (5), replace there τ by u, and integrate with respect to u from τ to M:

$$0 = \int_\tau^M du \int_a^u q(t)E_2(u-t)dt - \int_\tau^M du \int_u^\infty q(r)E_2(t-u)\, dt$$
$$- \int_\tau^M du \int_a^\infty q(t)dt \int_u^\infty E(\sqrt{r^2 - a^2} + \sqrt{t^2 - a^2})\, dr + \int_\tau^M du \int_u^\infty \bar{E}_3(r)\, dr.$$

Reversing the order of integration, as before,

$$0 = \int_a^\tau q(t)dt \int_\tau^M E_2(u-t)du + \int_\tau^M q(t)dt \int_t^M E_2(u-t)du - \int_\tau^M q(t)dt \int_\tau^t E_2(t-u)du$$
$$- \int_M^\infty q(t)dt \int_\tau^M E_2(t-u)du - \int_\tau^M du \int_a^\infty q(t)dt \int_u^\infty E(\sqrt{r^2 - a^2} + \sqrt{t^2 - a^2})\, dr$$
$$+ \int_\tau^M du \int_u^\infty \bar{E}_3(r)dr.$$

Again using identities on E_n-functions:

$$0 = \int_a^\tau q(t) \left\{ E_3(\tau - t) - E_3(M - t) \right\} dt + \int_\tau^M q(t) \left\{ \frac{1}{2} - E_3(M - t) \right\} dt$$
$$- \int_\tau^M q(t) \left\{ \frac{1}{2} - E_3(t - \tau) \right\} dt - \int_M^\infty q(t) \left\{ E_3(t - M) - E_3(t - \tau) \right\} dt \tag{8}$$
$$- \int_\tau^M du \int_a^\infty q(t)dt \int_u^\infty E(\sqrt{r^2 - a^2} + \sqrt{t^2 - a^2})\, dr + \int_\tau^M du \int_u^\infty \bar{E}_3(r)dr.$$

Allowing $M \to \infty$ as before, the only integrals that require special study are:

$$\lim_{M \to \infty} \left[- \int_\tau^M q(t)E_3(M - t)dt - \int_M^\infty q(t)E_3(t - M)\, dt \right]$$
$$= \lim_{M \to \infty} \left[- \int_0^{M-\tau} q(M - u)E_3(u)du - \int_0^\infty q(M + u)E_3(u)du \right].$$

By an argument similar to that used in deriving (4) we obtain the limit $+ \frac{2}{3} r_0$.

Hence, on passing to the limit $M \to \infty$ in (8), we get:

$$0 = \int_a^\tau q(t)E_3(\tau - t)dt + \int_\tau^\infty q(t)E_3(t - \tau)dt + \frac{2r_0}{3}$$
$$- \int_\tau^\infty du \int_a^\infty q(t)dt \int_u^\infty E(\sqrt{r^2 - a^2} + \sqrt{t^2 - a^2})dr + \int_\tau^\infty du \int_u^\infty \bar{E}_3(r)dr, \tag{9}$$

or setting $\tau = a$,

$$0 = \int_a^\infty q(t)E_3(t-a)dt + \frac{2}{3}r_0 - \int_a^\infty du \int_a^\infty q(t)dt \int_u^\infty E(\sqrt{r^2-a^2}+\sqrt{t^2-a^2})dt + \int_a^\infty du \int_u^\infty \bar{E}_3(r)dr.$$

Multiplying by -1, we obtain:

$$\frac{2}{3}r_0 = \int_a^\infty |q(t)|E_3(t-a)dt - \int_a^\infty |q(t)|dt \int_a^\infty du \int_u^\infty E(\sqrt{r^2-a^2}+\sqrt{t^2-a^2})dr + \int_a^\infty du \int_u^\infty |\bar{E}_3(r)|dr. \tag{10}$$

Now,

$$\int_u^\infty E(\sqrt{r^2-a^2}+\sqrt{t^2-a^2})dr < \int_u^\infty E(r-a+\sqrt{t^2-a^2})dr = E_2(u-a+\sqrt{t^2-a^2})$$

and

$$\int_a^\infty du \int_u^\infty E(\sqrt{r^2-a^2}+\sqrt{t^2-a^2})dr < E_3(\sqrt{t^2-a^2}) < E_3(t-a).$$

Hence, we find from (10):

$$\frac{2}{3}r_0 \geqslant r_0\left\{\frac{1}{3} - \int_a^\infty dt \int_a^\infty du \int_u^\infty E(\sqrt{r^2-a^2}+\sqrt{t^2-a^2})\,dr\right\} + \int_a^\infty du \int_u^\infty |E_3(r)|dr,$$

and finally:

$$r_0 \geqslant \frac{\int_a^\infty du \int_u^\infty |\bar{E}_3(r)|dr}{\frac{1}{3} + \int_a^\infty dt \int_a^\infty du \int_u^\infty E(\sqrt{r^2-a^2}+\sqrt{t^2-a^2})\,dr}. \tag{11}$$

From (6) and (10) one may obtain upper bounds for r_0 which are better than (7). We have, indeed:

$$\int_a^\infty |q(t)|\,E_2(t-a)dt = \int_a^\infty |\bar{E}_3(r)|\,dr - \int_a^\infty |q(t)|dt \int_a^\infty E(\sqrt{r^2-a^2}+\sqrt{t^2-a^2})\,dr,$$

and

$$\int_a^\infty |q(t)|E_3(t-a)dt = \frac{2r_0}{3} + \int_a^\infty |q(t)|dt \int_a^\infty du \int_u^\infty E(\sqrt{r^2-a^2}+\sqrt{t^2-a^2})\,dr - \int_a^\infty du \int_u^\infty |\bar{E}_3(r)|dr.$$

This, in turn, yields:

$$\int_a^\infty |q(t)|E_2(t-a)dt \leqslant \int_a^\infty |\bar{E}_3(r)|dr - r_0 \int_a^\infty dt \int_a^\infty E(\sqrt{r^2-a^2}+\sqrt{t^2-a^2})dr, \tag{12}$$

and

$$\int_a^\infty |q(t)| E_3(t-a)\,dt \geqslant \left\{\frac{2}{3} + \int_a^\infty dt \int_a^\infty du \int_u^\infty E\left(\sqrt{r^2-a^2} + \sqrt{t^2-a^2}\right) dr\right\} r_0 - \int_a^\infty du \int_u^\infty |\bar{E}_3(r)|\,dr. \quad (13)$$

Since $E_2(t-a) > E_3(t-a)$, on subtracting the first equation above from the second, we find:

$$\int_a^\infty |q(t)| \{E_3(t-a) - E_2(t-a)\}\,dt \geqslant r_0 \left\{\frac{2}{3} + \int_a^\infty dt \int_a^\infty E\left(\sqrt{r^2-a^2} + \sqrt{t^2-a^2}\right) dr + \int_a^\infty dt \int_a^\infty du \int_u^\infty E\left(\sqrt{r^2-a^2} + \sqrt{t^2-a^2}\right) dr\right\} - \int_a^\infty |\bar{E}_3(r)|\,dr - \int_a^\infty du \int_u^\infty |\bar{E}_3(r)|\,dr,$$

and finally:

$$r_0 \leqslant \frac{\int_a^\infty |\bar{E}_3(r)|\,dr + \int_a^\infty du \int_u^\infty |\bar{E}_3(r)|\,dr}{\frac{5}{6} + \int_a^\infty dt \int_a^\infty E\left(\sqrt{r^2-a^2} + \sqrt{t^2-a^2}\right) dr + \int_a^\infty dt \int_a^\infty du \int_u^\infty E\left(\sqrt{r^2-a^2} + \sqrt{t^2-a^2}\right) dr}. \quad (14)$$

The second method is based on the fact that:

$$E_4(t-a) - \frac{2}{3} E_3(t-a) > 0,$$

and that $|q(t)|$ is monotonically decreasing. We find that:

$$\int_a^\infty \left\{E_4(t-a) - \frac{2}{3} E_3(t-a)\right\} d|q(t)| < 0.$$

Integrating by parts and observing that the integrated part vanishes at both limits, we obtain:

$$\int_a^\infty |q(t)| \left\{\frac{2}{3} E_2(t-a) - E_3(t-a)\right\} dt > 0.$$

Using (12) and (13) again, we obtain:

$$0 < \frac{2}{3} \int_a^\infty |\bar{E}_3(r)|\,dr - \frac{2}{3} r_0 \int_a^\infty dt \int_a^\infty E\left(\sqrt{r^2-a^2} + \sqrt{t^2-a^2}\right) dr - r_0 \left\{\frac{2}{3} + \int_a^\infty dt \int_a^\infty du \int_u^\infty E\left(\sqrt{r^2-a^2} + \sqrt{t^2-a^2}\right) dr\right\} + \int_a^\infty du \int_u^\infty |\bar{E}_3(r)|\,dr,$$

and finally:

$$r_0 < \frac{\frac{2}{3} \int_a^\infty |\bar{E}_3(r)|\,dr + \int_a^\infty du \int_u^\infty |\bar{E}_3(r)|\,dr}{\frac{2}{3} \int_a^\infty dt \int_a^\infty E\left(\sqrt{r^2-a^2} + \sqrt{t^2-a^2}\right) dr + \frac{2}{3} + \int_a^\infty dt \int_a^\infty du \int_u^\infty E\left(\sqrt{r^2-a^2} + \sqrt{t^2-a^2}\right) dr} \quad (15)$$

It is to be expected—and has also been checked—in analogy with the plane case that (15) is a more refined upper limit than (14), which itself is a more refined limit than (7). We have tried to obtain a more refined lower limit for r_0 than is given by (11) but without success. It seems impossible to do so in principle since the part of the integral kernel which depends on the square root always makes the inequalities go in the wrong direction. Since more delicate properties of the difference of two E_n-functions are employed in the derivation of the refined upper limit (15) than in the derivation of the crude lower limit given by (11), it is clear that the value of r_0 given by (15) must be closer to the actual value than the one given by (11). This is made very plausible by considering the limit $a \to \infty$; the integrals involving the E_n-functions of square roots then approach zero and the bounds for $(r_0 - a)$ — it is more revealing to talk about $(r_0 - a)$ than r_0— are given simply by:

$$-\frac{3}{4} < (r_0 - a) < -\frac{17}{24}. \tag{16}$$

The correct value of $(r_0 - a)$ is -0.7104; it is seen that the upper limit is out only by 0.3%, while the lower limit is in error by 5.5%. Since all the integrals involved are monotonic functions of a, it is reasonable to suppose that a similar situation prevails over the entire range, except for sufficiently small* a.

The integrations in (15) involving the square roots can only be performed by numerical means. It is convenient to rewrite (15) in the form:

$$(r_0 - a)_u < \frac{-\frac{17}{36} - a\left(\frac{2}{3}B + C\right) + \left(\frac{2A}{3} + D\right)}{\frac{2}{3} + \left(\frac{2}{3}B + C\right)}, \tag{17}$$

where

$$A = \int_a^\infty E_3(\sqrt{t^2 - a^2})dt,$$

$$B = \int_a^\infty dt \int_a^\infty E(\sqrt{r^2 - a^2} + \sqrt{t^2 - a^2})dr,$$

$$C = \int_a^\infty dt \int_a^\infty du \int_u^\infty E(\sqrt{t^2 - a^2} + \sqrt{r^2 - a^2})dr,$$

$$D = \int_a^\infty du \int_u^\infty E_3(\sqrt{t^2 - a^2})dt.$$

In terms of the above notation the lower bound for $(r_0 - a)$ is:

$$(r_0 - a)_l > \frac{-\frac{1}{4} - aC + D}{\frac{1}{3} + C}. \tag{18}$$

* *For very small a, Equation (15) predicts an $a^2 \log a$ behavior for r_0 as $a \to 0$, whereas the correct behavior is a^2. Curiously enough, Equation (11) gives the correct behavior of r_0 as $a \to 0$.*

The integrals A, B, C, and D have been computed for $a = 0.5, 1, 2, 5$ and are given in columns 2–5 of Table I. Columns 6 and 7 contain $(r_0 - a)_u$ and $(r_0 - a)_l$ respectively.

TABLE I

a	A	B	C	D	$(r_0-a)_u$	$(r_0-a)_l$
0.5	0.2071	0.1764	0.1180	0.1452	−0.340	−0.363
1.0	0.1516	0.0932	0.0560	0.0941	-0.503_5	-0.544_5
2.0	0.0968	0.0377	0.0174	0.0457	−0.630	−0.681
5.0	0.0442	0.00782	0.00187	0.0120	−0.692	−0.740
∞	0	0	0	0	−0.708	−0.750

Appendix

We first prove a lemma:

Lemma. For all $\tau > a$:

$$\bar{E}_3(\tau) = -\left[aE_2(\tau - a) - E_3(\tau - a) + E_3\left(\sqrt{\tau^2 - a^2}\right)\right] < 0.$$

By the mean value theorem:

$$E_3(\tau - a) - E_3\left(\sqrt{\tau^2 - a^2}\right) = E'_3(\xi)\left[\tau - a - \sqrt{\tau^2 - a^2}\right] = E_2(\xi)\left[\sqrt{\tau^2 - a^2} - (\tau - a)\right],$$

where $$\tau - a < \xi < \sqrt{\tau^2 - a^2}.$$

Now,

$$aE_2(\tau - a) - E_3(\tau - a) + E_3\left(\sqrt{\tau^2 - a^2}\right) = aE_2(\tau - a) - E_2(\xi)\left[\sqrt{\tau^2 - a^2} - (\tau - a)\right]$$
$$> aE_2(\xi) - E_2(\xi)\left[\sqrt{\tau^2 - a^2} - (\tau - a)\right] = E_2(\xi)\left[\tau - \sqrt{\tau^2 - a^2}\right] > 0.$$

This proves the lemma.

We next prove that if $f(\tau)$ is the solution of the integral equation:

$$f(\tau) = \frac{1}{2}\int_a^\infty f(t)\left\{E\left(|\tau - t|\right) - E\left(\sqrt{\tau^2 - a^2} + \sqrt{t^2 - a^2}\right)\right\} dt,$$

so normalized that $f(\tau) = \tau - a + \bar{q}(\tau)$, then $0 < \bar{q}(\tau) \leqslant a$ for all $\tau > a > 0$.

We first observe that since:

$|\tau - t| < \sqrt{\tau^2 - a^2} + \sqrt{t^2 - a^2}$ and $E(t)$ is a monotonically decreasing function, $E(|\tau - t|) - E\left(\sqrt{\tau^2 - a^2} + \sqrt{t^2 - a^2}\right) > 0$. Next, evaluating the integral:

$$\frac{1}{2}\int_a^\infty \left\{E(|\tau - t|) - E\left(\sqrt{\tau^2 - a^2} + \sqrt{t^2 - a^2}\right)\right\} dt = 1 - \frac{1}{2}E_2(\tau - a)$$
$$- \frac{1}{2}\int_a^\infty E\left(\sqrt{\tau^2 - a^2} + \sqrt{t^2 - a^2}\right) dt,$$

we obtain:

$$1 = \frac{1}{2}\int_a^\infty \{E(|\tau - t|) - E(\sqrt{\tau^2 - a^2} + \sqrt{t^2 - a^2})\}\, dt + \frac{1}{2} E_2(\tau - a) + \frac{1}{2}\int_a^\infty E(\sqrt{\tau^2 - a^2} + \sqrt{t^2 - a^2})dt.$$

Secondly, evaluating the integral:

$$\frac{1}{2}\int_a^\infty (t-a)\{E(|\tau - t|) - E(\sqrt{\tau^2 - a^2} + \sqrt{t^2 - a^2})\}\, dt,$$

we obtain:

$$\tau - a = \frac{1}{2}\int_a^\infty (t-a)\{E(|\tau - t|) - E(\sqrt{\tau^2 - a^2} + \sqrt{t^2 - a^2})\}\, dt + \frac{1}{2}\int_a^\infty (t-a) E(\sqrt{\tau^2 - a^2} + \sqrt{t^2 - a^2})dt - \frac{1}{2} E_3(\tau - a).$$

Furthermore,

$$\frac{1}{2}\int_a^\infty tE(\sqrt{\tau^2 - a^2} + \sqrt{t^2 - a^2})\, dt = \frac{1}{2} E_3(\sqrt{\tau^2 - a^2}),$$

so that the above equation becomes:

$$(2)\quad \tau - a = \frac{1}{2}\int_a^\infty (t-a)\{E(|\tau - t|) - E(\sqrt{\tau^2 - a^2} + \sqrt{t^2 - a^2})\}\, dt - \frac{1}{2} E_3(\tau - a) + \frac{1}{2} E_3(\sqrt{\tau^2 - a^2}) - \frac{a}{2}\int_a^\infty E(\sqrt{\tau^2 - a^2} + \sqrt{t^2 - a^2})dt.$$

Multiplying Equation (1) by a and adding to (2), we get:

$$(3)\quad \tau = \frac{1}{2}\int_a^\infty t\{E(|\tau - t|) - E(\sqrt{\tau^2 - a^2} + \sqrt{t^2 - a^2})\}\, dt + \frac{1}{2}\{aE_2(\tau - a) - E_3(\tau - a) + E_3(\sqrt{\tau^2 - a^2})\}.$$

Since in (2):

$$E_3(\tau - a) - E_3(\sqrt{\tau^2 - a^2}) + a\int_a^\infty E(\sqrt{\tau^2 - a^2} + \sqrt{t^2 - a^2})\, dt > 0,$$

we obtain:

$$(4)\quad \tau - a < \frac{1}{2}\int_a^\infty (t-a)\{E(|\tau - t|) - E(\sqrt{\tau^2 - a^2} + \sqrt{t^2 - a^2})\}\, dt$$

and, in view of the lemma, from (3) we find

$$(5)\quad \tau > \frac{1}{2}\int_a^\infty t\{E(|\tau - t|) - E(\sqrt{\tau^2 - a^2} + \sqrt{t^2 - a^2})\}\, dt.$$

We now introduce the sequence of functions:

$$(6)\quad f_1(\tau) = \tau - a,\ f_n(\tau) = \frac{1}{2}\int_a^\infty f_{n-1}(t)\{E(|\tau - t|) - E(\sqrt{\tau^2 - a^2} + \sqrt{t^2 - a^2})\}\, dt.$$

Inequality (4) shows that:

$$f_1(\tau) < f_2(\tau).$$

Multiplying both sides by $\frac{1}{2}\{E(|\tau - t|) - E(\sqrt{\tau^2 - a^2} + \sqrt{t^2 - a^2})\}$ and integrating, since the multiplying factor is positive, we find:

$$f_2(\tau) < f_3(\tau)$$

and generally:

$$f_{n-1}(\tau) < f_n(\tau). \tag{7}$$

Returning now to inequality (5), from $\tau - a < \tau$ and the positivity of the kernel, we find:

$$f_2(\tau) < \frac{1}{2}\int_a^\infty t\{E(|\tau - t|) - E(\sqrt{\tau^2 - a^2} + \sqrt{t^2 - a^2})\}\,dt < \tau.$$

Repeating the argument,

$$f_3(\tau) = \frac{1}{2}\int_a^\infty f_2(t)\{E(|\tau - t|) - E(\sqrt{\tau^2 - a^2} + \sqrt{t^2 - a^2})\}\,dt$$

$$< \frac{1}{2}\int_a^\infty t\{E(|\tau - t|) - E(\sqrt{\tau^2 - a^2} + \sqrt{t^2 - a^2})\}\,dt < \tau.$$

Thus,

$$f_n(\tau) < \tau. \tag{8}$$

In any finite interval, therefore, the sequence $\{f_n(\tau)\}$ is bounded and according to (7), the sequence is monotonically increasing. Consequently, the limit:

$$\lim_{n \to \infty} f_n(\tau) = f(\tau)$$

exists. By well known theorems we are justified in taking the limit $n \to \infty$ under the integral sign in (6), which shows that $f(\tau)$ is a solution of the integral equation:

$$f(\tau) = \frac{1}{2}\int_a^\infty f(t)\{E(|\tau - t|) - E(\sqrt{\tau^2 - a^2} + \sqrt{t^2 - a^2})\}\,dt.$$

It follows, moreover, from (7) and (8) that the solution $f(\tau)$ satisfies the inequalities:

$$\tau - a < f(\tau) \leqslant \tau.$$

Applied to $\bar{q}(\tau)$, this means that $0 < \bar{q}(\tau) \leqslant a$, as was to be proved.

References

1. BERLIN, T. H. Phys. Rev. 73: 437. 1948.
2. HANSSON, L. and WALLER, I. Ark. Mat. Astron. Fysik, B, 36: (8). 1949.
3. HOPF, E. Mathematical problems of radiative equilibrium. Cambridge University Press, London. 1934. Chap. II.
4. MARSHAK, R. E. Phys. Rev. 71: 443. 1947.

A METHOD OF MEASURING GAMMA-RAY ABSORPTION COEFFICIENTS AT 0.51 Mev[1]

By P. E. Argyle, G. M. Griffiths, and J. B. Warren

Abstract

The coincidence method described makes use of the angular correlation between pairs of annihilation quanta to eliminate the effect of scattered radiation usually present in absorption measurements. Mass absorption coefficients in $(gm./cm.^2)^{-1}$ found by this method are as follows:

Lead	0.1519 ± 0.0008
Copper	0.0819 ± 0.0005
Aluminum	0.0831 ± 0.0013.

Introduction

In the usual methods (1) employed for accurate measurements of gamma-ray absorption coefficients, the main difficulty is to prevent scattered radiation from reaching the detector. We have circumvented this difficulty by using the precise 180° angular correlation (2) between two annihilation quanta to measure the absorption of 0.51 Mev. radiation.

Two gamma-ray scintillation counters were placed in line several meters apart, one on each side of a thick source of positrons. The coincidence rate between the counters was measured as a function of the thickness of the absorber which was placed between the source and one counter, as close to the source as possible.

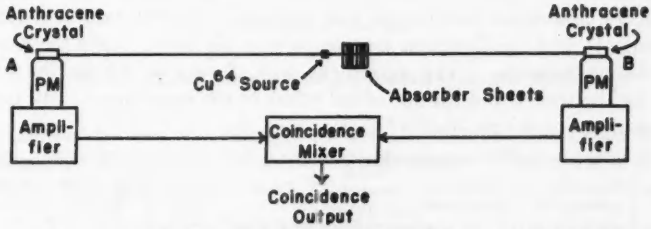

FIG. 1. *Apparatus for measuring absorption coefficients at 0.51 Mev.*

Counter *A* (Fig. 1) acts as a collimator for the gamma-ray 'beam' from the source to counter *B*, but does not itself scatter a significant amount of radiation back into *B*. Radiation scattered by the absorber and by the laboratory walls, while it may enter one of the detectors, cannot produce a coincidence count in both detectors owing to the exact antiparallelism of the pair of annihilation quanta. This is a simple method of producing a beam of monochromatic gamma-rays collimated to any desired degree of accuracy—

[1] *Manuscript received August 28, 1950.*
Contribution from the Department of Physics, University of British Columbia, Vancouver, B.C.

which could be used, for example, to measure the variation in efficiency of a Geiger counter over its volume.

Experimental

The scintillation counters consisted of blocks of anthracene placed on RCA 5819 photomultipliers, and the source of annihilation radiation was Cu^{64} produced in the Chalk River pile. The distance between each detector and the source was 220 cm. and the plane angle subtended by the phosphors at the source was just 3/4°. The pulses, after amplification, were standardized by fast multivibrators with dead times of 17 μsec. and then fed into a Rossi circuit of resolving time 0.15 μsec. Considerable care was taken to keep the over-all gain of the system, and hence the efficiency of the counters, constant during the runs. The stability was checked by taking readings on the coincidence rate with no absorber and comparing the half life deduced from these readings with the accepted value. With the multiplier operating conditions chosen the noise rates were about 10 per second, which gave an insignificant number of coincidence background counts.

Results

The experimental readings were corrected for accidentals, dead time losses, and source decay. The value of half life used for the decay correction was 12.88 ± 0.03 hr. (5). The table below shows the experimental absorption coefficients obtained from our results by the method of least squares, the values predicted by theory, and values obtained by other experimenters. The photoelectric absorption coefficients were obtained from the curves of Hulme and others (4), and the Compton absorption was calculated on the basis of the Klein-Nishina formula. The agreement with theory is within the errors quoted for the theory and the statistical errors of the experiment. All results are given in units of $(gm./cm.^2)^{-1}$.

Absorber	Photoelectric absorption	Compton absorption	Total theoretical absorption	Present authors	Glendenin (Ref. 3)	Cowan (Ref. 1)
Pb	0.0802	0.0675	0.1477	0.1519 ± 0.0008	0.154	–
Cu	0.0028	0.0778	0.0806	0.0819 ± 0.0005	–	0.079
Al	0.0002	0.0823	0.0825	0.0831 ± 0.0013	0.082	0.083

The maximum thicknesses of absorber used were 4 cm. for lead, 4.7 cm. for copper, and 5 cm. for aluminum. Fig. 2 shows the counting rates in the two counters and in the coincidence channel, after corrections, for the case when lead absorbers were used.

These curves indicate clearly how the effect of scattering from walls, tables, and supports distorts the counting rate curve for counter *B* when the absorber is put between that counter and the source, while the coincidence curve

remains straight. The stability of the apparatus is indicated by the fact that the counting rate in counter *A* remained constant to within 3%. The actual stability is probably better than this, since a considerable fraction of the 3% rise in counting rate of '*A*' as the absorber thickness is increased can be attributed to backscattering from the absorber.

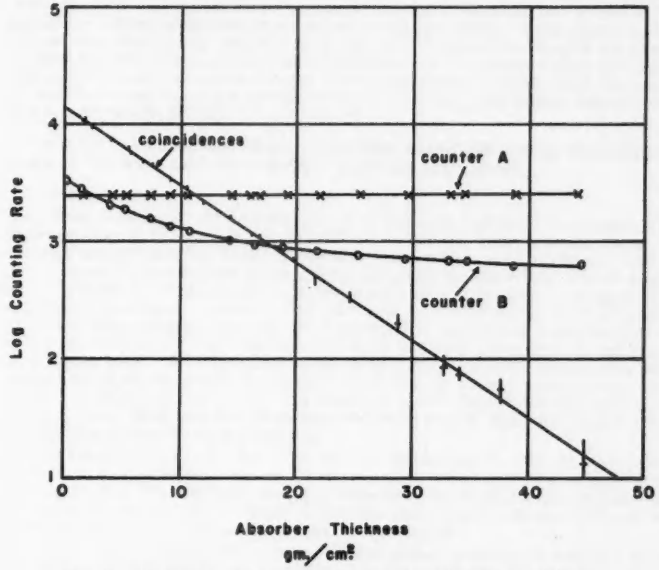

FIG. 2. *Channel counting rates as a function of absorber thickness.*

The aluminum used was Alcan 2S, which the manufacturers state is about 99.5% pure. The copper was made electrolytically. The purity of the lead was better than 99.9%

Acknowledgments

We wish to thank the Consolidated Mining and Smelting Company of Trail, B.C., for providing lead and the analysis thereof.

References

1. COWAN, C. L. Phys. Rev. 74: 1841. 1948.
2. DEBENEDETTI, S., COWAN, C. E., KONNEKER, W. R., and PRIMAKOFF, H. Phys. Rev. 77: 205. 1950.
3. GLENDENIN, L. E. Nucleonics, 2 (No. 1): 12. 1948.
4. HULME, H. R., MCDOUGALL, J., BUCKINGHAM, R. A., and FOWLER, R. H. Proc. Roy. Soc. (London), A, 149: 131. 1935.
5. SILVER, LORNA M. Can. J. Phys. 29:59. 1951.

CANADIAN JOURNAL OF PHYSICS

Notice to Contributors

GENERAL: Manuscripts should be typewritten, double spaced, and the **original and one extra copy** submitted. Style, arrangement, spelling, and abbreviations should conform to the usage of this Journal. Names of all simple compounds, rather than their formulas, should be used in the text. Greek letters or unusual signs should be written plainly or explained by marginal notes. Superscripts and subscripts must be legible and carefully placed. Manuscripts should be carefully checked before being submitted, to reduce the need for changes after the type has been set. If authors require changes to be made after the type is set, they will be charged for changes that are considered to be excessive. **All pages, whether text, figures, or tables, should be numbered.**

ABSTRACT: **An abstract of not more than about 200 words, indicating the scope of the work and the principal findings, is required.**

ILLUSTRATIONS:

(i) *Line Drawings:* All lines should be of sufficient thickness to reproduce well. Drawings should be carefully made with India ink on white drawing paper, blue tracing linen, or co-ordinate paper **ruled in blue only**; any co-ordinate lines that are to appear in the reproduction should be ruled in black ink. Paper ruled in **green, yellow, or red should not be used** unless it is desired to have all the co-ordinate lines show. Lettering and numerals should be neatly done in India ink preferably with a stencil (**do not use typewriting**) and be of such size that they will be legible and not less than one millimeter in height when reproduced in a cut three inches wide. All experimental points should be carefully drawn with instruments. Illustrations need not be more than two or three times the size of the desired reproduction, but the ratio of height to width should conform with that of the type page. **The original drawings and one set of small but clear photographic copies are to be submitted.**

(ii) *Photographs:* Prints should be made on glossy paper, with strong contrasts; they should be trimmed to remove all extraneous material so that essential features only are shown. Photographs should be submitted **in duplicate**; if they are to be reproduced in groups, one set should be so arranged and mounted on cardboard with rubber cement; the duplicate set should be unmounted.

(iii) *General:* **The author's name, title of paper, and figure number should be written in the lower left hand corner (outside the illustration proper) of the sheets on which the illustrations appear.** Captions should not be written on the illustrations, but typed on a separate page of the manuscript. All figures (including each figure of the plates) should be numbered consecutively from 1 up (arabic numerals). **Each figure should be referred to in the text.** If authors desire to alter a cut, they will be charged for the new cut.

TABLES: Each table should be typed on a separate sheet. Titles should be given for all tables, which should be numbered in Roman numerals. Column heads should be brief and textual matter in tables confined to a minimum. **Each table should be referred to in the text.**

REFERENCES: **These should be listed alphabetically by authors' names, numbered in that order, and placed at the end of the paper.** The form of literature citation should be that used in this Journal. **Titles of papers should not be given.** The first page only of the references cited should be given. **All citations should be checked with the original articles.** Each citation should be referred to in the text by means of the key number.

REPRINTS: Fifty reprints of each paper without covers are supplied free. Additional reprints, if required, will be supplied according to a prescribed schedule of charges. On request, covers can be furnished at cost.

Manuscripts should be addressed: *Canadian Journal of Physics,*
National Research Council,
Ottawa, Canada.

Contents

Page

γ-rays Produced by Slow Neutron Capture in Beryllium, Carbon, and Nitrogen—*B. B. Kinsey, G. A. Bartholomew, and W. H. Walker* - 1

The Angular Distribution of the Radiation at the Interface of Two Adjoining Media—*S. Chandrasekhar* - - - - - - - 14

The Effects of Plastic Deformation on Magnetic Properties of Polycrystalline Metals—*Ursula M. Martius* - - - - - - - 21

The Angular Correlation of Annihilation Radiation—*P. E. Argyle and J. B. Warren*- - - - - - - - - - - - - - - - - 32

The Scattering Lengths of the Deuteron—*D. G. Hurst and N. Z. Alcock* - 36

The Precision Measurement of Half Lives of Radioactive Substances—*Lorna M. Silver* - - - - - - - - - - - - - - - 59

Note on the Relation between Feynman's Formulation of Scattering Problems and the Born Approximation—*J. R. H. Dempster* 66

Upper and Lower Bounds for the Asymptotic Neutron Density in Milne's Problem for the Sphere—*W. Seidel and R. E. Marshak* 72

A Method of Measuring Gamma Ray Absorption Coefficients at 0.51 Mev.—*P. E. Argyle, G. M. Griffiths, and J. B. Warren* - 83